INFORMATION TO USERS

This manuscript has been reproduced from the microfilm master. UMI films the text directly from the original or copy submitted. Thus, some thesis and dissertation copies are in typewriter face, while others may be from any type of computer printer.

The quality of this reproduction is dependent upon the quality of the copy submitted. Broken or indistinct print, colored or poor quality illustrations and photographs, print bleedthrough, substandard margins, and improper alignment can adversely affect reproduction.

In the unlikely event that the author did not send UMI a complete manuscript and there are missing pages, these will be noted. Also, if unauthorized copyright material had to be removed, a note will indicate the deletion.

Oversize materials (e.g., maps, drawings, charts) are reproduced by sectioning the original, beginning at the upper left-hand corner and continuing from left to right in equal sections with small overlaps.

ProQuest Information and Learning
300 North Zeeb Road, Ann Arbor, MI 48106-1346 USA
800-521-0600

Dielectric-Enhanced Quantum-Well Intermixing in $\lambda = 1.55\,\mu$m InGaAsP/InP Laser Structures

by

JOHN HAZELL, M. ENG, B. ENG.

A Thesis
Submitted to the School of Graduate Studies
in Partial Fulfillment of
the Requirements for the Degree
Doctor of Philosophy

McMaster University

Dielectric-Enhanced Quantum-Well Intermixing in $\lambda = 1.55\,\mu$m InGaAsP/InP Laser Structures

DOCTOR OF PHILOSOPHY (2000)
(Engineering Physics)

McMaster University
Hamilton, Ontario

TITLE: Dielectric-Enhanced Quantum-Well Intermixing in $\lambda = 1.55\,\mu$m InGaAsP/InP Laser Structures

AUTHOR: John Hazell,
M. Eng. (McMaster University, Hamilton)
B. Eng. (Queen's University, Kingston)

SUPERVISORS: Professor John G. Simmons
Professor David A. Thompson

NUMBER OF PAGES: xiii, 114

Abstract

This thesis presents dielectric-enhanced quantum-well intermixing (QWI) studies of InGaAsP/InP-based $\lambda = 1.55\,\mu$m laser structures for photonic integration. QWI is studied as a function of MBE growth, dielectric film (SiO_xN_y) composition and thickness, annealing temperature and time. The results suggest there are at least two processes that cause intermixing in samples without dielectric coatings, related to grown-in defects. It is found that plasma-enhanced chemical-vapor-deposited SiO_xN_y films of refractive index 1.65 are best at enhancing the QWI process. Based on SIMS measurements of these films before and after anneal we observe the migration of Group III atoms into the dielectric film. Consequently we believe that Group V interstitials are injected into the laser structure and are responsible for the enhanced QWI. However, the amount of intermixing does not correlate with the amount of Group III that migrates into the dielectric film, suggesting that another factor, such as film stress, may affect the amount of injected interstitials. This postulated mechanism for InGaAsP/InP-based structures differs from the accepted belief that in the GaAs materials system the dielectric film injects Group III vacancies into material which promote the intermixing process, and that the number of injected vacancies is related to the film porosity. The thesis concludes with a presentation of materials properties and processing issues which are important for device fabrication. It is shown that although the electrical and optical properties of the intermixed material remain desirable, the process leads to difficulties in wet chemical etching and regrowth over material annealed with dielectric films.

Contents

List of Figures

List of Tables

Glossary of Abbreviations

AFM	Atomic Force Microscopy
BHF	10:1 Buffered HF (acid solution)
BPM	Beam Propagation Method
CB	Conduction Band
DFB	Distributed Feedback
DOS	Density of States
ECR	Electron-Cyclotron-Resonance
ENIAC	Electronic Numerical Integrater and Computer
ES	Etch Stop Layer
FTIR	Fourier Transform Infra-Red Spectroscopy
FWHM	Full Width at Half Maximum
GRINSCH	Graded-Index Separate-Confinement Heterostructure
GSMBE	Gas-Source Molecular Beam Epitaxy
HH	Heavy Hole
LEHM	Half-Width at Half Maximum; Low Energy Side
LH	Light Hole
LCM	Lateral Composition Modulation (Spinodal Decomposition)
LTPL	Low-Temperature Photoluminescence
MBE	Molecular Beam Epitaxy
MOCVD	Metal-Organic Chemical Vapor Deposition
MOVPE	Metal-Organic Vapor-Phase Epitaxy
MQW	Multiple Quantum Well
PL	Photoluminescence
PECVD	Plasma Enhanced Chemical Vapor Deposition
Q	Quaternary, i.e. 1.15 Q indicates material with a RTPL $\lambda = 1.15\,\mu$m
QW	Quantum Well
QWI	Quantum Well Intermixing
RTA	Rapid Thermal Anneal
RTPL	Room-Temperature Photoluminescence
SIMS	Secondary Mass Ion Spectroscopy
SOG	Spin-On Glass
SPL	Scanning Photoluminescence
TEM	Transmission Electron Microscopy
VCSEL	Vertical-Cavity Surface-Emitting Laser
WDM	Wavelength Division Multiplexing

Acknowledgements

I would like to thank all the people that have made contributions to this project.

Most importantly I would like to thank my supervisors, Dr. Simmons and Dr. Thompson, for their support, guidance, and funding. I would also like to thank Nortel, Materials and Manufacturing Ontario, and NSERC for their financial support through my degree. I would like to thank my supervisory committee members Dr. Cassidy and Dr. Preston for their participation and help.

Special thanks to the researchers at the NRC; Irwin Sproule for SIMS measurements, J.J. He for instruction in Fabry-Perot characterization, John Stapledon for film stress measurements, and Dolf Landheer for ECR dielectric films. I would also like to thank Brad Robinson, Scott McMaster, and Nortel for crystal growths, Steve Wallace for ECR CVD growths, Andy Duft and Fred Pearson for AFM measurements and TEM training, Luke Doran, Scott Hamilton and Doug Bruce for scanning PL measurements, and Peter Smith for positron measurements,

Many researchers have made contributions to this project, most importantly Greg Letal with whom the initial work was done and who contributed to the regrowth and regrowth TEM studies. I would also especially like to thank Nicolas Berscht for his help with sample preparation and testing. Brooke Gordon, and Joe Dailliere and Q.C. Zhao for their help with the CVD and sample preparation, and Matt Pearson for the his code and help that made BPM calculations possible. I would also like to thank Susan Nagy, Kevin Cearns, Doug Bruce, and Doris Stevanovic for their training on the equipment in the department.

Finally I would like to thank my mother for always being there to support me.

This thesis was prepared using LaTeX; data was analyzed and presented using Matlab.

Chapter 1

Background

1.1 Introduction to Integration

Integration is the process of combining parts into a whole. The trend towards integration is commonplace in many aspects of our lives today. Take for example stereo mini-systems: in one package you receive a radio, tape player, compact disc player, volume control, and speakers. The overall system is much smaller than assembling the respective pieces bought separately, and there is no effort involved in connecting the components to achieve a working system. A complete system can also be purchased at a lower price than the sum of the individual components.

Whereas the stereo system analogy above is somewhat superficial, it illustrates the main reasons why the integration of electrical "valves" has had such a profound impact on our society. These vacuum tubes generally run under significant voltage, glow, and become rather hot during normal operation. The first electronic computer, ENIAC, was constructed in 1945 from 18,000 vacuum tubes, 70,000 resistors, and 10,000 capacitors [1]. It weighed 30 tons, and required 130 kW of power [2]. The advent of the transistor – a new type of valve – by William Shockley in 1948 changed the face of electrical circuits. The transistor, created from crystalline material alone, performed all the same functions as a vacuum tube valve while being smaller, lighter and more functional. Si-based micro-chips, found in almost all electronic equipment these days, primarily consist of transistors which have been integrated together on the surface of a Si crystal. Where the first computers consisted of thousands of

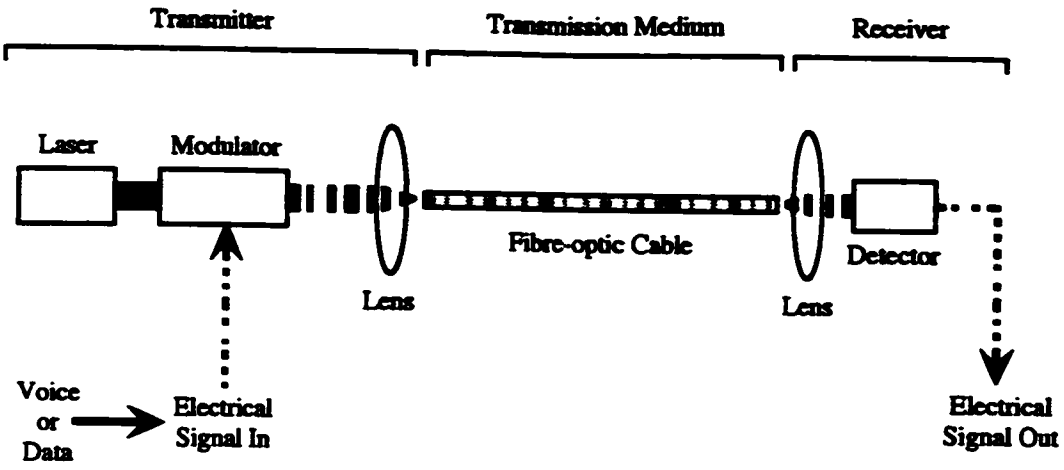

Figure 1.1: An example optical communications system.

valves contained in a room, the Pentium III microprocessor incorporates 9.5 million transistors [3] on the surface of a Si crystal less than a square inch in area! The advantages of speed, efficiency, functionality, and reliability of electronic integration are dramatically illustrated by comparing the computers of today to their predecessors.

Optical communications systems are currently striving to reap the benefits from the integration of photonic devices. In the most straightforward manner, optical communications systems consist of a transmitter and receiver, separated by the transmission medium that carries the light signal from one to the other, as shown in Fig. 1.1. In the transmitter module a light beam is generated, the message is encoded onto the light beam, and the light beam launched into the transmission medium. Figure 1.1 illustrates a simplified example where a laser produces a light beam which acts as a carrier for the signal. In this example a modulator "chops" the laser beam to encode the signal onto the beam. Lenses are used to guide and focus the light beam into a fibre-optic cable – a light pipe which is used as the transmission medium. By integrating these devices together the transmitter module would become smaller and more reliable. In this scheme only one light signal is sent down the optical fibre. A scheme called wavelength-division multiplexing (WDM), shown in Fig. 1.2, increases the capacity of a system by transmitting more than one signal simultaneously, by encoding the various signals on light beams of different wavelengths. Optical integration not

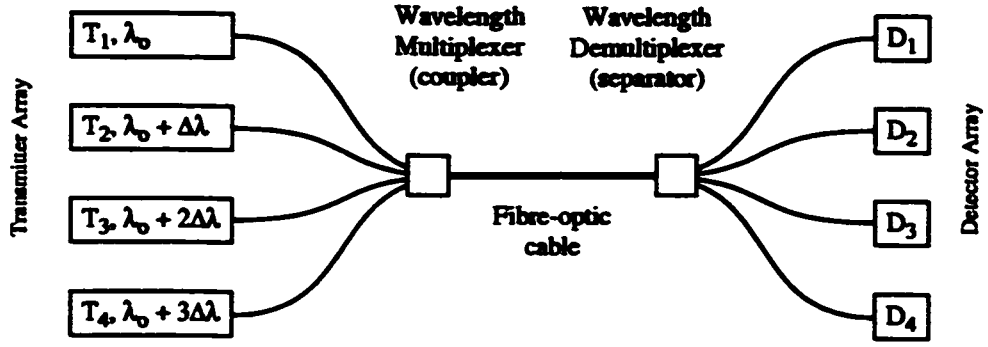

Figure 1.2: An WDM-based optical communications system.

only promises to integrate the transmitter into one package, but to integrate an array of transmitters into a single package, thereby providing a WDM transmitter module.

Current optical communication systems commonly rely on semiconductor lasers operating at 1550 nm to produce the light signal. Since the modulator and guiding functions can also be implemented in the same type of material, it makes excellent sense to integrate these devices together. However, integration of photonic components poses different problems than that of electronic integration. The electrical properties of the semiconductor material are controlled by "doping" it with small amounts of impurities. Si-based electronics depend on precise control of the doping profiles to place many transistors side by side. Photonic devices require an extra degree of control. The production of light is intimately related to the band-gap of the crystal material, which corresponds to a range of energies at which the electron and hole charge carriers are not permitted to exist [4]. The radiative recombination of an electron and a hole across the band-gap produces a photon, which to first approximation corresponds to the band-gap energy. The indirect band-gap of Si makes it an inefficient light emitter. The InP and GaAs materials systems have a direct band-gap, although they do not produce light at 1550 nm. The solution is to create light using an alloy of $In_{(1-x)}Ga_xAs_yP_{(1-y)}$ which emits at the desired wavelength. Therefore, unlike micro-chips constructed using Si, a semiconductor laser structure is built from various layers of $In_{(1-x)}Ga_xAs_yP_{(1-y)}$. A ridge-waveguide semiconductor laser is illustrated in Fig. 1.3. The layers of different composition are grown epitaxially upon a single crystal InP substrate. The ridge feature and metallic contacts are formed subsequent to the crystal growth. The com-

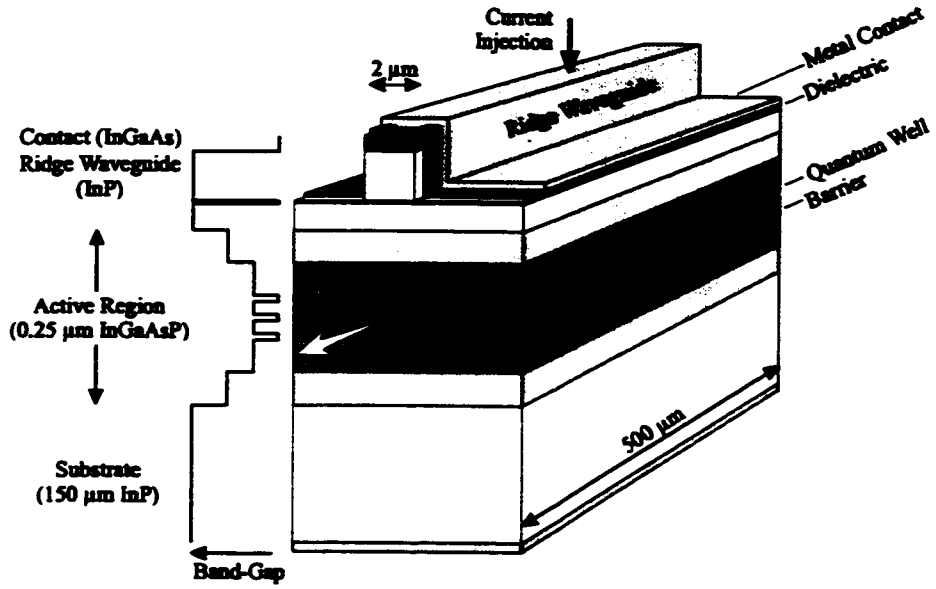

Figure 1.3: A semiconductor ridge laser.

plicated structure controls both the electrical and optical aspects of the device. Electrical current is injected into the device at the top contact. The injected carriers seek to minimize their potential energy through scattering processes, and therefore become localized in the layers of lowest band-gap. This corresponds to the quantum wells (QW), and when the carriers radiatively recombine here they produce the light output of the device. The ridge waveguide laterally confines the injected current and guides the optical field.

By the same token that the device emits light equivalent to the lowest band-gap layer, conversely, the same device will only significantly absorb photons of energy greater than the band-gap. Photonic devices rely on the band-gap to allow for either the generation, transmission, or absorption of light. Therefore, to integrate different photonic devices side-by-side on the same wafer one must find a way to vary locally the band-gap (in this case, of the QW) across the surface of the sample. Once this has been accomplished, devices are patterned over the sample to produce the integrated structures [5]. For example, by patterning a ridge-waveguide that spans areas of both low and high QW band-gap, a laser integrated with a non-absorbing waveguide is produced, as shown in Fig. 1.4. Under current injection the low band-gap QWs produce the light. The higher band-gap QWs will be non-

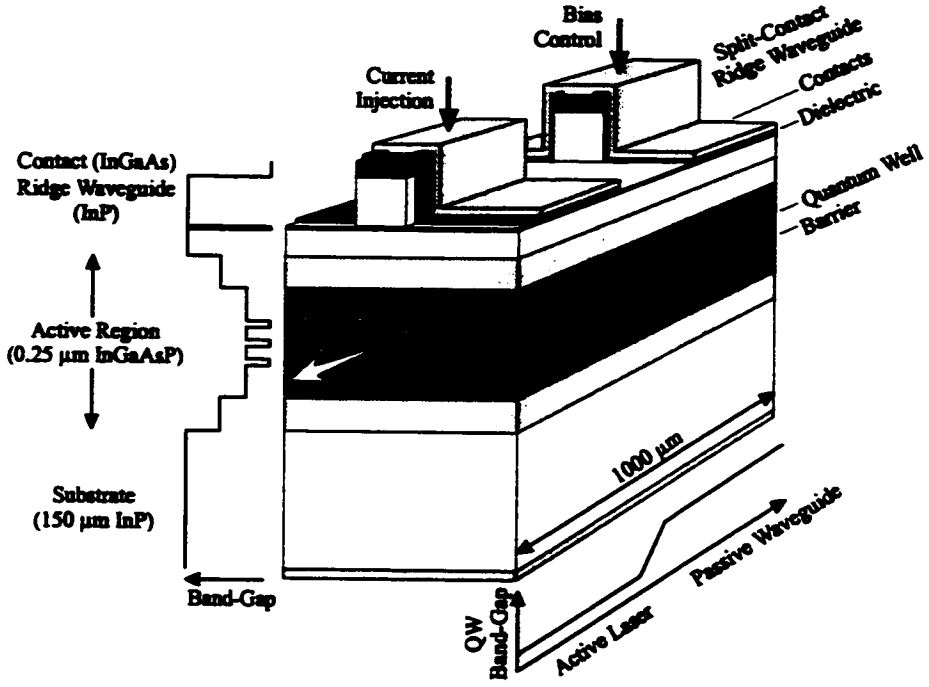

Figure 1.4: A semiconductor ridge laser integrated with a non-absorbing waveguide. Under bias the waveguide section may be used as an integrated modulator.

absorbing and transmit the light. If the band-gap shift in the second section is carefully chosen, roughly 80 nm in the 1550 nm regime [6], a reverse bias applied to the second contact will cause the waveguide section to become absorbing. Thus, the device may also be used as an integrated laser-modulator, based on the quantum-confined Stark effect.

There are three principal ways to create localized areas of differing band-gap, namely, etching and re-growth, selected-area epitaxy, and quantum well (QW) intermixing (QWI).

Etching and regrowth consists of etching the layer structure away from selected areas of a sample, and epitaxially regrowing a new layer structure with different compositions in its place [7]. A specific etch and regrow step is need for each different region desired. The growth of unwanted material over previously deposited sections must be removed by etching. This process has the particular benefit of precisely controlling the compositions, thickness, and doping of each region, but it suffers from having a low success rate since precise control over the etching and regrowth is difficult.

Selected-area epitaxy is more successful, and consists of performing crystal growths on

a sample that has been patterned with oxide stripes [8]. The crystal material will not readily grow on the oxide stripes, and instead the semiconductor atoms diffuse and incorporate in areas where the oxide is not present. Consequently, the crystal growth rate and composition between the stripes depends on the stripe separation. This technique is used to achieve band-gap shifts in excess of 100 nm, but suffers from the fact that the thickness and composition vary with distance from the oxide features.

The technique of QWI relies on the interdiffusion of material between the lower and higher band-gap areas to accomplish a local change in band-gap. Generally, the techniques for QWI produce large amounts of band-gap modification, and have a more straightforward implementation which reduces the process complexity compared to selected area regrowth. The area-uniformity of the process is greatly improved over that of selected area-epitaxy. For these reasons QWI is desirable for commercialization and has received much attention in the literature, and a number of different implementations have been reported. A detailed discussion of QWI is presented in Sec. 1.2.1.

The techniques of local-area band-gap engineering are useful to integrate more than just lasers and modulators. A number of different photonic devices that require more than one area of distinct band-gap are desirable. For example, a straightforward extension to the device shown in Fig. 1.4 would be to add a third section, such that a waveguide would be used to separate spatially the laser and modulator, in order to provide greater electrical isolation between these two areas of forward and reverse bias. Detectors can be integrated to monitor the output power of the laser section [9]. High-power semiconductor lasers often fail when the facets overheat; to alleviate this problem the facets can be cleaved from areas which have been band-gap shifted to reduce the absorption and heating at the facets [10]. Band-gap widened regions are useful for lateral current confinement. This has been successfully used to produce VCSELS without etching [11], and to aid the lateral confinement of ridge waveguide lasers [12]. QWI has been useful in reducing the polarization sensitivity of semiconductor optical amplifiers [13]. Array detectors, operating over a range of band-gaps, are used to measure not only the intensity of the incoming signal, but also the wavelength. Conversely,

an array of lasers which emit at different wavelengths can be integrated together. Add to this laser array a set of modulators for each device, and an integrated waveguide coupler, and one would produce an integrated light source where a number of different channels would be combined into the same waveguide, for transmission down a single optical fibre. Such a transmitter would be highly desirable for WDM applications.

To quote from the introduction to the Journal of Selected Topics in Quantum Electronics' issue on QWI technology, photonic integrated circuits hold the key to being able to "fully utilize the enormous bandwidth potential of optical communications..." which "...would lead to revolutionary breakthroughs in the areas of information processing, distribution and manipulation" [14]. The driving force behind these developments is ultimately the internet which is placing ever growing demands on optical networks to supply enormous amounts of data.

1.2 QW Intermixing Techniques

This section discusses how QWI is used to modify locally the band-gap in a device structure. The first part, Sec. 1.2.1 explains how QWI allows the band-gap to be modified. The subsequent sections discuss specific methods to enhance the QWI process and make it area-selective.

1.2.1 What is QWI?

The laser device shown in Fig. 1.3 was fabricated from a series of crystal layers of different band-gap. The injected carriers scatter to occupy the lowest energy states available, principally occupying states within the quantum well (QW) layers. Therefore, it is the band-gap of the QW layer which is related to the emission wavelength of the device. Since the QW has a lower band-gap than the surrounding barriers, the carriers find themselves inside a potential well where their motion is confined in one direction, Fig. 1.5a. This confinement causes the energy of the particle, in this direction, to become quantized: only certain energy values are allowed [4]. The lowest energy level, or "sub-band", corresponds to a value greater

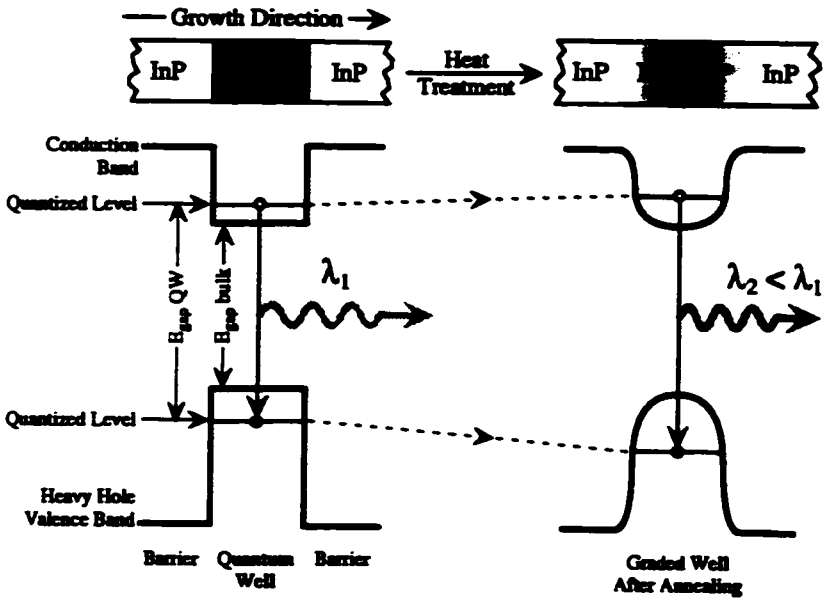

Figure 1.5: Diagram illustrating how the intermixing of the QW and barrier layers produces a blue-shift in the PL emission wavelength. The well on the right corresponds to the sample after heat treatment.

than the bottom of the well, the magnitude of which increases with increasing amount of confinement. Therefore, by changing the width of the QW layer, the composition of the barrier layer, or the composition of the QW layer, the transition energy of the QW is changed since the position of the lowest sub-band inside the well changes.

Post-growth band-gap modification relies on the sensitivity of QW structures to their size and composition. By intermixing the QW and barrier material one changes the profile of the QW from a square well to a well with a graded profile, as shown in Fig. 1.5. The change in profile changes the transition energy of the well, which generally shifts the emission wavelength towards the blue because of both quantum-size effects and compositional changes. QWI is accomplished by heating the structure in a furnace to a temperature which allows atoms to be exchanged between the QW and barrier layers. For optical integration this intermixing process must be locally encouraged in selected areas of the sample; techniques which accomplish this include furnace treatments with patterned dielectric films or localized heat treatments using focused high-power lasers, to name two.

Regardless of the technique used to accomplish the area-selective band-gap modifica-

tion the results must meet certain criteria after intermixing to be useful for optical integration purposes. The process must:

- be controllable and reproducible
- produce sufficient amount of band-gap modification
- maintain the electrical, optical, and crystal quality of the sample
- provide adequate spatial selectivity

The remainder of this section notes specific ways in which area-selective QWI is accomplished. Except for localized heating with a laser beam, all of the QWI methods rely on the introduction of defects into the crystal structure, and a heat treatment. It is often difficult to compare directly results from different groups due to the use of different materials systems, sample structures, preparation of QWI-enhancing layers, annealing techniques, and characterization methods [15].

1.2.2 Zn Diffusion Intermixing

The QWI phenomenon was first reported upon for the case of an AlAs-GaAs superlattice which was locally transformed into an $Al_xGa_{1-x}As/Al_yGa_{1-y}As$ superlattice during a Zn drive in diffusion at 600 °C, due to the diffusion of Al and Ga at the interfaces [16]. This was a significant result since previous studies had shown that the superlattice was thermally stable against interdiffusion up to 900 °C. The process can be made area-selective by using a diffusion mask to determine the areas where Zn intermixes the structure below. Since Zn is an impurity and acts as a dopant in both GaAs and InP-based materials, the Zn drive-in intermixing is not a good technique for preserving the electrical properties of the material, and obtaining low optical loss samples.

1.2.3 Ion Implantation Intermixing

Crystal damage induced by ion-implantation is useful in enhancing QWI [17]. The implant is followed by a thermal anneal which restores the crystal quality and allows the defects to diffuse to the QWs and promote intermixing. The amount of blue-shift depends on implant species, implant energy, and implant dose. In InP-based materials, P atoms are

typically implanted at several MeV and produce blue-shifts of over 70 nm. Area-selectively is obtained by using a thick dielectric layer to mask selected areas from being implanted. By controlling the thickness of mask one can control the implant damage, and, therefore, control the amount of blue-shift that a certain area experiences.

1.2.4 Laser-Heating-Induced Intermixing

Laser-heating-induced intermixing is the one QWI process which does not require the introduction of defects to achieve area-selectivity [18]. A high-power tunable cw laser is used to generate carriers locally in the active region by tuning the laser near to the emission wavelength of the structure. This causes localized heating resulting in a localized intermixing process. Metallic masks, such as Au, are useful in defining the affected regions, but the area-selectivity is poor due to the thermal conductivity of the sample. Pulsed-laser intermixing techniques are also used; they rely on a different mechanism. High-intensity short pulses cause thermal shock in the sample thus producing defects. These defects can be subsequently used to promote QWI [18].

1.2.5 Dielectric-Enhanced Intermixing

Dielectric-enhanced QWI is of particular interest because the deposition and etching of dielectric films is standard in typical fabrication sequences. Studies have been performed on various types of dielectric encapsulants, and in many cases the presence of a dielectric film is seen to enhance the intermixing process when the sample is thermally annealed. The process is made area-selective by patterning the dielectric film before anneal. Typically, dielectric films ranging from SiO_2 to SiN_x are deposited using plasma-enhanced chemical vapor deposition (PECVD). The generally accepted intermixing mechanism is that at the anneal temperature Ga migrates from the semiconductor into the dielectric film, which in turn produces a non-equilibrium concentration of Ga vacancies [19] in the crystal which enhance the intermixing process at high temperatures [20]. The specific results depend on film composition, deposition conditions, deposition technique, film thickness, anneal temperature, and anneal time. Large amounts of QWI, in excess of 100 nm, are possible with this process.

Some dielectric films can be used to inhibit the intermixing process, like SrF_2, AlF_3, and high quality SiN_x [21]. This effect is though to be a consequence of these materials inhibiting the migration of Ga and thereby suppressing the production of excess Ga vacancies.

1.2.6 Intermixing Using Unusual Epitaxial Layers

Unusual epitaxial layers have recently become available in the InP system to promote QWI during high-temperature anneal treatments. The growth of crystal layers under unusual circumstances incorporates defects which are used to influence the intermixing process. If these layers are grown on the top of the structure they may be patterned, and upon anneal produce an area-selective band-gap modification. There are two novel InP-materials that have been shown to be useful in this manner.

The first type of material is InP grown in the presence of a He plasma by MBE. This is referred to as He*-InP. Although the mechanics of the process are not yet fully understood, it is believed that vacancies present in the material diffuse into the crystal structure below and enhance the intermixing process [22]. The process produces adequate blue-shifts, and under certain circumstances the migration of defects quenches the luminescence of the QWs. The other unusual epi-layer is low-temperature grown InP (LT-InP). The defects are believed to be phosphorus antisites incorporated during the growth. The process produces large blue-shifts at modest anneal temperatures of 700 °C [23].

1.2.7 Sputtering Damage Induced Intermixing

Surfaces damaged by RF sputtering have been observed to enhance the QWI process. Studies based on sputtered SiO_2 films, [18], showed that samples (heat treated with the SiO_2 film either present or etched off) underwent large blue-shifts compared to samples which had not experienced the sputter deposition process. The process can be made area-selective by using a mask composed of PECVD SiO_2 and photoresist to protect selected areas of the sample from the sputtering. Heat treatment of the material produces blue-shifts at temperatures significantly lower than the other processes discussed, with shifts as large as 170 nm.

1.3 Project Motivation

The majority of QWI studies have been in the GaAs-based materials system. However, it is the InGaAsP/InP materials system which is the basis for current telecommunications emitters and detectors. This is because the materials can be used to produce efficient optical devices that operate at 1550 nm, which corresponds to the low attenuation window in silica optical fibres. Much work in this wavelength range has been on InGaAs/InP QWs (see for example [24]), a more straightforward system than InGaAsP/InGaAsP, but not as widely used in commercial or practical optoelectronic devices. Work has also been presented on InGaAs wells with InGaAsP barriers. Even so, many QWI studies have been done on superlattices or undoped structures, and are therefore not immediately applicable to the production of integrated devices.

A much smaller body of work exists for InP-based quaternary-quaternary heterostructures, and to our knowledge no comprehensive survey has yet been published. Wyllie [25] discusses the behavior of unstrained and tensile-strained heterostructures annealed between 700 to 800 °C. Lam [26] discusses the Ar-plasma implantation of MOVPE-grown structures ($\lambda = 1.3\,\mu$m) with a constant In/Ga concentration, at an anneal temperature of 650 °C. Noel [27] discusses the P implantation of MOCVD-grown structures ($\lambda = 1.31\,\mu$m), at an anneal temperature of 700 °C, and the subsequent fabrication and characterization of ridge-waveguide lasers. Ion implant studies have also been done on QWs that were compressive-, tensile-, or un-strained [28, 29], and studied using degree of polarization photoluminescence after annealing at 750 °C for 30 s. The intermixing of all-quaternary active regions ($\lambda = 1.55\,\mu$m) using a phosphorus-doped oxide film has been studied [30, 6] and used to produce an integrated DFB laser-modulator. Heterostructures with a constant P/As ratio in compressively-strained QWs and tensile-strained barriers have been studied [31, 32, 33] with the aim of determining the Group III interdiffusion coefficient. Other all-InGaAsP heterostructures (but not laser structures) were studied in [33], consisting of -0.75 % compressively strained QWs of 4.4 and 8 nm thicknesses, although this work was restricted to an anneal temperature of 850 °C. The study in [31] is restricted to 850 °C, where [32] ranges

from 650 to 950 °C. PECVD SiO_2-capped all-quaternary heterostructures were examined [34] at an anneal temperature of 650 °C for 120 minutes under different phosphorus pressures. The oxide film was simply used to protect areas of the sample from the phosphorus atmosphere, and resulted in the bare regions experiencing a larger blue-shift, dependent on the phosphorus over-pressure.

SiO_2 films have received a lot of attention, and SiN_x films have been used to suppress the QWI process. However, little work has been presented for SiO_xN_y films. The use of different composition or thickness films to produce different amounts of QWI is highly desirable for optoelectronic integration purposes. A study of different film compositions and deposition methods in GaAs/AlGaAs and InGaAs/GaAs [15] has been presented, but to our knowledge there has not been an investigation of these films published in the InP materials system. The PECVD SiO_xN_y films studied in [15] range in refractive index from 1.4 to 2.5; this index variation suggests that the film stoichiometry is poor. The investigation is done only at 925 °C for 60 s, and shows that the magnitude of the band-gap shift increases with the oxygen content of the film. The migration of Ga from GaAs into SiO_xN_y films has been characterized by SIMS [19], showing that the migration decreases with increasing N content. SiO_2 films on InGaAs/InGaAsP MQW structures have been studied [35] between 600–800 °C and were shown to exhibit shifts in excess of 100 nm at anneal temperatures as low as 650 °C, preferably when the dielectric is in contact with InGaAs. There does not appear to have been a consistent study of dielectric-capped intermixing in the InGaAsP/InP system with regard to dielectric composition or device structure.

Of the methods that allow the band-gap of a semiconductor material to be selectively controlled across the wafer, dielectric-enhanced band-gap shifting is a promising method for accomplishing this. The advantages of using dielectric films is that they are already a standard part of fabrication sequence. The band-gap can be patterned without the need of any complicated equipment such as a high-power laser system or ion implanter. All that is required is the heat treatment of the sample with a patterned dielectric film. No non-native impurities are introduced, unlike the Zn diffusion process. The drawback is that variations

in the deposited films affect the results of the band-gap shifting process.

1.4 Outline of Thesis

This thesis presents dielectric-enhanced quantum-well intermixing (QWI) studies of InGaAsP/InP-based $\lambda = 1.55\,\mu$m laser structures for photonic integration.

Chapter 2 presents the different laser structures studied, as well as the growth methods used to prepare the dielectric capping films. The chapter concludes with a description of the furnace setup used to heat treat the samples.

Chapter 3 outlines the different characterization methods used to measure the amount of band-gap shift and to better understand the nature of the dielectric-enhanced process.

Chapter 4 discusses the results of heat treating both bare and oxide-capped specimens. The goal is to compare the thermal stability and behavior of the various laser structures and to characterize the effect on the samples using photoluminescence.

Chapter 5 discusses the band-gap shifting results for different kinds of dielectric films, and the materials characterization of these films. Dielectric caps including spin-on glass and PECVD SiO_xN_y films of varying composition are examined. PECVD films of differing thickness are also examined. The emphasis is on photoluminescence characterization. The remainder of the chapter presents the results of experiments designed to elucidate the mechanism by which the dielectric caps promote intermixing. Principally, the data presented is an examination of the dielectric film by SIMS, FTIR, and film stress measurements. The film-semiconductor interface is examined by TEM and AFM. These results are then used to propose a mechanism by which the dielectric film promotes the interdiffusion of QW in the InGaAsP/InP based system.

Chapter 6 discusses the results that have direct bearing on using this process as a means to accomplish optoelectronic integration. Issues such as the absorption characteristics, etching behavior, spatial selectivity, and regrowth properties are examined.

The results are summarized in Chapter 7, together with a summary of original contributions in this thesis and suggestions for further research.

Chapter 2

Sample Preparation

Introduction

This chapter presents aspects regarding sample preparation. Section 2.1 discusses the growth and geometry of the various laser structures studied. Table 2.1 is a summary of device structures. The deposition of spin-on glass (SOG) and PECVD films is presented, with special attention paid to the PECVD deposition conditions in Section 2.3. This discussion includes characterization results of the as-deposited films. Discussion of the characterization methods is found in Chapter 3. The chapter concludes with a discussion of the rapid thermal annealing (RTA) processing method used to heat treat the samples.

2.1 Laser Structures

2.1.1 Generic Active Region

The majority of laser structures studied in this thesis have a common active region structure. This common structure is then finished with additional layers depending on whether it is a full or partial laser, which will be discussed in Sec. 2.1.2. The common active region consists of quaternary layers grown by GSMBE on n-type S-doped (001) InP substrates at 470 °C (all layers), as shown in Fig. 2.1. The active region is composed of three 1.1 % compressively strained 50 Å QWs of $In_{0.76}Ga_{0.24}As_{0.85}P_{0.15}$ and two 100 Å barriers of lattice-matched $In_{0.76}Ga_{0.24}As_{0.52}P_{0.48}$. Both the QWs and the barriers are undoped, and compositions have been chosen such that the In and Ga compositions are identical. The

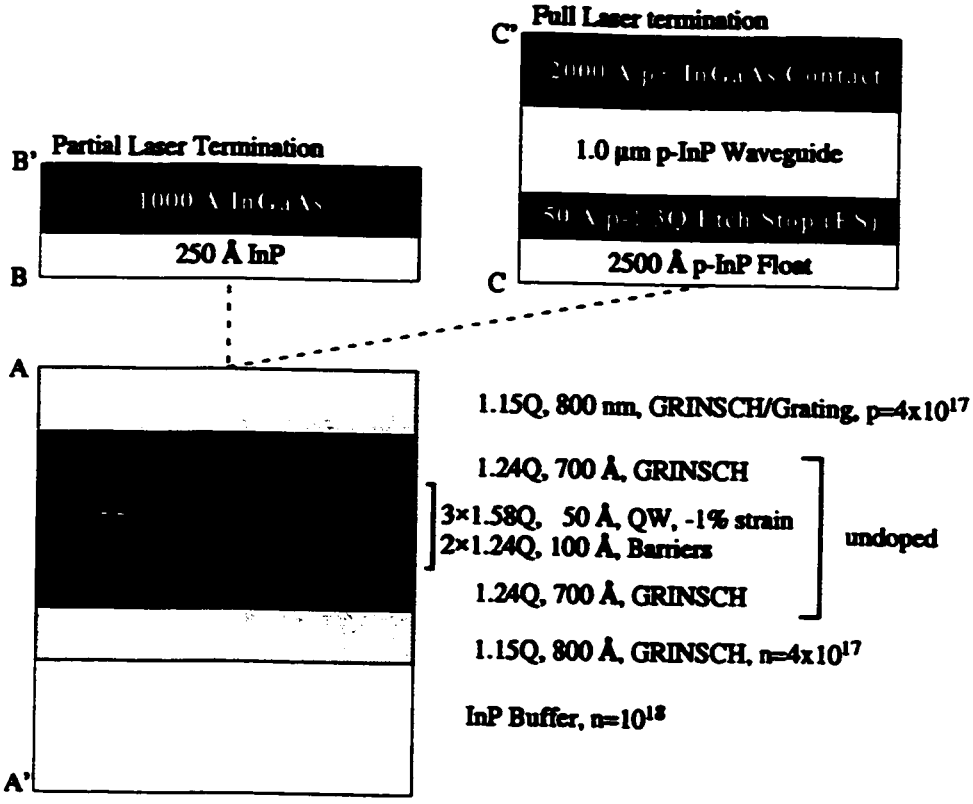

Figure 2.1: Diagram showing sample layer structure. The generic active region consists of the layers below A–A'. Building upon this basis, depositing layers B–B' produces a partial structure, while depositing layers C–C' produces a full structure.

1.24 Q and 1.15 Q layers above (p-doped, Be) and below (n-doped, Si) the active region are graded-index separate-confinement heterostructure (GRINSCH) waveguiding layers.

Figure 2.2a shows the calculated positions of the QW energy levels in the as-grown active region for the compositions noted above. Details of the calculations are found in [36]. The confinement profiles of the QW result in the conduction band (CB) level situated 33 meV below the barrier, heavy hole (HH) levels lying 185 meV and 114 meV above, and a light hole (LH) level lying 65 meV above the barrier. As a first approximation to determine the emission wavelength of "heavily" intermixed QWs one may consider the full homogenization of the three QWs with the equivalent of four barriers. This results in a 550 Å thick layer of $In_{0.76}Ga_{0.24}As_{0.61}P_{0.39}$ which is 0.3 % compressively strained. Including both strain and quantum-size effects the material would emit at 1322 nm resulting in a band-gap shift of $\approx$ 260 nm. Since the layer is so wide there are numerous CB, HH, and LH levels present, as

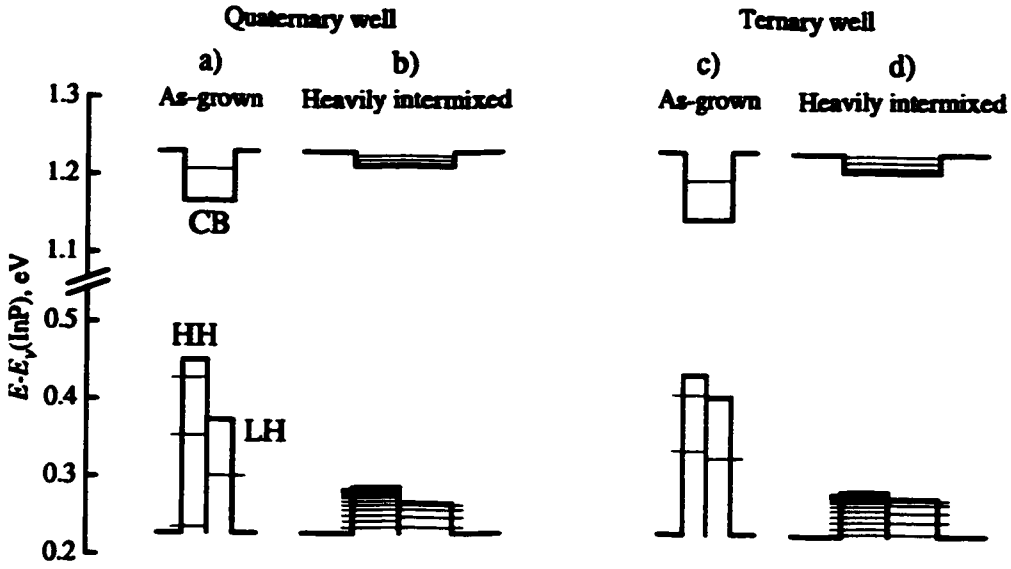

Figure 2.2: Diagram showing QWs in structure for (a–b) quaternary QW, (c-d) ternary QW; b,d) are heavily intermixed QWs.

shown in Fig. 2.2b; consequently the density of states (DOS) will begin to approach that of bulk material. Blue-shifting will occur beyond this wavelength by intermixing further into the barrier regions, but it is likely that this process will proceed at a slower pace.

In the above discussions, each layer of $In_{(1-x)}Ga_xAs_yP_{(1-y)}$ is considered to be a homogeneous alloy with the Group III and V atoms randomly distributed on their respective sub-lattices. However, not all compositions of $In_{(1-x)}Ga_xAs_yP_{(1-y)}$ find this configuration thermodynamically stable and, consequently, they tend to segregate into regions that are InAs- or GaP-rich. This behavior is called either lateral composition modulation (LCM) or spinodal decomposition, and is caused primarily because of the large difference in bond-length between the four binary components that can be considered to compose the quaternary material. The spinodal isotherms, shown in Fig. 2.3, describe the boundary between stable and unstable (inside the curve) bulk $In_{(1-x)}Ga_xAs_yP_{(1-y)}$ at a specified temperature under equilibrium conditions [37]. The entropy of the system increases with increasing temperature, which in turn favors more random atomic arrangements, and the isotherm consequently encompasses a smaller range of compositions. The InAs- and GaP-rich regions are typically 100×1000 Å in area [38], occur in pairs, and run parallel to the growth direction.

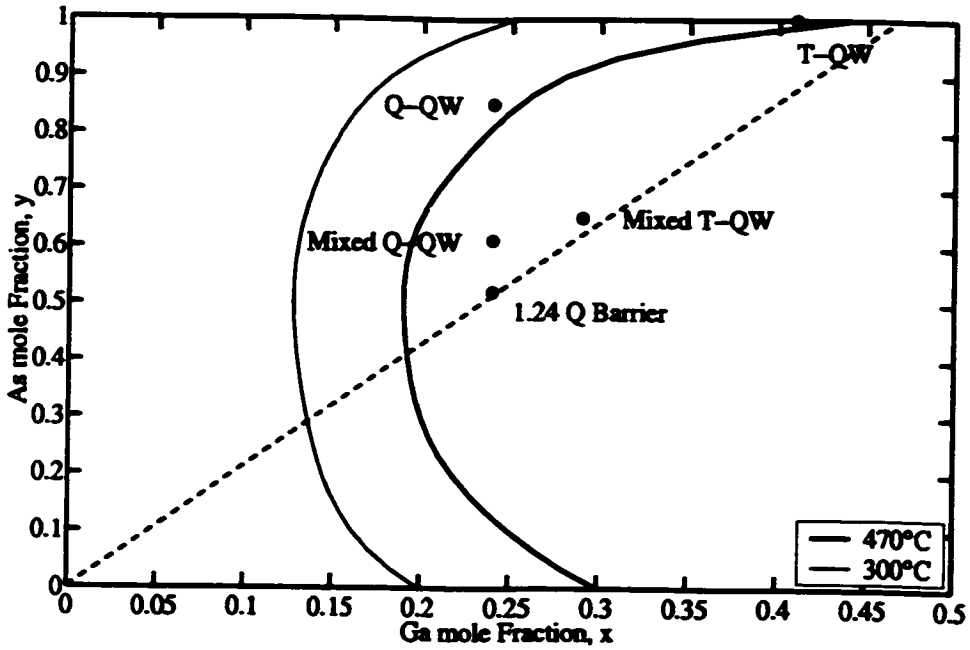

Figure 2.3: Compositional diagram for InGaAsP, indicating lattice matching to InP (dashed line), the coordinates of QW and barrier material considered in this thesis, and the equilibrium bulk spinodal isotherms for temperatures of 300 and 470 °C.

2.1.2 Full Versus Partial Laser Structures

A Fabry-Perot structure is created in one growth sequence by placing the layers C–C' over A–A' (see Fig. 2.1); this is a full laser structure. The heavily doped InGaAs layer is used to provide an ohmic contact. The thick layer of InP that comprises the majority of the regrowth will become a ridge waveguide providing lateral optical and current confinement. The etch stop layer is used to maintain the thin "float" layer of InP necessary for the optical waveguide. Distributed feedback (DFB) lasers are particularly valuable in present day long-haul communications systems due to their wavelength stability. The key to their improved characteristics over Fabry-Perot devices is a grating that is etched into the top 1.15 Q GRINSCH layer, the rulings of which run perpendicular to the laser cavity [39]. In order to fabricate such a device with an embedded grating, the laser growth must be interrupted, the grating patterned ex-situ, and the sample returned to the GSMBE chamber to be completed by growing the C–C' layer structure (Fig. 2.1). Figure 2.4 is a simplified illustration of how a grating-based device is created. First the partial structure through B–B'

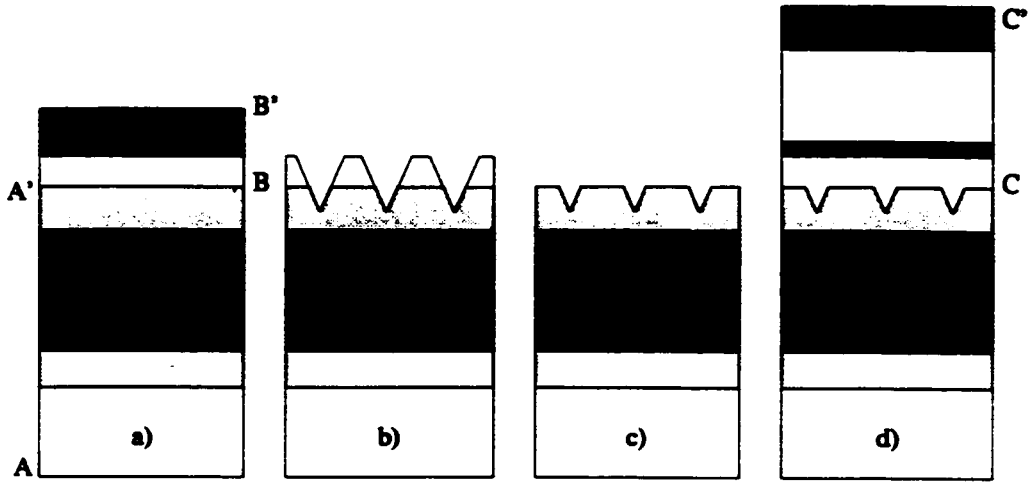

Figure 2.4: How a grating is placed into the structure. (a) partial laser structure as-grown, (b) InGaAs removed and grating etched, (c) removal of InP and sample cleaning, d) regrowth over grating to create equivalent grating-based structure. Please refer to Fig. 2.1 for layer details.

is grown. The top protective layer of InGaAs is then etched off and a grating is patterned by wet chemical etching [22]. Next the top-most discontinuous layer of InP is etched away and the sample cleaned. Finally, the layers above C–C' are regrown over the grating to complete the equivalent grating based structure.

There are two windows of opportunity to apply the QWI process during the creation of a grating-based device as shown in Fig. 2.4. The first opportunity is at step (a) after the initial partial laser growth. The other opportunity is after step (d) once the regrowth is complete. In either case, samples are terminated in InGaAs, the reasons being the increased thermal stability of InGaAs over that of InP allowing the study of higher temperatures needed for the dielectric process, and the need for Ga in the topmost layer which will out-diffuse into the dielectric as part of the enhanced QWI process.

Each window of opportunity has its own advantages and pitfalls. Our studies of dielectric-enhanced QWI on material that has been grating-patterned and regrown have not produced consistent results. We believe that interfaces or defects resulting from the grating pattering and regrowth process are acting as sinks and sources of defects, and are responsible for the variable results. We have therefore concentrated our efforts on the application of the dielectric-enhanced process on partial laser structures. Although this approach is not without

MBE #	InGaAs Å	InP μm	ES Å	Float Å	QW	Buffer μm	Substr. Doping	RTPL λ nm
2826	2000	1.45	50	1000	InGaAsP	0.75	Zn (p)	1559
2827	2000	1.45	50	1000	InGaAsP	0.75	S (n)	1560
2880	2000	1.00	50	2500	InGaAsP	0.50	S (n)	1571
2881	2000	1.00	50	2500	InGaAsP	0.50	S (n)	1575
2885	1000	–	–	250	InGaAsP	0.50	S (n)	1575
2888	1000	–	–	250	InGaAs	0.50	S (n)	1581
2958	1000	–	–	250	InGaAsP	0.50	S (n)	1578

Table 2.1: Summary of device structures. Layers are as defined in Fig. 2.1.

its difficulties (see Sec. 6.2.2) it provides a solid basis from which to work.

2.1.3 p- Versus n- Substrates

A pair of full laser structures was grown (MBE# 2826 & 2827), identical in every way except for the doping profiles. Sample 2826 has a p-doped (Zn) substrate (as opposed to the standard S-doped substrate). Consequently the doping type of the epitaxially-grown layers switched. The substrate doping levels are typically $5 \times 10^{18}/\text{cm}^3$. This was done to determine what effect the doping sense had on the dielectric-enhanced QWI process.

2.1.4 Ternary QW

The effect of QW composition was studied using wells composed of 0.4% compressively strained $In_{0.59}Ga_{0.41}As$. This composition was chosen so that the as-grown QWs emitted light at 1575 nm, consistent with the other structures. The QW energy solutions are shown in Fig. 2.2c–d. Intermixing with four barriers creates material of composition $In_{0.71}Ga_{0.29}As_{0.65}P_{0.35}$ which is 0.1% compressively strained. Including strain and quantization effects, an emission wavelength of 1334 nm and a maximum blue-shift of $\approx$ 245 nm is expected.

2.2 Deposition of Spin-On Glass

Spin-on glass (SOG) is a commercial product used to produce insulating and planarizing films for semiconductor device processing. Allied Signal Accuglass T-111 Spin-On

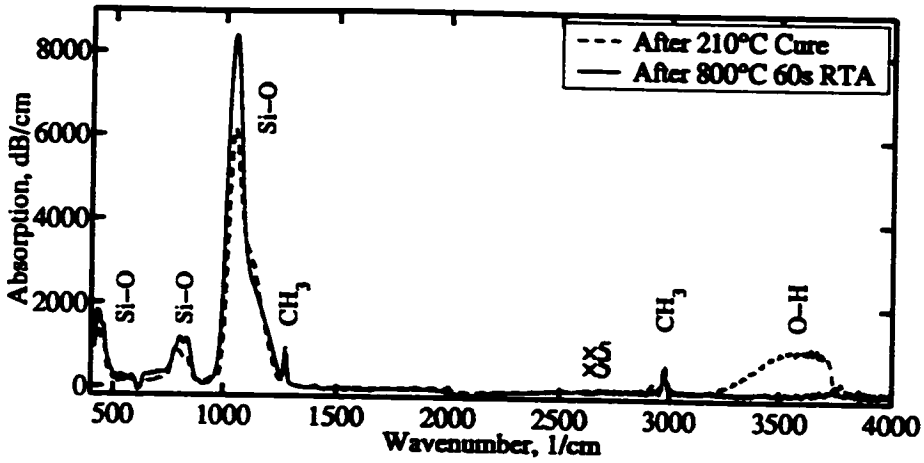

Figure 2.5: FTIR spectra of SOG films before and after annealing. The right-hand portion of the spectra are enlarged by a factor of 5.

Glass consists of a Si–O–Si polymer back-bone with organic groups contained in a solvent base. Films are prepared by spin coating the substrate material at 4000 rpm for 30 s. The films are cured by baking in an oven at 210 °C for 24 hours after a 1 hour ramp up period. The curing procedure drives out hydrogen (H) and creates a denser film approximating that of SiO_2, but with an 11 % CH_3 content [40]. After curing, the films exhibited a thickness of 1084 Å and a refractive index of 1.422. Since these films are designed to be cured at 400 °C, a significant H content remains. This is evidenced by the H absorption band around 3500 cm^{-1} as measured by Fourier transform infrared spectroscopy (FTIR), shown in Fig. 2.5. FTIR measurements are discussed in more detail in Sec. 5.4.

2.3 Deposition of PECVD SiO_xN_y

SiO_xN_y films were deposited in a Technics Micro-PD Series 900 PECVD system. The deposition is accomplished by leaking controlled amounts of process gases (SiH_4, N_2O and NH_3) into a stainless steel vacuum chamber and decomposing them with an RF microwave field. The fragments of the decomposed process gases react on the sample and chamber surfaces to create a film whose composition and properties depend on the process parameters. The oxynitride composition is controlled by adjusting the relative amounts of N_2O and NH_3.

The process gases enter the chamber through holes around the rim of the 9 inch

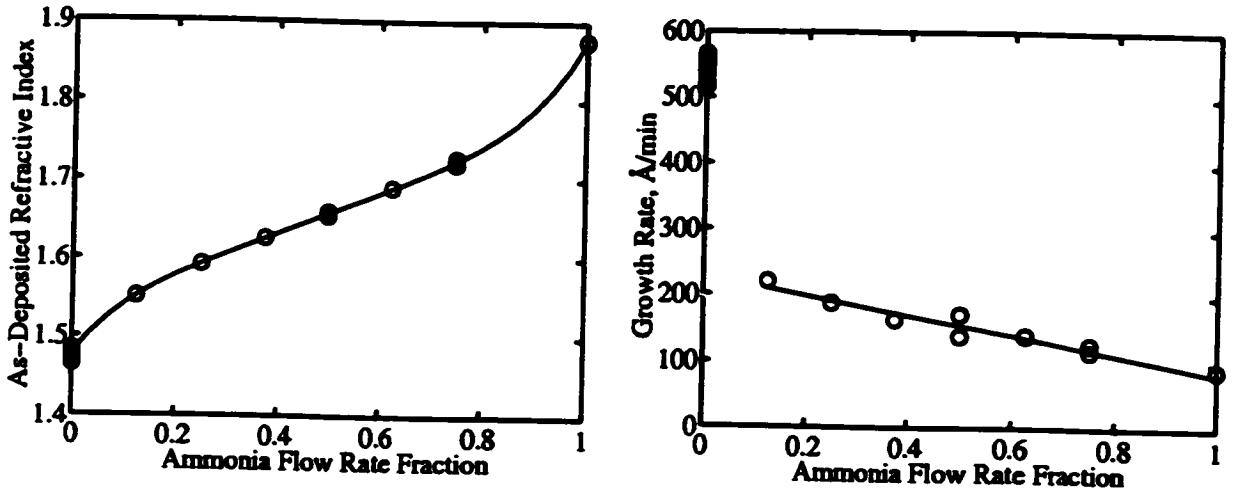

Figure 2.6: Deposition results of SiO_xN_y films.

diameter platen. The platen has been modified with a stainless steel collar whose 3 inch diameter center hole is designed to enhance deposition uniformity by concentrating the gases over a smaller area around the sample. Process parameters were optimized to produce uniform films (< 10 Å over a 2 inch wafer) low amounts of H incorporation.

The flow rates of the precursor gases are chosen such that SiH_4 is the limiting reagent for the oxide growth. In this way an abundance of O and/or N is provided in the chamber allowing easier control of the growth rate and composition. SiO_xN_y films are deposited using 100 sccm of 5% SiH_4 diluted in Ar and 60 sccm of a N_2O-NH_3 mixture, with chamber conditions of 300 °C, 650 mT, and 50 W RF power (30 kHz). The composition of the mixture determines the film composition and deposition rate, as shown in Fig. 2.6. A near-oxide film is obtained from a mixture of SiH_4 and N_2O; a near-silicon-nitride film is deposited from SiH_4 and NH_3. Thermally grown oxide and nitride films have indexes of 1.46 and 2.05, respectively.

SiH_4 is a pyrophoric molecule which for safety is diluted in Ar. It reacts much more strongly with O than N, resulting in the higher deposition rate for oxide films. The reason why near oxide films are obtained from SiH_4 and N_2O alone is that even when the N≡N–O molecule completely decomposes, the abundance of available O dominates the process. N_2 formed during this time is extremely inert and difficult for the low power RF plasma to

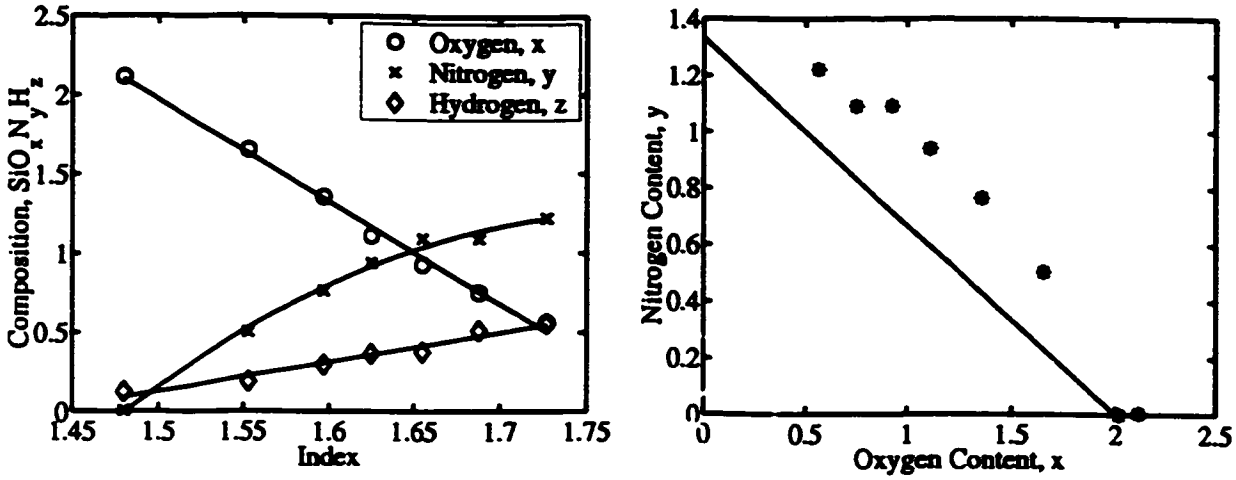

Figure 2.7: Composition of SiO_xN_y films (a) as determined by Auger and FTIR analysis, (b) comparison of composition to linear interpolation between SiO_2 and Si_3N_4.

decompose. NH_3, on the other hand, is much more likely to decompose and yield N or N–H_x fragments which incorporate into the film.

The samples were analyzed by the technique of Auger spectroscopy [41] to determine the relative atomic concentrations of Si, O, and N. The results are presented in Fig. 2.7 for films that have been annealed at 800 °C for 60 s. The line drawn on Fig. 2.7b corresponds to the interpolation $SiO_xN_y = (SiO_2)_x(Si_3N_4)_{1-x}$, indicating that the stoichiometry is poor, likely the consequence of the H content of the film, as determined by FTIR (see Sec. 3.4 and 5.4). The H content is unavoidable due to the large amount of H in the SiH_4 and NH_3.

It is also possible to manipulate the film composition using only SiH_4 and flow rates of N_2O that starve the process of O. This encourages the incorporation of N, creating SiO_xN_y films. However, excess Si is incorporated into the film when the flow of N_2O is too low. Evidence of excess Si includes film refractive indexes larger than 2, extremely low etch rates, and FTIR features indicating large amounts of Si–H incorporation. SiO_xN_y films were deposited by this technique using 2% SiH_4 in N_2 and flow rates of N_2O from 8 to 60 sccm. Films deposited both with and without NH_3, over the range of n=1.48–1.75, were compared by Auger, etch rate, and FTIR and found to be very similar. QWI experiments using SiO_xN_y films deposited using only N_2O produced blue-shifts of similar but lower magnitude. The QWI results of SiO_xN_y films grown using only N_2O will be explicitly noted in the sections

where presented. Si-rich films were not studied due to their awkward sample preparation and etching, placing them outside the realm of a standard micro-fabrication processing sequence.

2.4 Rapid Thermal Annealing

We use an AG Associates model 610 Mini-Pulse rapid thermal annealing (RTA) furnace with a flowing ambient of N_2 gas. The samples are contained within a 3.25 inch graphite boat sandwiched face-down between either Si, GaAs, or InP proximity caps. We find that the proximity cap material does not affect our results, and therefore we typically use Si. The temperature is measured by a K-type thermocouple embedded in the graphite boat. Samples are annealed at temperatures of 600–820 °C for durations of 10 s to 20 minutes. To achieve optimized temperature profiles, the furnace is stabilized at 300 °C for 60 s and then ramped at 25 °C/s to the set-point temperature. We conservatively estimate a scatter of ±2 s and ±3 °C on the furnace treatment, a consequence of the control stability of the furnace heating and stabilization cycle.

Chapter 3

Characterization Methods

Introduction

This chapter details the characterization methods and the data analysis which are used for the bulk of the work presented in this thesis. Section 3.1 discusses the photoluminescence measurements. Secondary ion mass spectrometry was used to study the migration of Ga and In into the dielectric films. Ellipsometry, FTIR, and film stress measurements were used to characterize the dielectric films. The chapter concludes with the technique used to measure the optical absorption of waveguide devices.

3.1 Photoluminescence Spectroscopy

Photoluminescence spectroscopy (PL) is the technique of optically exciting electron-hole pairs in a material, and then monitoring the spontaneous emission luminescence spectrum from the sample caused by the recombination of these excess carriers. A pump laser, with photon energies greater than the band-gap of the semiconductor, is used to generate the excess carriers. By phonon scattering, these carriers relax towards the band minima and assume a thermal distribution in their respective bands. In the most simple approximation for a direct band-gap semiconductor, the spontaneous recombination of electrons and holes creates photons of energy corresponding to the band-gap and several kT above because of the thermal populations. A monochromator is used to analyze this light which produces spectra similar to those shown in Fig. 3.1. The analysis of these spectra provides information about

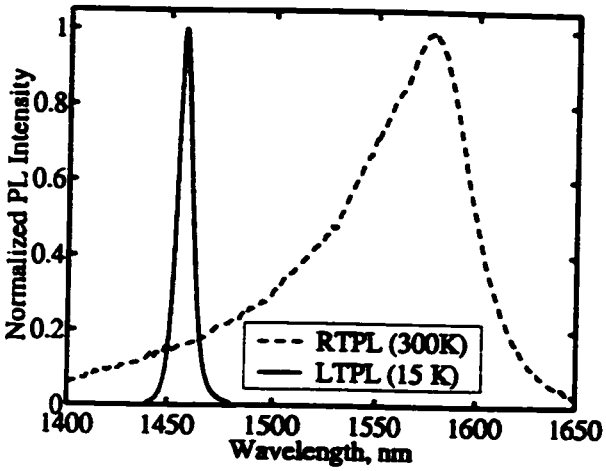

Figure 3.1: Comparison of LTPL and RTPL spectra for MBE# 2958 as-grown.

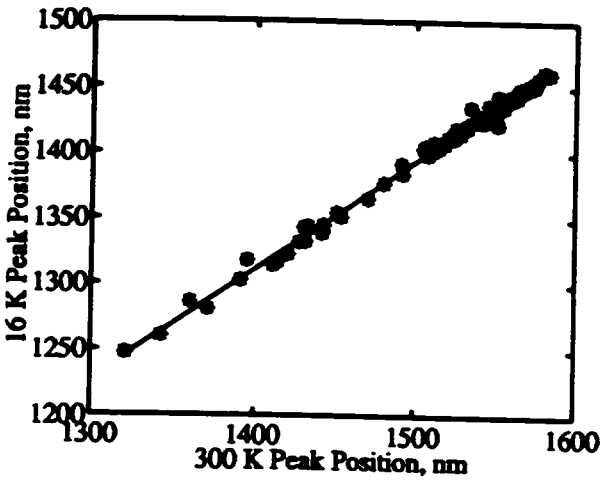

Figure 3.2: Comparison of LTPL and RTPL peak wavelength position.

the band-gap and material quality of the sample.

The sample temperature, and consequently the thermal distribution, greatly influences the appearance of the PL spectra and the information obtainable from it. Figure 3.1 illustrates the effect of temperature on PL spectra. Room-temperature PL (RTPL) measurements provide useful information about the band-gap and optical quality of the sample at the temperature where devices fabricated from such samples would be designed to operate. At room temperature $kT = 24\,\text{meV}$; therefore, the RTPL spectra will be wide ($1.8\,kT$, [37]).

Low-temperature PL (LTPL) measurements at 15 K provide a different view of the sample. The reduced temperature causes the crystal lattice to contract and, consequently, the band-gap increases in energy. The thermal population effects are also greatly reduced since $kT = 0.5\,\text{meV}$. The resulting spectral features occur at shorter wavelength and are much sharper. Consequently, new features associated with material defects become discernible in the spectra. The presence of impurities creates localized levels inside the band-gap manifested as a low-energy tail on the PL spectra. QW roughness or inhomogeneous material composition (due to lateral composition modulation [37]) causes localized band-gap fluctuations and, hence, broadened PL spectra. Because there is a direct correspondence between the LTPL and RTPL peak position, as shown in Fig. 3.2, only the RTPL blue-shifts will be presented and discussed in the text; the LTPL linewidth is used to examine material quality.

Our PL test setups use either a HeNe or a Ar-ion laser as an excitation source. The monochromator wavelength resolution is better than 1 nm. An InGaAs photodiode is used to detect the light. An Oriel model 63358 calibrated white-light source was used to determine the wavelength response of the system; this correction was relatively insignificant over the working wavelength range of 1300–1620 nm. To reduce atmospheric water absorption in the vicinity of 1400 nm, the monochromators are purged with dry N_2. Laser intensities are low enough to avoid band-filling artifacts. Further details of the experimental setups are given elsewhere [37]. In order to facilitate PL measurements, the top layers of the sample are chemically etched away to expose either the 1.15 Q top waveguide layer or the etch stop layer. Without this step the pump laser intensity is insufficient to produce adequate luminescence from the samples because the pump beam is strongly attenuated by the semiconductor material. Due to difficulties in apparatus alignment, LTPL intensities are not suitable for comparison; RTPL measurements provide useful intensity data if the sample group is tested together, having allowed the pump laser more than one hour to warm up.

The PL spectra are analyzed by fitting a polynomial to determine the peak PL intensity and wavelength. The PL linewidths are calculated by fitting polynomials to the edges of the PL spectrum and determining the wavelengths that correspond to half the peak intensity.

3.2 Secondary Ion Mass Spectrometry

Secondary Ion Mass Spectrometry (SIMS) measurements provide a way to profile material composition versus depth, and are particularly good at detecting trace elements in a matrix where other techniques are not as sensitive [41]. For this reason we have used SIMS to examine the migration of semiconductor material into the dielectric film following the QWI heat treatment.

In a SIMS measurement energetic ions are used to sputter the sample. This causes the creation of ionized sputtering products characteristic of the material being studied. A mass analyzer is used to monitor the ionized species as a function of sputtering time. In this way a compositional depth profile of the sample is obtained. In a multi-layer sample the

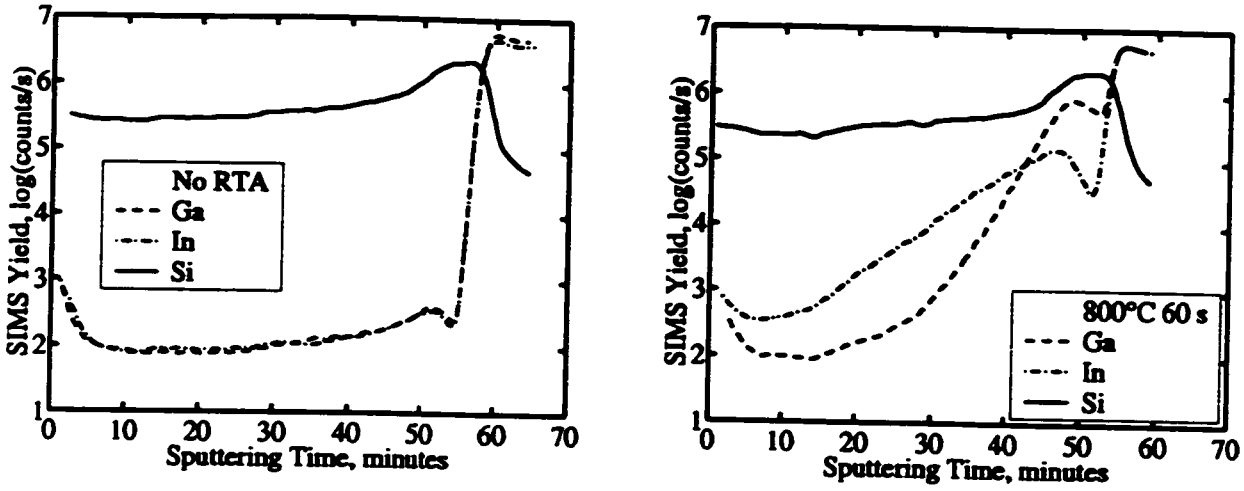

Figure 3.3: Raw SIMS data for a SiO_xN_y film of n = 1.61; (a) as-deposited, and (b) annealed at 800 °C for 60 s.

sputter time is transformed into a distance scale from knowing the layer thicknesses and by reference to when these interfaces appear in the SIMS data.

In our experiments 4 keV oxygen is used for sputtering. The mass analyzer monitors Si, In, Ga, As, and P. The use of oxygen as a sputtering agent is intended to saturate the process ionization yield and so that the oxygen content of the dielectric films does not influence the results. Samples intended for SIMS analysis must be annealed using Si caps (as opposed to GaAs or InP) to reduce III-V contamination on the top surface of the dielectric film.

Figure 3.3 shows raw SIMS data for Ga, In, and Si obtained from a SiO_xN_y films, both as-deposited and annealed at 800 °C for 60 s. There appears to be a local enhancement of the signals near the interface between the dielectric and the semiconductor. This is most apparent in the Si trace, and has been noted before [42] in SiO_2/Si samples where it was found to be indicative of the interface position. Auger depth profiles show that the dielectric composition is constant throughout the film, indicating that this feature is a SIMS measurement artifact. We therefore believe that it is useful to divide all other traces by the Si signal to remove this artifact. We note that after applying this Si reference technique this area is flattened, as shown in Fig. 3.4 for the same two samples combined. This figure also shows the time scale shifted with respect to the distance from the semiconductor-SiO_xN_y

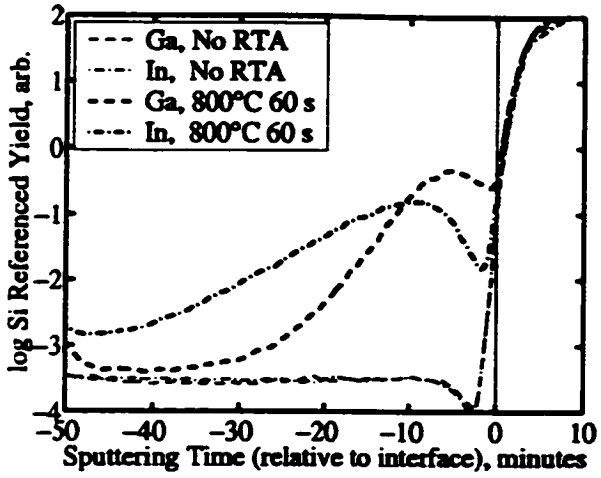

Figure 3.4: SIMS data for a SiO_xN_y film of n = 1.61, referenced to the Si signal and interface position for the samples shown in Fig. 3.3.

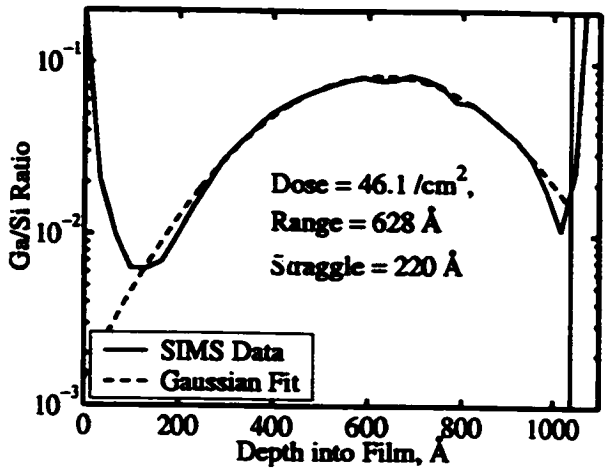

Figure 3.5: SIMS profile of Ga implant sample with Gaussian fit.

interface, by estimating the position of the film-semiconductor interface to be where the edge of the non-annealed sample is.

In order to quantify the sputtering yield, a calibration sample was prepared by implanting a dose of 9.6×10^{14} Ga/cm^2 at 80 keV into an n=1.605 SiO_xN_y film (prepared by the low N_2O flow technique). An inspection of the SIMS profile, Fig. 3.5, shows a deep implant with a Gaussian distribution and large straggle, after correction by the Si reference technique discussed above. The fact that the measured implant distribution appears Gaussian over a much increased range after the Si reference technique is applied lends added credibility to the Si reference technique. The measured implant profile was integrated and compared to the known Ga implant dose; the resulting calibration factor was found to be 1.84×10^{13}/cm^2. For example, in Fig. 3.4 the Ga concentration near the SiO_xN_y-semiconductor interface corresponds to $\approx 2 \times 10^{20}$/cm^3.

3.3 Elipsometry

Film-thickness measurements are made using a Rudolph Research AutoEL elipsometer with a 633 nm HeNe laser and an incidence angle of 70° to the surface normal. This configuration corresponds to a high accuracy in measuring the parameters of 1000 Å SiO_xN_y

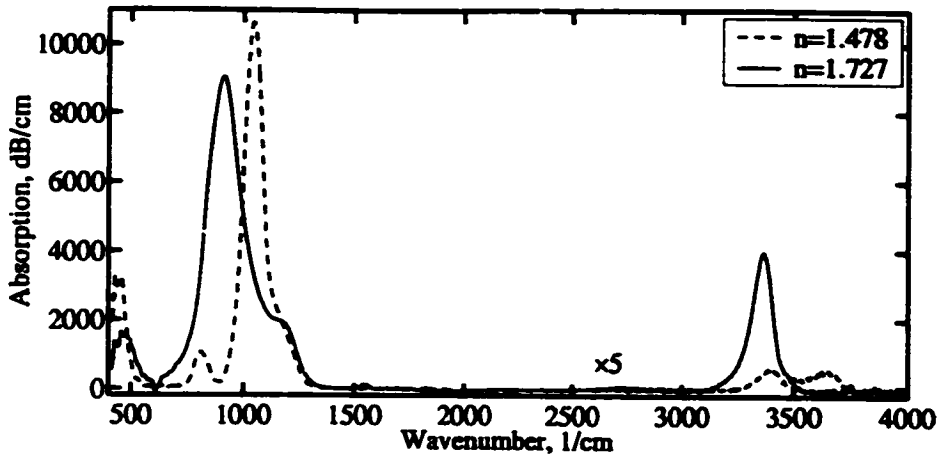

Figure 3.6: FTIR spectra for as-deposited PECVD dielectric films.

films on Si or InP substrates. The typical measurement scatter is ± 2 Å in thickness and ± 0.002 in index. Depositions on both InP and Si substrates have been found to give consistent values within the measurement scatter. For this reason film properties have been measured on Si witness samples.

3.4 Fourier Transform Infrared Spectroscopy

When molecules or crystal lattices absorb IR radiation they are excited into a higher vibrational level. By measuring the IR absorption spectrum of a sample, one obtains a fingerprint whereby the type and density of various chemical bonds are identified. The spectra of SiO_xN_y films yield information about Si–O, Si–N, O–H, N–H, and Si–H bonds in the film. The wavenumber range of 4000–400 cm^{-1} (2.5–25 μm) corresponds to the mid-IR region, commonly used to study these features.

The technique is essentially that of a transmission measurement. An interferometer is used in the measurement of the IR signal; a Fourier transform is used to convert the interferogram into a spectrum. The spectrum of the IR source is first recorded after the IR passes through a blank substrate at normal incidence. This is called the "reference" spectrum. Second, the spectrum of the IR source is recorded after passing though a substrate coated with the film to be measured. This is called the "sample" spectrum. The absorption

Bond	Mode	Position cm^{-1}	Reference
Si–O	rocking	450	[43]
Si–O	bend	800	[43]
Si–N–Si	stretch	850	[44]
Si–O–Si	stretch	1070	[44]
Si–O–Si	out of phase	1200	[44]
$N–H_2$	scissor	1550	[45]
		1545	[46]
Si–H	stretch	2160	[47, 45]
		2260	[43]
N–H	stretch	3340	[45]
		3350	[47]
		3320	[46]
$N–H_2$	stretch	3470	[46]
O–H	stretch	3645	[47]

Table 3.1: Position and identification of FTIR absorption lines in oxynitride films.

spectrum of the film is isolated and calculated from these two measured spectra using:

$$\alpha\ (\text{dB/cm}) = 10 \log_{10}\left[\frac{\text{reference}}{\text{sample}}\right] / \text{ film thickness} \tag{3.1}$$

A Bio-Rad FTS-40 spectrometer is used to measure the IR spectra. Double-polished undoped Si substrates, 300 μm thick, are used to minimize the amount of attenuation that the substrate introduces. The instrument is thoroughly purged with dry N_2 to eliminate artifacts from atmospheric H_2O and CO_2 which otherwise obscure useful spectral features. The spectrum of the IR source has a much larger dynamic range than that of the signal. Hence, when the spectra are divided point by point in Equation 3.1 errors are incurred if the wavenumber positions do not *exactly* correspond. This imprecision in the referencing process causes a drift in the calculated baseline (what corresponds to the true zero absorption) of the absorption spectra, which must be corrected in order obtain accurate information. Fortunately, the baseline drift is significantly smaller in magnitude than the signal and nearly linear in wavenumber. Since the spectra of PECVD films are relatively uncluttered, baseline correction is straightforward and accurate. Figure 3.6 shows sample FTIR spectra of PECVD SiO_2 and SiO_xN_y films with corrected baselines. Table 3.1 lists the positions of notable features in this spectral range.

Bond	Calibration Factor K_{X-H}, cm^{-1}	Reference
N–H	1.9×10^{17}	[47]
Si–H	1.35×10^{17}	[47]
O–H	2.8×10^{17}	[48]
$N–H_2$	4×10^{17}	[48]

Table 3.2: Calibration factors used to determine H content in SiO_xN_y films.

The exact position of features varies with film deposition conditions. This is because both film composition and bonding environment are influenced by deposition conditions. For example, the stretching mode bond energy of X–H depends on what other atoms are back-bonded to X. As the electronegativity of the atoms back-bonded to X decreases, the effective spring constant of the X–H bond decreases and, therefore, the wavenumber of the X–H stretching mode also decreases.

The intense band between 700–1200 cm^{-1} is a superposition of a number of vibrational modes. This feature is mainly related to the Si–O and Si–N bonds in the film and, is therefore, characteristic of the majority of the film. Since the feature positions are not well defined in SiO_xN_y films, it is not possible to accurately deconvolve the individual features. Therefore, it is only appropriate to comment qualitatively on this spectral feature.

The H-related features at 2160 and 3500 cm^{-1} are of greater value since they are correlated with the amount of bonded H in the film and easily separated. From Fig. 3.6 it is seen that only N–H and O–H bonds are present in significant quantities in our films. The hydrogen content of the film is calculated using the method of Lanford and Rand [47]. A calibration factor is used to determine the concentration of X–H bonds from the integrated absorption over the X–H feature:

$$[\text{X-H}] = K_{X-H} \int_{X-H} (\alpha)\, dw \tag{3.2}$$

The total amount of H in the film is then obtained by summing the contributions from O–H, N–H, Si–H, and $N–H_2$ features, assuming that there is no free (unbonded) H in the film. The atomic fraction of H is estimated using the empirical factor of 11.5×10^{-21} At%/cm^3 [47], which is valid up to at least 27 At% H.

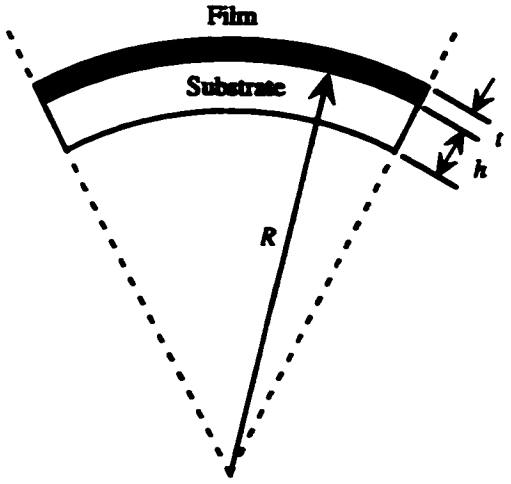

Figure 3.7: Diagram showing film stress conventions. The film is under compression, since without the film the substrate would prefer to lay flat.

3.5 Film Stress

The dielectric films and the InP substrates have different thermal expansion coefficients; hence, upon cooling from the deposition temperature of 300 °C to room temperature the film will be under stress, σ. This elastic energy is partially stored in the substrate which causes it to bow, as illustrated in Fig. 3.7. Typically, oxide films have a thermal expansion coefficient which is an order of magnitude lower than that of InP (see Table 5.2 on page 83). Therefore, oxide films at room temperature are expected to be under compressive stress ($\sigma < 0$); at the high temperatures associated with the QWI process the films are expected to be under tensile stress ($\sigma > 0$).

Substrates exhibit a built in internal stress which must be corrected for in order to obtain an accurate measurement of σ. The change in measured curvature R between the bare substrate, R_1, and the substrate with film, R_2, is:

$$\frac{1}{R} = \frac{1}{R_2} - \frac{1}{R_1} \tag{3.3}$$

The strain is then calculated using R [49]:

$$\sigma = \frac{Eh^2}{(1-\nu)6Rt} \tag{3.4}$$

Where E is the elastic modulus of the (100) InP substrate (74 GPa), ν is Poisson's Ratio

(0.357) [50], h and t are the thickness of substrate and film.

The curvature of the substrate was measured using a scanning laser in a Tencor FLX-2900 system. Substrates were first heated to 300 °C for 30 minutes to allow the internal stress in the substrates an opportunity to relax. The substrates were then cleaned and PECVD films deposited. The as-deposited strain was measured at room temperature.

3.6 Fabry-Perot Waveguide Characterization

The purpose of Fabry-Perot transmission measurements is to determine the absorption and refractive index of waveguides as a function of wavelength. The experimental technique consists of measuring the transmission as a function of wavelength for individual waveguide samples. By modeling the waveguide as a Fabry-Perot etalon the absorption and group index, both as a function of wavelength, are extracted from the transmission spectrum knowing the waveguide length and facet reflectivity. A Tunics model 1500 tunable laser was used as the light source for the experiment: this was coupled to a polarization-preserving lensed fibre which launched a TE polarized probe beam into the waveguides. The output of the waveguide was collected by another lensed fibre connected to a detector. The tunable laser was swept from 1470–1580 nm, and a step size of 0.2 Å was selected to resolve the Fabry-Perot fringes. This was adequate considering that the longitudinal mode spacing of $L = 1000\,\mu$m guides is $\Delta\lambda \approx 3.2$ Å. A fibre-based power splitter was used to sample the tunable laser output power and correct for power fluctuations over the wavelength range. The absorption and group index are calculated from the peak to valley ratio T_{min}/T_{max} and spacing of the measured Fabry-Perot fringes [51]:

$$M = \frac{T_{min}}{T_{max}} = \left[\frac{1 - Re^{-\alpha L}}{1 + Re^{-\alpha L}}\right]^2 \tag{3.5}$$

therefore

$$\alpha = \frac{1}{L}\ln\left[\frac{(1 - \sqrt{M})}{R(1 + \sqrt{M})}\right] \tag{3.6}$$

and

$$n = \frac{\lambda_0}{2L\Delta\lambda} \tag{3.7}$$

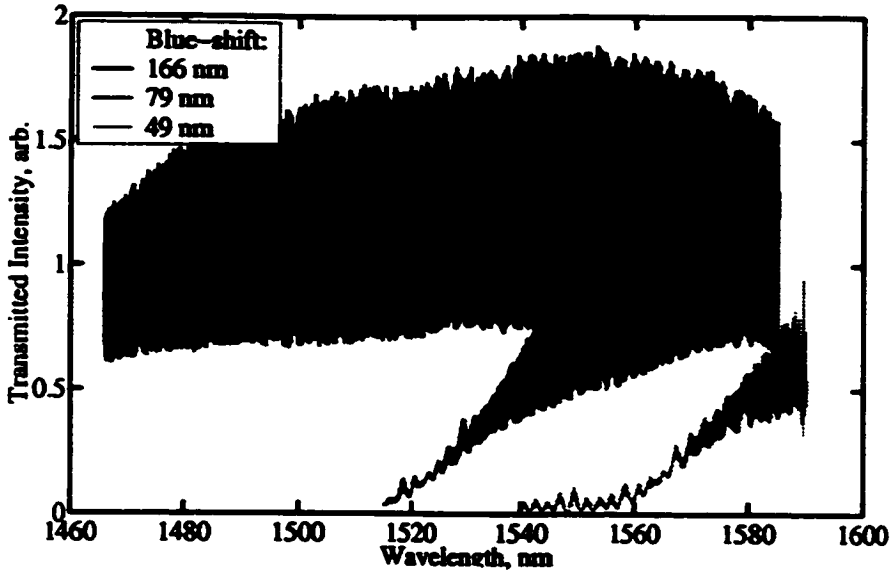

Figure 3.8: Fabry-Perot data for waveguides fabricated from intermixed laser structures. The scale does not permit the observation of individual fringes.

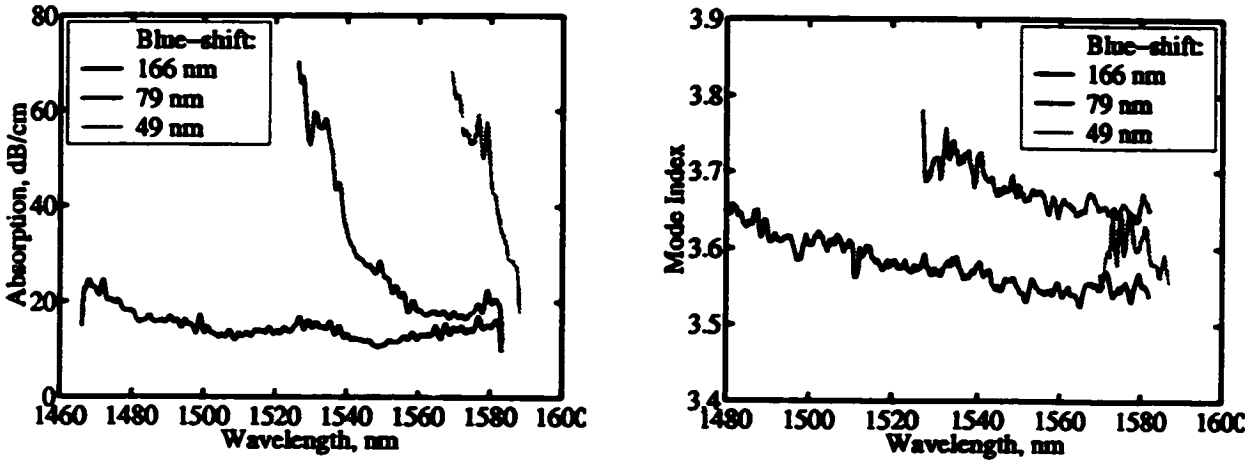

Figure 3.9: Calculations of absorption and group index versus wavelength from the Fabry-Perot data of Fig. 3.8.

A facet reflectivity of $R = 0.32$ is used in the calculations. A sample of raw data is shown in Fig. 3.8, the corresponding calculations of absorption and mode index are shown in Fig. 3.9.

This technique requires that the waveguides have only one waveguide mode, and even so is sensitive to the launch conditions of the probe beam. Single-mode operation of the waveguides can be established by examining the light distribution which exits the waveguide as the probe beam is scanned across the input facet. If the field distribution at

the exit facet remains centered on the facet and changes only in intensity then the waveguide is assumed to be single mode. If the field distribution changes either position or shape significantly then the waveguide is assumed to be multi-mode (since the behavior can be explained by the superposition of the fundamental mode with higher order modes). The data presented in Fig. 3.9 do not show perfect single-mode behavior, which may be evidence of either the second order mode which is close to cutoff, or of higher order modes which have not sufficiently attenuated before reaching the exit facet. The undulations of the absorption spectra (i.e. around 1550 nm) are due to a beating effect from an insufficiently attenuated higher order mode. Longer guides ($> 2000\,\mu$m) would be desireable to reduce this effect further.

Chapter 4

Comparison of Laser Structures for QWI

Introduction

This chapter discusses the stability of laser structures (Section 2.1), subjected to high temperature anneal treatments, both bare and SiO_2-coated. PECVD dielectric films other than SiO_2 are considered in Chapter 5. Section 4.1 presents the QWI results on an annealed uncoated partial laser structure; Sec. 4.2 presents the PECVD SiO_2-capped and annealed results for the same structure. The subsequent sections compare the QWI differences between full and partial laser structures, partially etched structures, ternary versus quaternary wells, and structures grown on n- versus p-doped substrates. Detailed discussions are saved until Sections 4.6 and 4.7 which discuss the thermal and SiO_2-capped results, respectively. Curve fits are added to many figures throughout the following chapters as an aid to the eye and to highlight experimental observations only. The addition of uncertainties to the data would in many cases simply obscure the markers.

4.1 QWI of an Uncoated Partial Laser Structure

Figure 4.1 shows RTPL spectra for sample MBE#2958 (see Table 2.1) annealed for 60 s at various temperatures between 600–800 °C, without an SiO_2 cap layer. As the annealing temperature increases, the peak of the PL spectra moves to shorter wavelengths and the peak intensity passes through a maximum. The difference in peak wavelength before

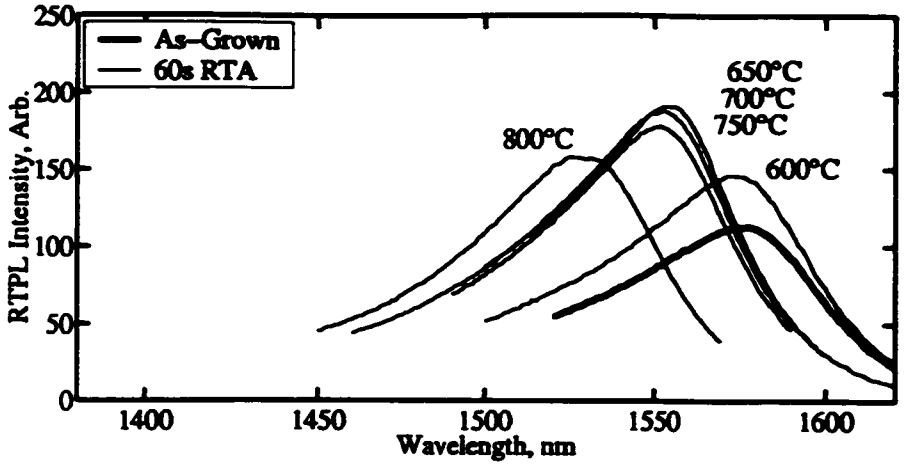

Figure 4.1: Sets of RTPL spectra for a partial laser structure annealed for 60 s at temperatures from 600 to 800 °C in 50 °C increments.

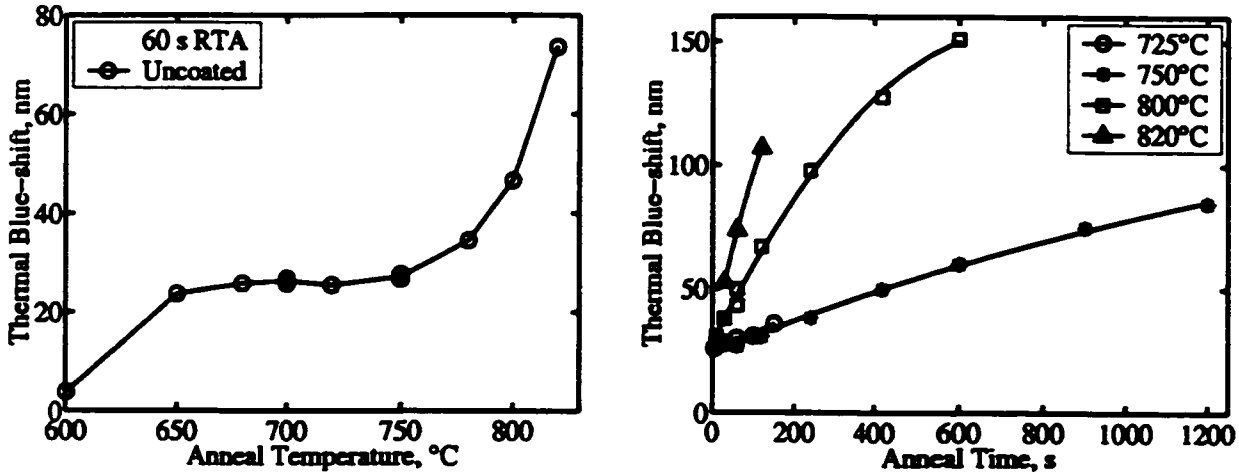

Figure 4.2: Blue-shifting of an uncoated partial laser structure annealed (a) for temperatures between 600–820 °C for 60 s, (b) versus time for various temperatures.

and after heat-treatment is referred to as the wavelength blue-shift. In uncoated samples this is denoted as the "thermal blue-shift". Figure 4.2a illustrates the results of the amount of blue-shift versus RTA temperature for anneal times of 60 s. Figure 4.2b shows the amount of blue-shift versus anneal time at various anneal temperatures. At 600 °C there is very little thermal shift; at most a few nm. Between 600-650 a thermal shift appears, and this saturates around a value of $\approx$ 28 nm in the temperature range of 650–750 °C. At temperatures above 750 °C the amount of thermal shift begins to rise strongly with temperature. In the plateau region, the majority of the 28 nm shift is established on a short time scale of < 5 s, and

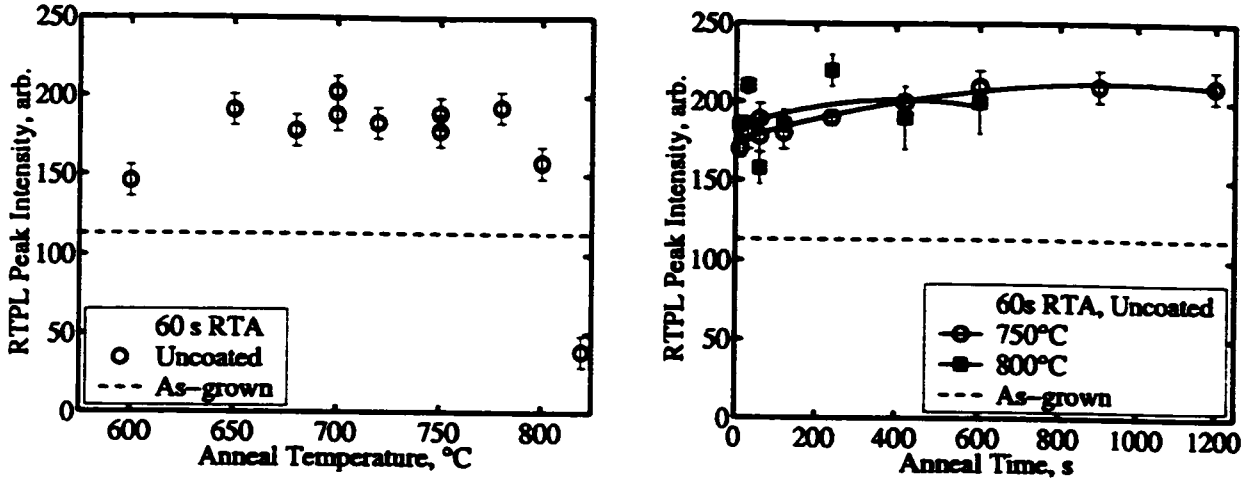

Figure 4.3: RTPL intensity data versus time or temperature of anneal for uncoated samples. The horizontal line denotes the intensity of the as-grown sample.

then the intermixing proceeds slowly after that. As the anneal time is extended at anneal temperatures of 725–750 °C the sample continues to blue-shift more slowly. Above 750 °C, where the blue-shift exceeds that of the plateau region and begins to increase rapidly with temperature, the change with anneal time also increases rapidly with temperature. It is interesting to note that the curves all extrapolate back to essentially the value of 27 ± 2 nm, the measured thermal shift in the plateau region. These observations suggest there is more than one mechanism influencing the thermal behavior. At temperatures of 800 °C we begin to see surface decomposition on the samples after the RTA regardless of the composition of proximity cap used (Si, InP, GaAs), indicating that proximity caps are not effective at these temperatures. After treatments in excess of 820 °C for 60 s the samples become fused to the proximity caps. We note that our results are similar in magnitude to those reported by Harmoudi of an 83 ± 5 nm blue-shift [30] and 92 ± 15 nm [33] blue-shifts at 850 °C 60 s anneal, for QWs that are similar to our standard, but in InGaAsP barriers of an unidentified composition.

As seen in both Figs. 4.1 and Fig. 4.3 the RTPL peak intensity increases from that of the as-grown material, for most anneal treatments. The horizontal line in Fig. 4.3 denotes the intensity of the as-grown sample for comparison. This increase is desirable for both light-emitting and transmitting devices. The improvement is probably due to a removal of

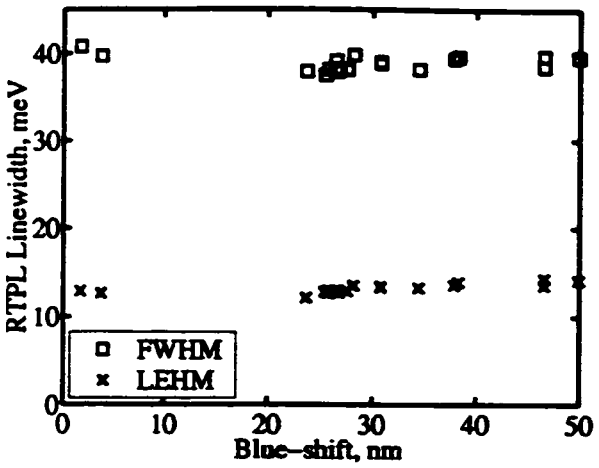

Figure 4.4: RTPL linewidth versus the amount of band-gap shift for uncoated samples annealed for various times and temperatures up to 800 °C.

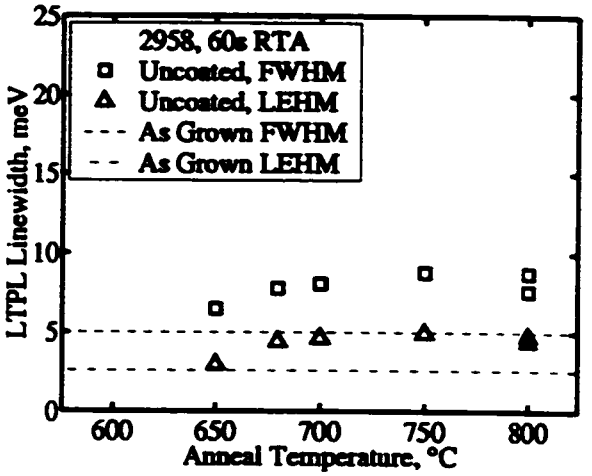

Figure 4.5: LTPL linewidth versus anneal temperature for uncoated samples annealed for 60 s versus temperature.

non-radiative defects initially grown into the active region. The anomalous results seen in the 800 and 820 °C data is likely due to either surface damage and/or incomplete etching of the top layers.

The RTPL full width at half-maximum (FWHM) is shown in Fig. 4.4, and changes little with the amount of thermal QWI. As can be seen directly in Fig. 4.1, most of this occurs on the high-energy side of the spectrum. In LTPL measurements (15 K, $kT = 1.2\,\text{meV}$) strongly intermixed samples do not have asymmetric PL line-shapes. This confirms that thermal population effects are responsible for the RTPL linewidth behavior. The fact that the LTPL linewidth increases with anneal temperature (and, therefore, blue-shift) indicates that the QW has roughened, as will be discussed further in Sec. 4.6.

We believe that the plateau is caused by defects or interfaces grown into the active region, as will be discussed in Sec. 4.6. Since samples do not appear to intermix until the anneal temperature exceeds 600 °C, this suggests that the activation temperature for this process is between 600–650 °C, and once activated the effect quickly runs to completion. The increased sensitivity of the thermal shift with time at higher temperature is believed to be a consequence of the lowered thermal stability of the InGaAsP/InP system and intrinsic interdiffusion taking over at the higher temperatures.

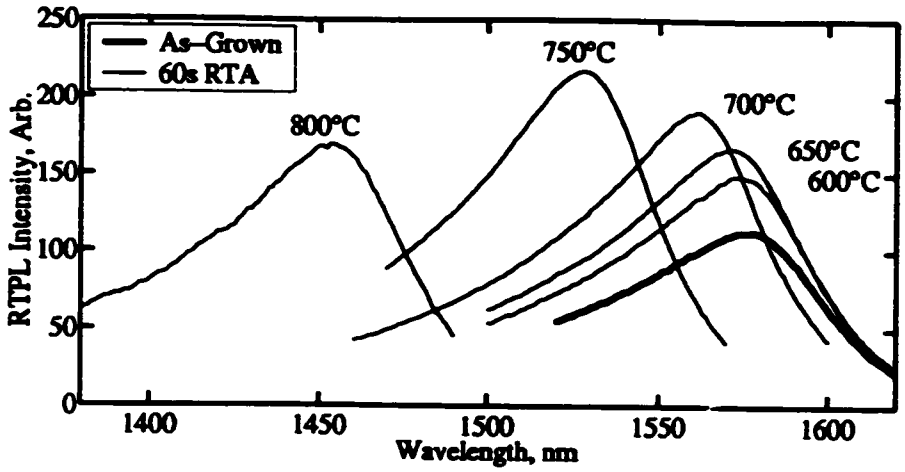

Figure 4.6: RTPL spectra for partial laser structure MBE# 2958 annealed for 60 s at temperatures from 600 to 800 °C.

4.2 QWI of an SiO_2-Capped Partial Laser Structure

Figure 4.6 shows RTPL spectra for sample MBE# 2958 (see Table 2.1) annealed for 60 s at temperatures from 600 to 800 °C, with an SiO_2 cap layer. The difference in peak wavelength before and after heat-treatment in dielectric-coated samples is referred to as the total blue-shift. The "net blue-shift" denotes the dielectric-enhanced blue-shift with the thermal component subtracted.

Figure 4.7 compares the amount of thermal blue-shift and the total oxide-enhanced blue-shift together on the same axis. The difference between these two curves, the net shift, is shown in Fig. 4.8 for a range of conditions. The plateau effect seems to be suppressed in the SiO_2-coated sample. The oxide film causes band-gap shifts in excess of the thermal shift, but not until the anneal temperature exceeds 720 °C as shown in Fig. 4.8a. Figure 4.8b shows the net oxide shift versus anneal time at 750 and 800 °C, demonstrating that the oxide film is able to produce shifts in excess of 70 nm, an amount useful for optical integration purposes. The amount of net shift appears to saturate or roll-over in the neighborhood of 110–120 nm, depending on anneal temperature, Fig. 4.8b. We believe this to be a consequence of the wells and barriers approaching near homogenization. Justification for this is based on calculations which indicate that the samples when fully intermixed should experience a

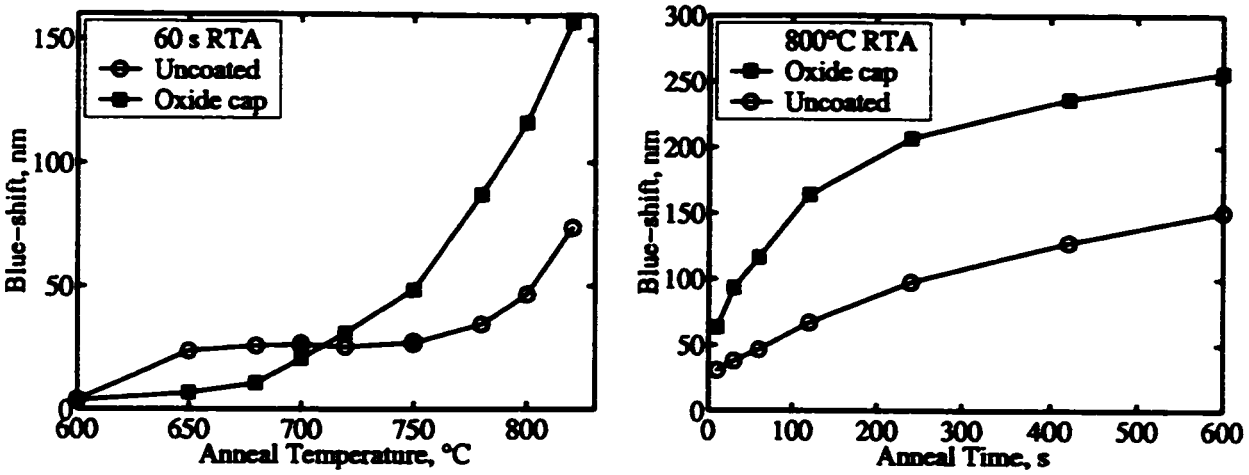

Figure 4.7: Blue-shifting of a partial laser annealed both uncoated and with oxide caps (a) for temperatures between 600–820 °C for 60 s, (b) at 800 °C for times up to 10 minutes.

total shift of ≈250 nm, and we see this saturation behavior in the regime of 200–260 nm. This interpretation is consistent with the fact that the samples annealed at 750 °C exhibit a larger dielectric-enhanced shift than those at 800 °C; the reason being that the uncoated structure shifts less at the lower temperature, leaving more "head-room" before the oxide coated sample reaches the blue-shift "ceiling" around 260 nm. This is also the reason that the 800 °C anneal exhibits a roll-over, since the thermal shift is nearly 150 nm at this anneal treatment. It is surprising though that the 750 °C anneal has not then resulted in much larger enhanced shifts than the 800 °C sample; it may simply require much longer anneal treatments than studied. It is likely that the samples will continue to shift beyond our calculated value since the well material can intermix with ever larger portions of the 1.24 Q GRINSCH layers. The dielectric film appears to suppress the band-gap shift at lower temperatures. As will be seen and discussed in the following sections, this behavior differs from structure to structure, with no clear pattern.

In order to determine if surface oxidation, produced in the RTA furnace, due to the presence of residual atmospheric oxygen, affects the amount of thermal shift, or if it is responsible for the suppression of the thermal shift in the oxide coated samples, a set of samples was annealed with and without a native oxide film. The native oxide film was formed on the surface of the sample during a 10 minute UV ozone treatment. The partial laser

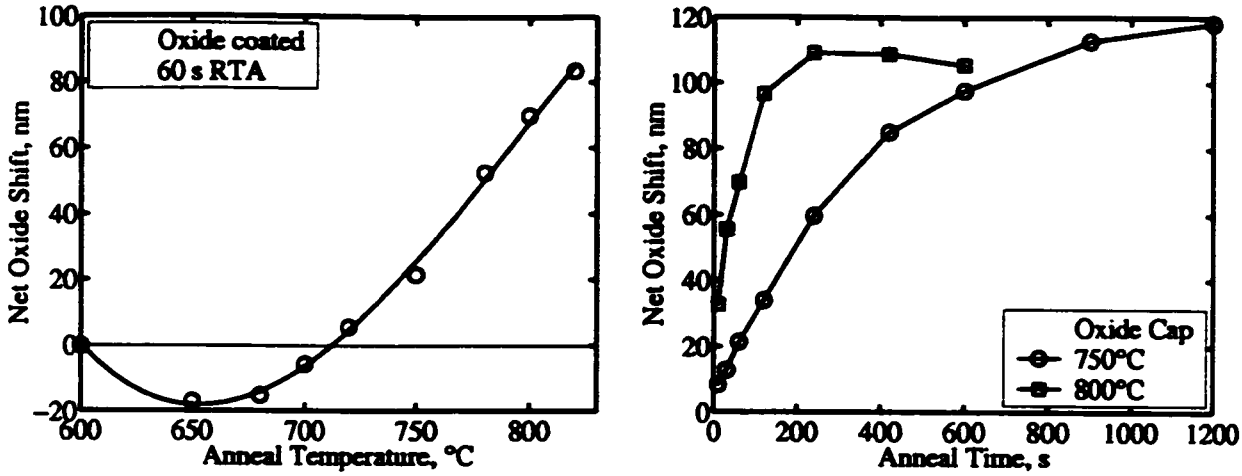

Figure 4.8: Net shift of a partial laser with an oxide cap (a) for temperatures between 600–820 °C for 60 s, (b) at 750 and 800 °C for anneal times up to 20 minutes. The net shift is the oxide-capped shift with the thermal component removed.

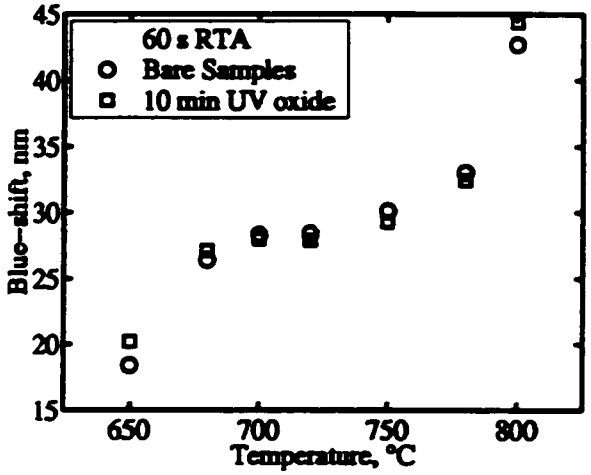

Figure 4.9: Comparison of band-gap-shifting results for bare and UV ozone native oxide capped samples.

structure 2958, discussed in detail in Sections 4.2 and 4.1 was used for this experiment. The film is too thin to measure by ellipsometry or alpha-step; we estimate that it is $\approx 20 \pm 10$ Å thick. As seen in Fig. 4.9 the blue-shifting results both with and without the UV ozone film correspond within ± 1 nm. The UV ozone film therefore has no significant effect on the QWI behavior of the sample. One significant difference between the samples, however, is that at the higher anneal temperatures of 780 and 800 °C the surface of the samples with a UV ozone film markedly degrades, visible to the naked eye. Examination by SEM indicates that the

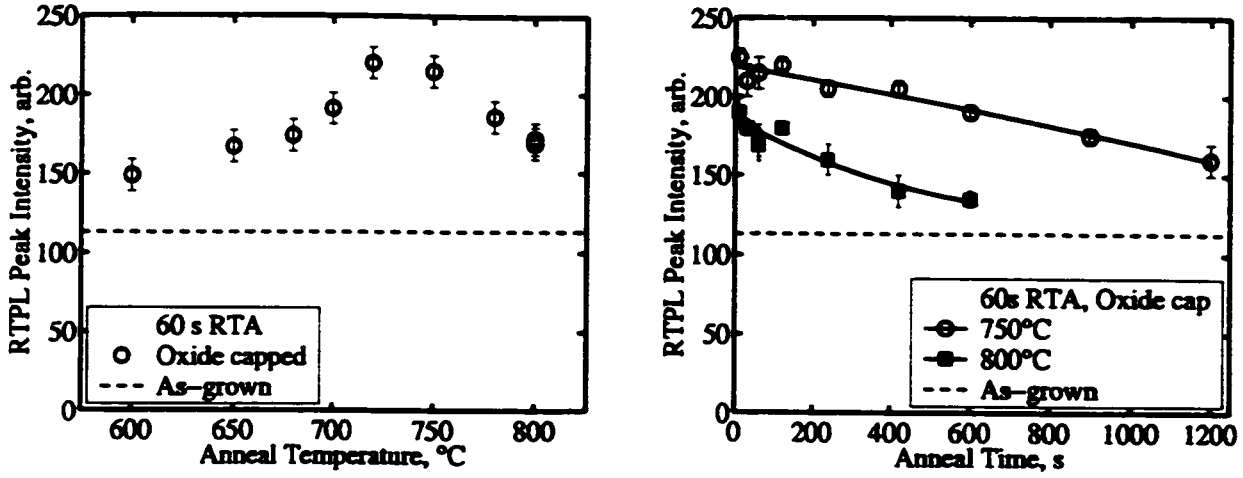

Figure 4.10: RTPL intensity data versus amount time or temperature of anneal. The horizontal line denotes the intensity of the as-grown sample.

surface has roughened, with the appearance of particles $\approx 1\,\mu$m in size, inside very shallow craters. These features are likely In/Ga-rich droplets left after the native oxide desorption and loss of As from the surface. It would seem reasonable to assume that if the surface was involved in the production of defects which affected the QWI process, then the samples which show such marked surface damage would therefore exhibit a different thermal QWI behavior. Since this is not the case, it implies that surface effects are not responsible for the thermal intermixing effect in these samples.

As seen in both Fig. 4.6 and Fig. 4.10 for 60 s anneals at all temperatures the RTPL peak intensity is increased with respect to the as-grown samples. This increase in peak intensity is a maximum for anneal temperatures of $\approx 725\,^{\circ}$C and drops for either anneal temperatures above 750 °C or with increasing anneal time. However, there is still an $\approx 50\,\%$ increase even after 800 °C anneals. The RTPL FWHM steadily and strongly increases with the amount of band-gap shift after an initial sharpening of a few meV, as shown in Fig. 4.11. The initial sharpening may be related to smoothing at the QW/barrier interface, although this may not be consistent with the development of LCM in QWI structures. Most of this linewidth broadening occurs on the high-energy side of the spectrum. We believe that the RTPL linewidth-broadening effect is due to the evolution of the active region from that of a QW to a quasi-continuum as shown in Fig. 2.2 and Fig. 4.12. The distribution of carriers

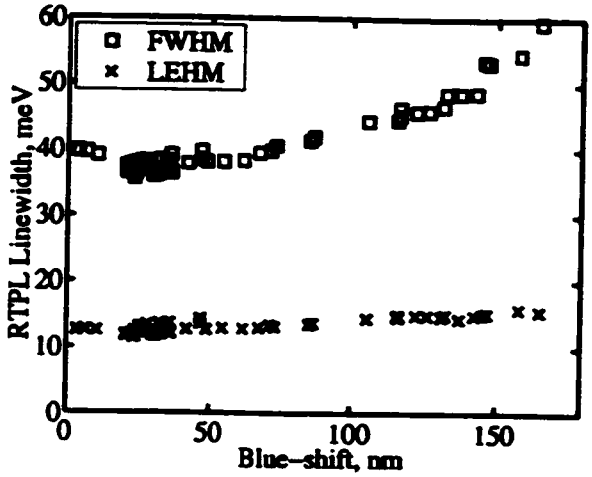

Figure 4.11: RTPL linewidth versus total band-gap shift for samples annealed for 60 s at various temperatures. Uncoated, SiO_2-capped, SiO_xN_y-capped, and SOG-capped samples are all included.

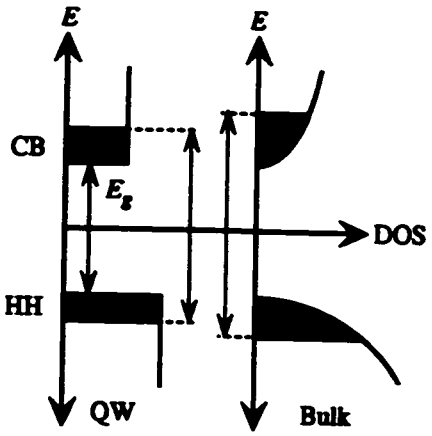

Figure 4.12: Illustration of why the PL linewidth increases due to population effects when the QW broadens and the DOS approximates that of a bulk layer.

over a larger energy range increases the emission at shorter wavelengths and therefore both broadens the RTPL linewidth and decreases the peak intensity. The drop in RTPL peak intensity with blue-shift for the oxide-coated sample is therefore not related to a degradation in material quality.

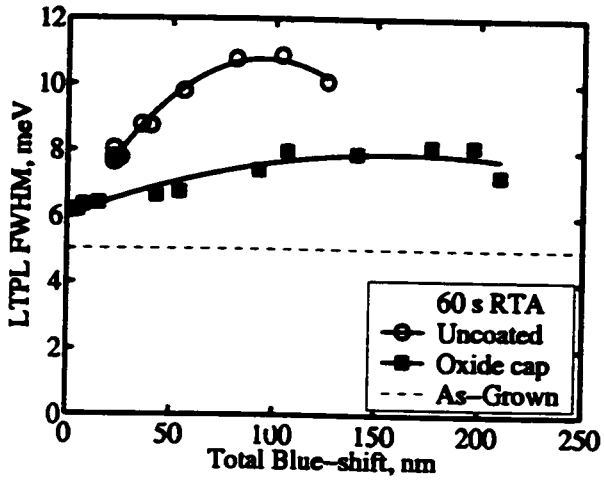

Figure 4.13: LTPL linewidth versus amount of band-gap shift for samples annealed at temperatures up to 800 °C and times up to 60 s, both uncoated and with oxide caps.

Strongly intermixed samples do not have large LTPL linewidths even though the FWHM can increase by a factor of greater than two, Fig. 4.13, again confirming that ther-

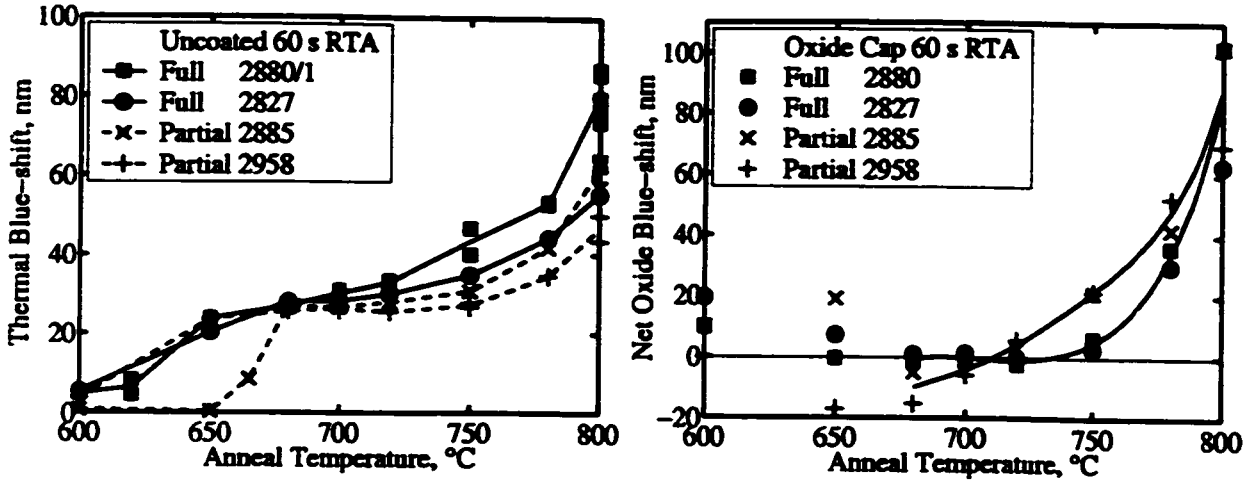

Figure 4.14: Comparison of thermal and net blue-shift for various full and partial structures annealed for 60 s, versus temperature.

mal population effects are responsible for the RTPL linewidth behavior. The decrease in RTPL FWHM (Fig. 4.11) is not observed in LTPL measurements; this may be related to interface roughness; the recombination taking place in the low band-gap regions only in the LTPL measurements. At low temperature, where thermal broadening effects are greatly reduced, it is seen that oxide capped samples exhibit smaller linewidths than uncoated samples annealed in the same furnace treatment; this is also true when comparing samples that have experienced the same blue-shift. This result demonstrates that the oxide cap actually acts to preserve the quality of the sample active region, even at low anneal temperatures where it is inhibiting the thermal shift.

4.3 QWI of Full Versus Partial Structures

Figure 4.14 compares the thermal shift in both partial and full laser structures. The physical differences between the partial and full structures, noted in Table 2.1, is the addition of an etch-stop, a thick InP layer, a 2000 Å as opposed to a 1000 Å InGaAs cap layer. Also, the layers grown above the active region are heavily doped p-type. On average, the QWI results of the full structures show an increased thermal shift and the plateau region appears sloped. The SiO_2-capped results show that the enhanced QWI effect in full structures activates at a temperature 25 ± 5 °C higher than the partial structures. The observed scatter in the results

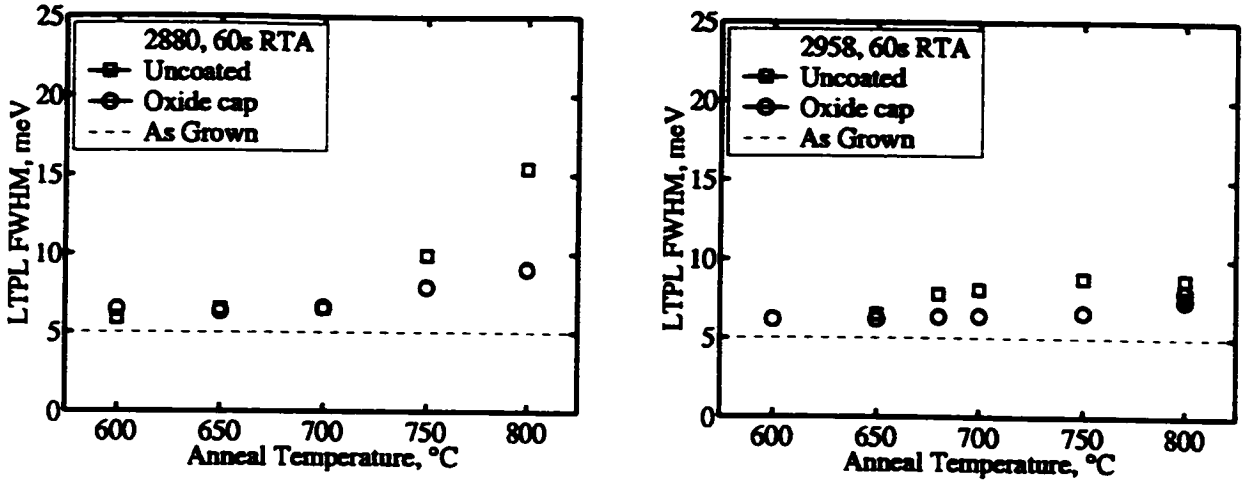

Figure 4.15: LTPL linewidth for full and partial laser structures annealed for 60 s, (a) full laser structure MBE# 2880, (b) partial laser structure MBE# 2958.

for the partial structures for anneal temperatures of 680 °C and below is likely related to the different laser growths, as will be discussed later in this section; we have ruled out the possibility that the results are due to the reproducibility of the annealing process.

A comparison of the LTPL results, Fig. 4.15, reveals that the two structures have similar as-grown linewidths, but that the uncoated full structure exhibits larger linewidths at anneal temperatures of 750 °C and above. The SiO_2-capped samples again exhibit smaller linewidths than uncoated samples, the linewidths being marginally larger in the full structure.

These results suggest that at least one component of the thermal shift originates from defects grown into the extra semiconductor material added to the structure, and that this has a deleterious effect on the QW material quality by virtue of the fact that the LTPL linewidth increases more on anneal in the full laser structures. In order to determine if these grown-in defects could be removed from the material before the RTA treatment a pair of structures was grown: MBE# 2880 and MBE# 2881. These samples are nominally identical full lasers, except for the fact that the growth of 2881 was interrupted 100 Å into the top InGaAs cap layer and was annealed for 8 min at 525 °C in-situ under a Group V over-pressure before depositing the remaining 1900 Å of InGaAs to complete the layer. This is compared to the customary growth temperature of 470 °C. Fig. 4.16 compares the two structures with and without SiO_2 caps, showing that they exhibit the same results, usually

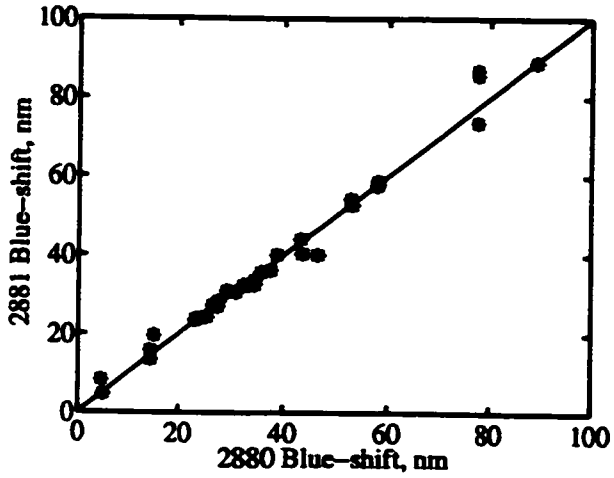

Figure 4.16: Comparison of blue-shift for MBE# 2880 and 2881. MBE# 2881 has a 525 °C in-situ anneal during growth. Results include various temperatures and times for both uncoated and SiO_2-capped samples. The line denotes a 1:1 relationship and is not a curve fit. The results demonstrate the reproducibility of the QWI process.

within uncertainty. Therefore, we conclude that the in-situ anneal has no effect, and that it is possible to reproduce QWI results using sequential growths of the same structure.

From examination of Fig. 4.14 it is seen that additional comparisons of nominally identical laser structures can be made. MBE# 2885 and 2958 are both nominally the same partial laser structure, but grown on separate occasions. However, these two structures exhibited different results, particularly at the lower anneal temperatures. During this time we were able to reproduce previous results versus temperature for MBE# 2826 and have, therefore, ruled out the operation of the RTA furnace as the cause of the differences. While the different SiO_2 results could be attributed to variations in PECVD chamber cleanliness or drift, we do not believe that this is the case, since successive depositions produce consistent results (excepting the circumstance of a faulty RF power supply discussed in Sec. 5.2); it seems reasonable to expect that the samples will not behave the same when dielectric coated when the behavior of the uncoated structure differs to begin with. Structures MBE# 2880 and 2827 are similar in that they are both full laser growths on n-type substrates, but they differ in various aspects as outlined in Table 2.1. The LTPL linewidths show similar trends, but MBE# 2827 has linewidths that are ≈ 2 meV larger than those of MBE# 2880

(not shown). The difference in layer structure may be a possible contributing factor to the differing results; unfortunately, there are too many structural differences to make a clear identification. The differences may be attributed to differences in either grown-in defects, substrate defects, or GSMBE growth conditions outside of experimental control. This seems reasonable since it has been noted in the literature before for InGaAs/GaAs that substrate defects play a more important role than most growth parameters, such as flux ratios and growth temperature by providing a source of defects which dominate the intermixing process [52]. Additionally, a study of InGaAs/InGaAsP wells on a variety of substrates identified that the substrate etch pit density was the determining factor in the activation energy of the thermal intermixing process [53].

In general, it appears that the growth reproducibility accounts for most of the non-reproducibility in the QWI behavior, particularly when the period between growths is long. Practical application in a production environment should lead to better reproducibility as compared to a research system, where many different compounds and structures are grown between laser structures intended for intermixing studies. For sequential growths, reproducibility is most sensitive to higher anneal temperatures, likely due to the greater sensitivity of the QWI to both anneal temperature and time in this vicinity. Practical device processing is therefore more reliable if lower anneal temperatures, around 750 °C, are used when intermixing the samples.

To determine what effect the layers above the active region have on the thermal QWI process, the top-most 1–2 layers were etched from both full and partial structures, and the samples subsequently annealed as a function of temperature. The results are presented in Fig. 4.17. In the partial structure, after the 1000 Å InGaAs and 250 Å InP layers (both undoped) are removed the top 1.15 Q GRINSCH layer is exposed. In the full structure the removal of the 2000 Å p-InGaAs and 1.0 μm p-InP layers exposes the thin 1.3 Q etch-stop layer. Comparisons of the results from these two structures are complicated by the fact that both the sample geometries and doping levels differ.

The blue-shift versus anneal temperature for these etched samples can be separated

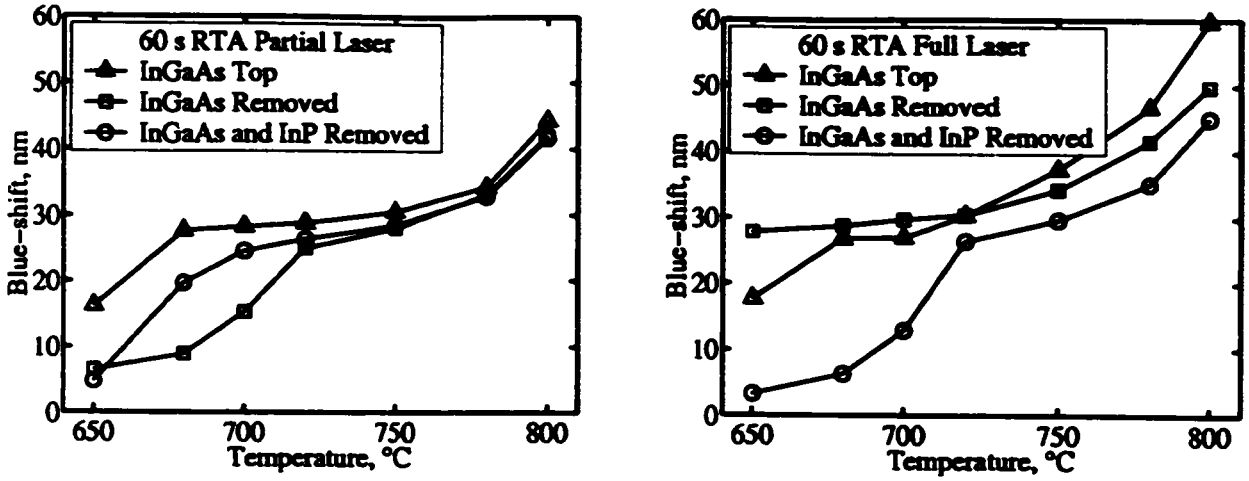

Figure 4.17: Blue-shifting of an uncoated laser structure annealed for 60 s with various layers removed from the top surface, (a) Partial laser structure 2885 (b) Full laser structure 2880. See Table 2.1 for specific structure details.

into two regimes. Above $\approx$ 730 °C the QWI steadily increases with temperature and the amount of material present over top of the active region. A simple explanation, which seems plausible is that the defects present in the upper layers of material are mobile enough to diffuse to the active region and promote disordering. As the amount of material is reduced, either by the growth of less material or by etch removal the top layers, the blue-shift decreases due to the lesser number of defects present to drive the QWI process.

Below 730 °C the differences in the QWI behavior are much greater. Depending on whether the sample is a full or partial laser structure, the removal of the top InGaAs layer can either decrease or increase the amount of blue-shift. There are too many differences between the samples to determine if this is due to the different doping levels of the upper layers. It appears that for different geometries the plateau activates at different temperatures; we do not know what causes this behavior, or if this effect is related to the variable results that we obtain from comparing nominally identical structures. We speculate that the grown-defects present in the upper layers are as mobile at these lower anneal temperatures. Consequently, their movement may be influenced by the electric fields in the sample. As layers are etched off the surface, the band-bending near the surface will change depending on the material composition and doping level. The electric fields within the structure will therefore change,

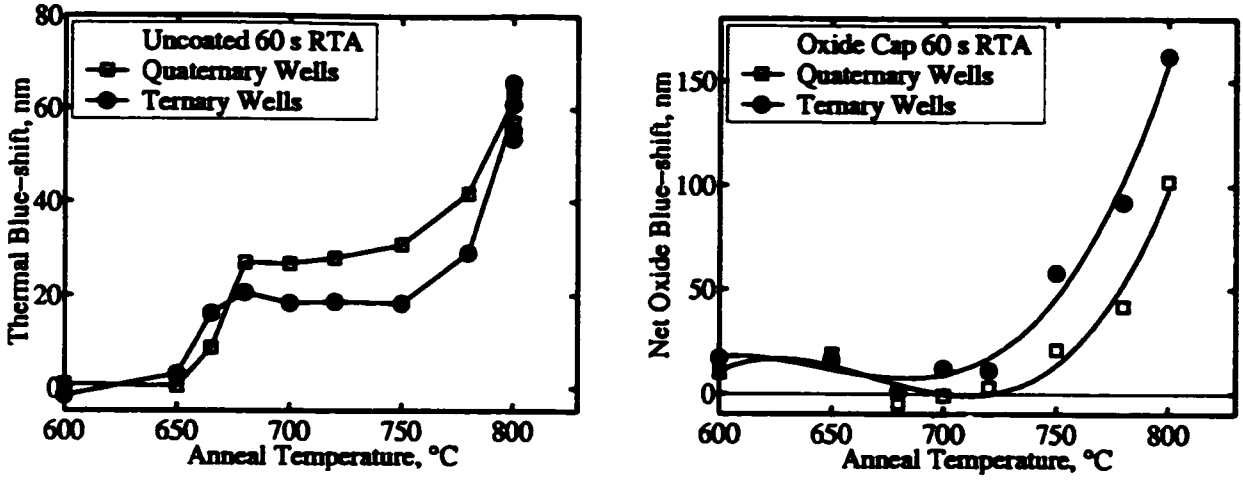

Figure 4.18: Blue-shift for ternary and quaternary QW samples annealed for 60 s, (a) thermal blue-shift, (b) net oxide capped blue-shift.

potentially affecting the migration behavior of defects and the thermal QWI process. Since the two samples considered have different doping levels and layer thicknesses we are unable to suggest a more complete model.

4.4 QWI of Quaternary Versus Ternary QWs

The ternary and quaternary wells show significantly different behavior, as illustrated in Fig. 4.18. Both show an increase in thermal blue-shift above 650 °C and a plateau region between 680–750 °C. The InGaAs wells exhibit a lower thermal plateau level. For anneals at 800 °C thermal shift appears to become comparable to that of InGaAsP wells, but the rapid rate of change of blue-shift with temperature leads to a large spread in the data. The effect of SiO_2 caps is to produce blue-shifts of larger magnitude in the InGaAs QW samples, the dielectric-enhanced effect being evident at temperatures 20 °C lower than in InGaAsP samples. We believe that the differences in results are related to the compositional differences between two QW types because the Group III ratios are not the same in the InGaAs QWs and barriers. This will be discussed in Sec. 4.6.

The InGaAs QW LTPL linewidths, Fig. 4.19, exhibit similar behavior to InGaAsP QWs versus anneal temperature, however, the InGaAs wells show broader linewidths than the quaternary structures (see Fig. 4.15 on page 47). This is likely related to either the non-

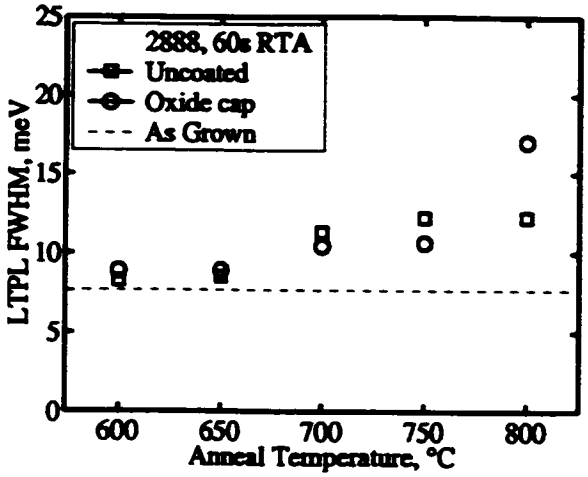

Figure 4.19: LTPL linewidths for ternary QW samples annealed for 60 s.

optimum growth temperature of the InGaAs (470 °C), or grown-in LCM, since the InGaAs QWs are more likely to suffer LCM than the InGaAsP QWs, as shown in Fig. 2.3; additionally, the composition of an intermixed InGaAs QW will likely lie deeper within the isotherm than for an InGaAsP QW.

Studies of InGaAs/InGaAsP wells have been presented in the literature before, and it was shown that there was little intermixing effect at 700 °C [21]. Results published for 30 s anneal cycles at temperatures between 600–800 °C for lattice-matched InGaAs wells in InGaAsP barriers (of nearly the same composition as we have studied) exhibited thermal results that are smaller than ours by 5–10 nm [54]. The same study also examined the effect of PECVD SiO_2 films, the results being significantly lower in magnitude at anneal temperatures above 700 °C.

4.5 QWI of Structures Grown on p- and n-Substrates

Sequentially grown samples with complementary doping profiles show a significant difference in QWI behavior, as shown in Fig. 4.20. The n-substrate-based structure, MBE# 2827, behaves similarly to the full and partial structures, also grown on n-substrates, as already described. The p-substrate-based structure, MBE# 2826, exhibits an all-together different temperature dependence with no plateau region, blue-shift onset at 650 °C, and ultimately

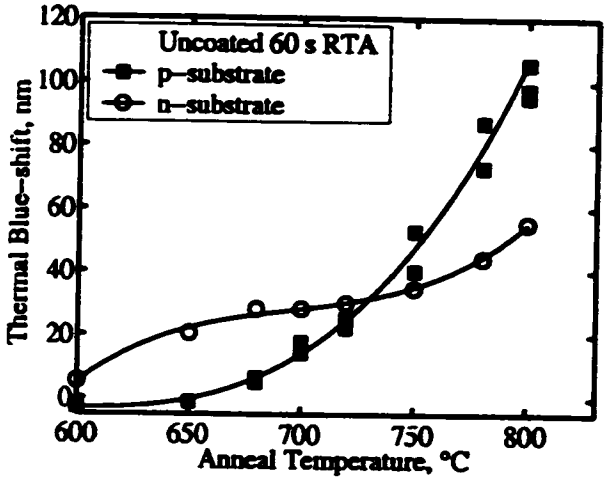

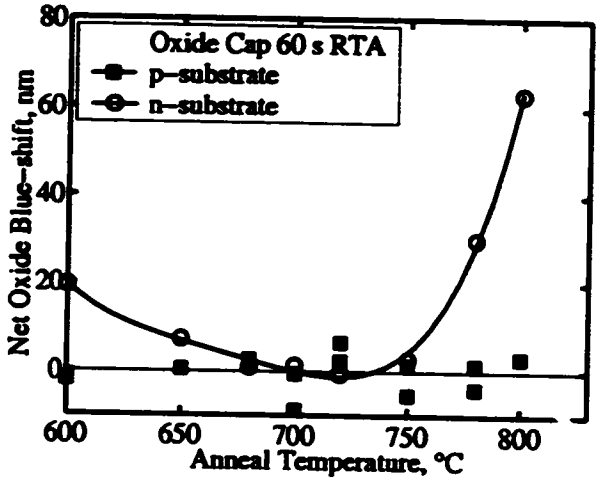

Figure 4.20: Blue-shift for n- and p-substrate-based samples annealed for 60 s at various temperatures, (a) thermal blue-shift, (b) net oxide-coated blue-shift.

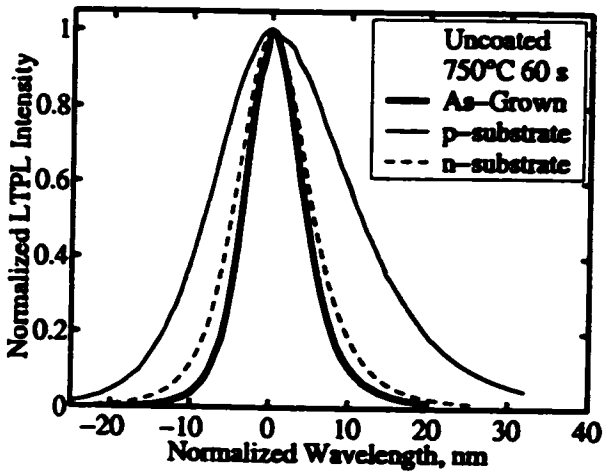

Figure 4.21: LTPL spectra for uncoated p- and n-substrate-based samples. The spectra have been normalized to the peak intensity and shifted in wavelength so that the peak positions correspond. The as-grown spectra are very similar; the effect of annealing is to broaden the p-substrate FWHM and introduce band-tailing.

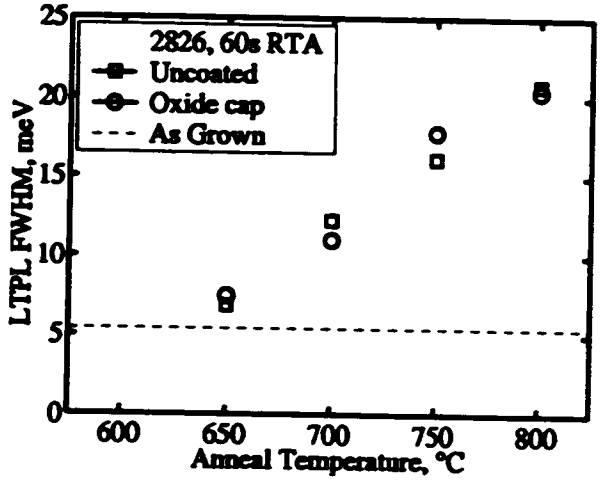

Figure 4.22: LTPL FWHM for p-substrate-based samples annealed for 60 s. For comparison with n-substrate-based samples see Fig. 4.15, for example.

exhibits much larger thermal shifts at anneal temperatures above 750 °C. It is interesting that the dielectric does not appear to enhance the intermixing process over this temperature range for 60 s anneals in the p-substrate-based structure.

The LTPL spectra shed additional light on the difference in behavior between these two structures, illustrated in Figs. 4.21 and 4.22. Overall the p-substrate structure shows

much larger linewidths at much lower anneal temperatures. There is strong band-tailing and much broader LTPL linewidths in the p-substrate samples compared to the n-substrate samples, as illustrated for 750 °C in Fig. 4.21. There is no significant difference in linewidths between the SiO_2-capped and bare samples, shown in Fig. 4.22, suggesting that the process by which the SiO_2 cap suppresses the broadening in the n-substrate samples is either not present, or is overcome by the mechanism causing the large linewidth and blue-shift.

The gradually rising thermal shift of the p-substrate structure, absence of a plateau region, and absence of a dielectric-enhanced shift suggests that QWI processes present in this structure are different from those already discussed, and related to sample doping. Disordering experiments using a Zn drive-in diffusion typically result in a red-shift due to the preferential intermixing of Group III atoms at temperatures below 600 °C [55]. There is also evidence that Zn can promote intermixing of the Group V sub-lattice at 700 °C [56]. It therefore seems reasonable that the QWI in these structures grown on Zn-doped substrates is related to either the migration of substrate defects made possible by the different electric fields in the sample, or related to the movement of the Zn atoms. Regardless, the intermixing processes in the p-substrate samples appears to be much more aggressive and damaging than the processes present in the n-substrate sample, with or without a SiO_2 cap.

4.6 Discussion of Thermal QWI

There appear to be two effects contributing to the thermal intermixing effect. The initial effect occurs at ≈ 650 °C and quickly runs to completion producing a 28 ± 2 nm shift, and is followed by a region of no change in blue-shift between anneal temperatures of 650–750 °C. The second effect, above 750 °C, is responsible for causing a shift which is time and temperature dependent. Care should be taken that native oxide films are not present on the sample surface and that anneal temperatures do not exceed 820 °C, in order to avoid surface damage problems.

We believe that the plateau is caused by defects grown into the active region. We speculate that the proximity of the defects allows the process to occur quickly and then

exhaust itself since the defects either diffuse away or are consumed in the process. Samples do not appear to thermally intermix until the anneal temperature exceeds 600 °C, the exact temperature depending on sample structure. In order to investigate the nature of the plateau, and how it was influenced by the presence of semiconductor layers above the active region, experiments were performed where the top 1–2 layers (InGaAs and InP) were etched away before annealing. The results of these experiments showed two distinct regimes. Below 730 °C the sample geometry and/or doping affected the activation temperature of the plateau. Above 730 °C the thermal shift increased with the amount of material above the active region. Electric fields, produced by surface effects, doping, and heterojunctions may be responsible for the activation temperature varying between $\approx$ 600–700 °C, if they are able to influence the migration behavior of the grown-in defects. The absence of a plateau in the p-doped substrate sample may be evidence that the electric fields affect the migration behavior of the grown-in defects. Once activated the effect quickly runs to completion.

Certainly, LCM is present in the as-grown active region layers [38, 57]. It has been shown before [25] that the LCM is not removed upon anneal, but that phase separated areas become internally more uniform and distinct from each other, as observed in TEM diffraction. While LCM was thought to influence the QWI process in strongly tensile-strained QW structures [25], we do not believe that changes in LCM are responsible for the blue-shift plateau. Evidence that LCM increases with intermixing in our samples is that the LTPL FWHM of annealed samples is greater than that of non-annealed samples; had LCM been removed one would expect a decrease in the FWHM. Additionally, InGaAs QWs exhibit larger linewidths than the InGaAsP QWs after annealing which could be a consequence that the compositions of intermixed InGaAs QWs lie deeper within the spinodal isotherm than intermixed InGaAsP QWs.

In the higher temperature regime, the shift which occurs on a longer time scale appears to be associated with grown-in defects, perhaps from the layers above the active region, as opposed to defects generated at the sample surface during anneal. It has been shown before [34] that a P-deficient atmosphere promotes intermixing, likely due to the loss

of Group V atoms from the surface thereby producing vacancies which diffuse and promote the QWI. Although this seems reasonable, the full structures exhibit more thermal shift, which is consistent with the increased amount of material providing a larger source of grown-in defects which promote disordering, as opposed to the assumption that Group V vacancies produced at the surface cause the intermixing. The etch-back experiments, where samples with different top layers are removed, annealed, and compared suggests that this is the case for temperatures above 750 °C. This interpretation is also consistent with the UV ozone native oxide film experiments, page 42, that show samples with significant surface damage (visible to the naked eye) experience the same amount of QWI. QWI experiments with samples capped with He*-InP material, known to contain Group V vacancies, do not show enhanced intermixing in full laser structures; this suggests that Group V vacancies are slow to diffuse to the active region. Other He*-InP experiments [22] have identified that a portion of the thermal effect and, hence, the increased thermal blue-shift in the full structures comes from the (additional) material grown above the active region. These experiments involve layers of InP grown in the presence of a He plasma (He*-InP). The He*-InP material either promotes or suppresses QWI, depending on its proximity to the active region. By placing layers at different distances above and below the active region, it was determined that defects in the substrate did not contribute to the thermal shift, but that there was a source of defects in the layers above the active region that contributed to produce roughly 30–60 % of the thermal shift. Therefore, it would seem that within the InGaAsP/InP system, thermal intermixing is dominated by grown-in defects. The grown-in defects in the InGaAs cap layer may be related to the relatively low growth temperature of 470 °C, or may be associated with the presence of LCM. QWI enhancing defects may also be related to interfaces or dopants; we are unable to make a clear identification with the present data.

The intermixing of Group V species (As, P) acts to produce a wider well with a higher band-gap. The intermixing of Group III species (In, Ga) acts to produce a wider well with a smaller band-gap. Therefore, one expects Group III intermixing to produce a red-shift in wavelength, and Group V intermixing to produce a blue-shift in wavelength,

assuming that the compositional changes outweigh those due to well width. Calculations have shown that this is the case [33]. It therefore makes sense that the InGaAs wells exhibit less thermal blue-shift due to the competition of both Group III and V intermixing, where in the InGaAsP QWs the Group III compositions are nominally identical in both the QWs and barriers.

LTPL results suggest that the grown-in defects from the top layers promote an intermixing process that degrades the QWs, as evidenced by the increased LTPL linewidths. The larger linewidths may be due to LCM effects causing the QWs to become more non-uniform. Variations in either the QW composition or thickness would cause changes in QW energy over the surface of the sample. When averaged, this would appear as a broader PL spectrum. An inspection of the individual spectra shows that the amount of band-tailing is small, which supports the fact that the spectra are being broadened by inhomogeneous effects and not by the presence of defects accumulating within the active region.

The intensity improvement for 600 °C anneal treatments indicates that non-radiative defects are removed from the material, since the lack of a blue-shift means the QWs are unchanged. There is no evidence from PL-intensity measurements that the thermal intermixing process leaves the material loaded with any significant concentration of defect-related localized states acting as non-radiative recombination centers which would result in a reduction in luminescence intensity.

We believe that the thermal intermixing mechanism in the Zn-doped p-substrate samples is different than in the n-substrate-based structures. Since the electric fields in the structure are reversed it is possible that charged substrate defects, other than Zn, are able to migrate to the active region and enhance the thermal QWI process. Zinc is also known for its high diffusivity and QWI effect, where it enhances the Group III sub-lattice QWI at low temperatures [55], and may induce disordering on the Group V sublattice at 700 °C [56]. Therefore, the Zn itself may be diffusing from the substrate and enhancing the QWI at higher anneal temperatures. We are unable to distinguish which effect is responsible; SIMS measurements of the Zn profile would be useful in this respect.

4.7 Discussion of SiO_2-capped QWI

The QWI behavior when the samples are capped with SiO_2 films depends on both device structure and anneal treatment. At temperatures in excess of 730 °C the film acts to enhance the QWI process. At temperatures below 730 °C a blue-shift less than that of an uncapped sample is experienced by some dielectric coated samples.

It is not understood if the lack of a blue-shift at low anneal temperatures in some dielectric capped samples is due to the presence of the dielectric film, or if it is related to the laser structure itself, since the results are not consistent when nominally identical partial laser structures with nominally the same dielectric film are compared. If the dielectric film is indeed responsible for the suppression of the blue-shift then the suppression effect is not likely related to the dielectric simply protecting the surface from a loss of Group V species during the anneal since surface effects do not seem to have a significant effect in uncapped samples. Suppression mechanism possibilities include defects introduced by the dielectric interacting with the intrinsic defects, the dielectric affecting the thermal intermixing process through a mechanism like strain, or a surface effect similar to that observed in partially etched structures as described in Sec. 4.3.

Above 730 °C the dielectric-enhanced QWI effect produces blue-shifts that are greater than that of the thermal shift. The net blue-shift increases with both anneal temperature and time, with the amount of intermixing becoming more sensitive as the anneal temperature increases. Because the Group III ratio (Ga/In) between the QWs and barriers is the same we believe that defects injected into the laser structure, as a consequence of the dielectric film's presence, are intermixing the Group V sub-lattice to produce the blue-shift.

The examination of QW composition shows that the InGaAs QWs exhibit a larger dielectric-capped shift, even though they have a lower thermal shift. The lower thermal shift is explained by the simultaneous interdiffusion of both Group III and V species whose effects partially counter each other in producing a blue-shift. Why then would the InGaAs wells have a larger dielectric-enhanced shift if both Group III and V species are available to intermix? This result suggests that the effect of the oxide cap is to preferentially enhance

the intermixing on the Group V sub-lattice. The larger net blue-shift may be due to the fact that the InGaAs wells differ more significantly in Group V composition from the 1.24 Q barriers than do the InGaAsP QWs. Section 5.8 postulates that the dielectric films inject Group V interstitials which cause the enhanced QWI. This mechanism appears consistent with the results on these InGaAs QW structures.

We believe that the RTPL linewidth-broadening effect, Fig. 4.11, is due to the evolution of the active region from that of a QW to a quasi-continuum as shown in Fig. 2.2. In the as-grown sample the two lowest QW radiative transitions are separated by 70 meV ($kT = 24$ meV at RT) and the DOS will be constant over this range. Additional energy levels are introduced into the QW as it broadens, illustrated for the case of heavy intermixing in Fig. 2.2. These levels, spaced ever closer together as intermixing proceeds, will cause the DOS to increase with energy. The thermal distribution of carriers over a larger energy range increases the emission at shorter wavelengths and therefore broadens the RTPL linewidth. The drop in RTPL peak intensity with blue-shift for the oxide-coated sample is a consequence of the thermal distribution of carriers over a large energy range, and not related to a degradation in material quality.

At 15 K, where thermal broadening effects are greatly reduced, it is seen that oxide-capped samples exhibit significantly smaller linewidths and less band-tailing than uncoated samples annealed in the same manner or for the same blue-shift (see Fig. 4.13, for example). Therefore, the oxide cap actually acts to preserve the quality of the sample active region, even at low anneal temperatures where the thermal shift is sometimes inhibited. The fact that the PL peak broadens on the low-energy side without showing significant band-tailing suggests that the QWs are becoming spatially more non-uniform. The non-uniformity would cause different areas of the sample to emit light at different peak wavelengths, thus broadening the PL. In fact, the oxide-capped results are close to that of the theoretical linewidth for QW thickness fluctuations of one monolayer [57]. If the defect introduced by the presence of the dielectric film promotes a more uniform intermixing process, then this could explain why the dielectric-coated samples exhibit lower LTPL linewidths even though neither dielectric-

or un-coated samples show significant band-tailing.

The structures grown on p-substrates do not exhibit a dielectric-enhanced QWI effect. The reason for the absence of an enhanced dielectric blue-shift is not fully understood. The presence of Zn may block the action of the SiO_2-introduced defects if they are charged and unable to surmount electrostatic barriers within the oppositely-doped structure and therefore unable to arrive at the active region.

4.8 Overall Summary

This chapter has described how the blue-shifting results depend on the laser structure used. Partial laser structures with SiO_2 caps can be used advantageously to create differential amounts of blue-shift, but caution must be taken in applying this method. Reproducibility is most sensitive at anneal temperatures starting at 800 °C, likely due to the greater sensitivity of the QWI to both anneal temperature and time in this vicinity. The different behavior of nominally identical structures suggests that the substrate or growth conditions affect the QWI results. This has the implication that the behavior of every growth should be individually characterized before proceeding with device fabrication. Practical application in a production environment should lead to better reproducibility as compared to a research system, where many different compounds and structures are grown between laser growths intended for intermixing studies.

Multiple mechanisms appear to be responsible for the thermal QWI process. There appears to be a fast transient process that causes a ≈ 25 nm shift within seconds of heat treatment above 600 °C. This is postulated to be due to grown-in defects located in the active region. The second process is the intrinsic thermal intermixing that causes the structure to intermix on a longer time scale, and produces large shifts once the anneal temperature exceeds 750 °C. This process is likely related to both grown-in defects removed from the active region and the thermal stability of the InGaAsP material.

The action by which the dielectric cap enhances the QWI has not been elucidated by the experiments in this chapter, but has been shown to significantly enhance the QWI pro-

cess at temperatures above 730 °C. The heat treatment process improves the luminescence efficiency of the material which is particularly desirable for light-emitting or transmitting devices fabricated by this technique. From LTPL measurements it is seen that the oxide-coated samples maintain a higher material quality, as evidenced by LTPL linewidths, than the bare samples, even under extreme anneal conditions that approach homogenization of the QWs. The results from InGaAs QWs are consistent with the dielectric causing preferential intermixing on the Group V sublattice.

The suitability of a number of different laser structures for integration by QWI has been addressed. Structures grown on Zn-doped p-substrates are not suitable for optical integration due to the lack of an enhanced-shift mechanism and the degraded material quality as seen in the LTPL spectra. Partial structures exhibit a lower thermal shift and larger SiO_2-capped shifts than full laser structures, but either type of structure is appropriate. Ternary QWs exhibit a lower thermal shift and yet a larger dielectric-enhanced shift than InGaAsP QWs, however, InGaAs QWs exhibit poorer material quality after anneal as evidenced by the significantly larger LTPL linewidths.

The questions as to how the dielectric shift is manipulated and the origin of the enhanced dielectric blue-shift are discussed in the next two chapters.

Chapter 5

Dielectric-Enhanced QWI

Introduction

This chapter presents band-gap shifting results for samples capped with SOG and SiO_xN_y, as well as the results of experiments designed to further the understanding of the dielectric-enhanced QWI mechanism. The experiments correspond to a wide range of anneal conditions, film preparation methods, and dielectric film thicknesses. Section 5.1 discusses the results of "spin-on glass" films deposited from solution. Section 5.2 discusses the effect of changing the composition of a PECVD SiO_xN_y film. In Sec. 5.3 we present SIMS and microscopy data that examine the migration of semiconductor material into the dielectric films. In Sec. 5.4 we present FTIR data that examines the change in bonding environment of the dielectric films and H loss after annealing. Section 5.5 discusses the effect of changing PECVD thickness. Section 5.6 examines the stress in the dielectric films. The results of this chapter are summarized in Sec. 5.7, while Sec. 5.8 concludes the chapter by proposing a new mechanism for dielectric-enhanced QWI effect in the InGaAsP/InP system, based on the injection of Group V interstitials into the laser structure.

5.1 Effect of SOG Caps

We note in this section that SOG films have no effect on the QWI process in both full and partial standard laser structures, versus either anneal temperature or time. Figure 5.1 presents blue-shift data for MBE# 2958 annealed at 60 s for temperatures of 700–800 °C,

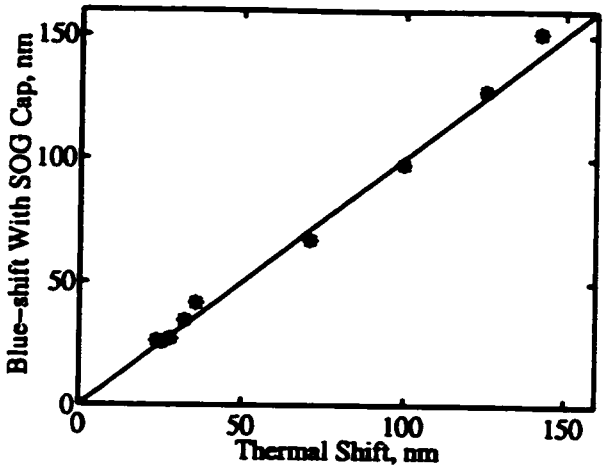

Figure 5.1: Comparison of band-gap-shifting results for SOG versus uncoated samples, annealed at temperatures 700–800 °C for 60 s, and 800 °C for 60–600 s. The straight line indicates a 1:1 relationship.

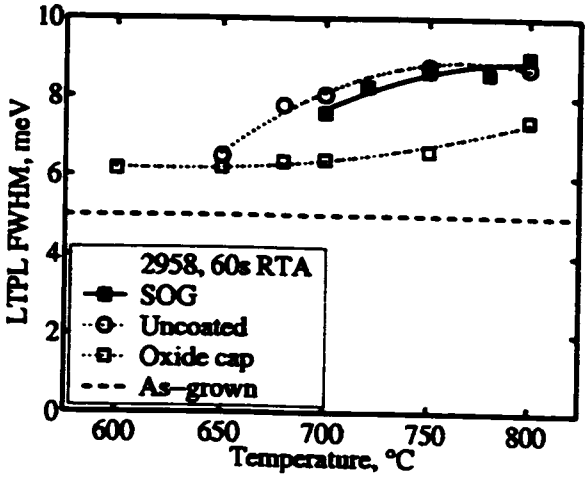

Figure 5.2: Comparison of LTPL linewidths for SOG versus uncoated and SiO_2 samples, annealed at temperatures 600–800 °C for 60 s.

and at 800 °C for times of 60–600 s for both uncoated and SOG-coated samples. Coating the sample surface with SOG reproduces the blue-shifting result for a uncoated sample within ±3 nm. The LTPL information also indicates that the SOG has no effect. In Fig. 5.2 it is seen that the uncoated and SOG-capped samples exhibit the same linewidth within uncertainty, which is significantly larger than SiO_2-capped samples.

SOG films are not without merit since they provide surface protection during the anneal process. This has important applications in device processing since all parts of the sample are protected during the anneal treatment. For example, consider a sample with a 1000 Å SiO_2 film. To selectively modify the band-gap of the sample, the PECVD film is patterned and etched away in areas where a lower band-gap is desired, illustrated in Fig. 5.3. When this sample is sandwiched between proximity caps, for protection during the anneal treatment, there will still be a 1000 Å gap between the InGaAs layer and the proximity cap where the PECVD film has been removed. This is undesirable since the loss of As from the surface will leave the surface In and Ga rich after anneal. To prevent this surface damage the sample is coated with a SOG film that covers both uncoated and PECVD areas. The uncoated surface is now protected, and the SOG does not appear to interfere with the

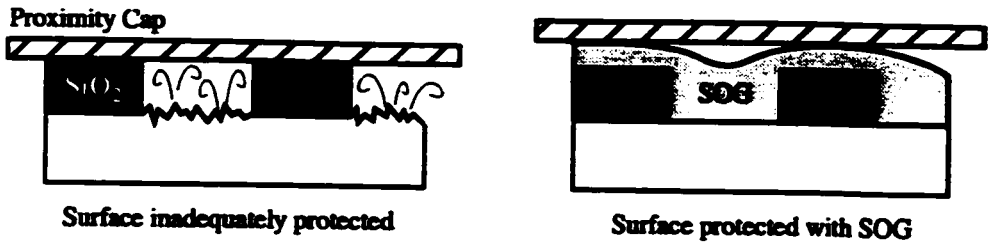

Figure 5.3: Illustration of how SOG is used to protect the surface of a patterned sample.

QWI in the PECVD-coated areas. An example of this is shown in Fig. 6.6, a scanning-PL measurement of a sample that had a patterned PECVD film coated with SOG.

5.2 Effect of PECVD Dielectric Composition

As described in Sec. 2.3 and noted in Table 5.1, the SiO_xN_y films are deposited from a mixture of SiH_4, N_2O, and NH_3 with refractive indexes between 1.478 and 1.727. The composition of these samples is presented in Fig. 2.7. The samples were deposited in a random order onto samples cleaved from MBE# 2958. Figure 5.4 shows the blue-shifting results for these SiO_xN_y films. The film thickness varies from sample to sample, but there is no correlation between film thickness and amount of blue-shift. Therefore, the results of Fig. 5.4 are related to film composition and not film thickness. The net shift increases as the anneal temperature increases, and the maximum blue-shift always corresponds to the sample with the n = 1.655 film. The difference in blue-shift between the n = 1.655 and n = 1.478 films is shown in Fig. 5.4b. At the higher anneal temperatures there is more than 50 nm difference between the blue-shifts of samples coated with these two films. The significance of

CVD Run#	SiH_4 sccm	N_2O sccm	NH_3 sccm	Thickness Å	Index
1089	100	60.0	0	950	1.478
1105	100	52.5	7.5	880	1.553
1099	100	45.0	15.0	930	1.597
1103	100	37.5	22.5	1000	1.625
1097	100	30.0	30.0	810	1.655
1104	100	22.5	37.5	1090	1.688
1106	100	15.0	45.0	1140	1.727

Table 5.1: Summary of PECVD SiO_xN_y films.

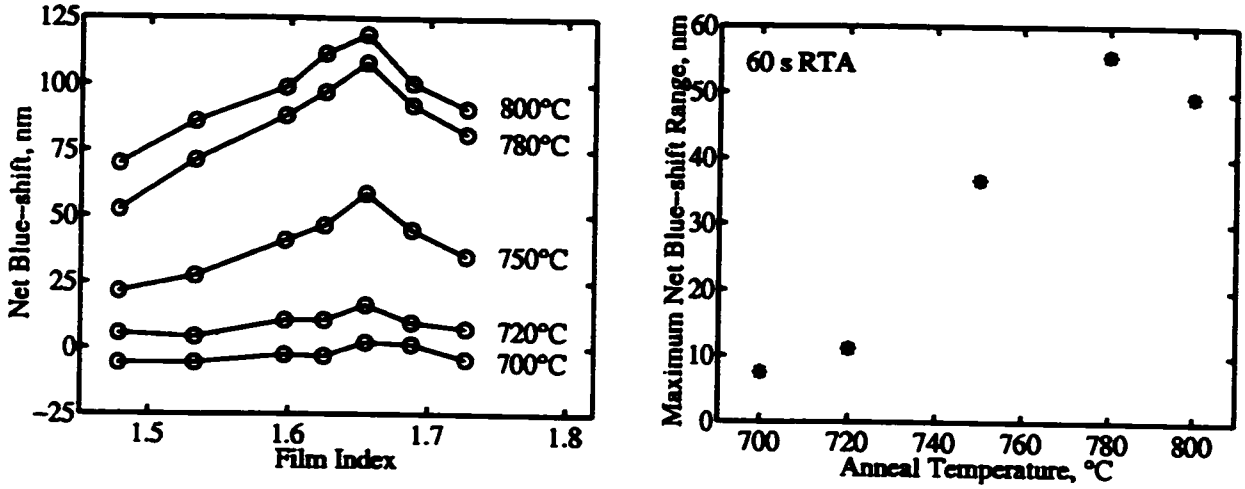

Figure 5.4: Band-gap shifting results for various SiO_xN_y capped samples annealed at 600–800 °C for 60 s: (a) shows the net shift; and (b) shows the difference in net shift between the SiO_2 and n = 1.655 samples.

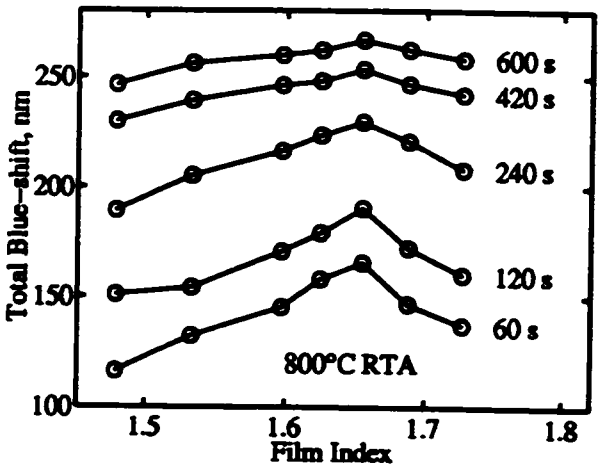

Figure 5.5: Band-gap shifting results for various SiO_xN_y capped samples annealed at 800 °C for the indicated times.

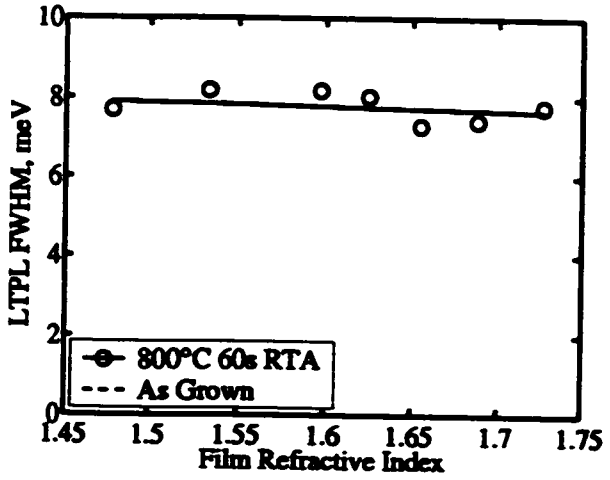

Figure 5.6: LTPL FWHM of various SiO_xN_y capped samples annealed at 800 °C for 60 s.

this result is that a sample patterned with multiple SiO_xN_y films of different composition will result in a sample with multiple areas of different band-gap after annealing. This result was achieved without any optimization of the anneal time or temperature, so it seems reasonable that this range can be extended.

Blue-shift saturation effects are observed in all of the different PECVD-coated samples when the total shift is $\approx$ 260 nm, as shown in Fig. 5.5. The QWs are expected to be nearly homogenized at this point. Even so, at the extreme anneal of 800 °C 60 s the n=1.655

film shows the largest shift. The intermixing of the homogenized wells with the rest of the surrounding 1.24 Q material will continue to cause a blue-shift, but will do so at a slower rate since the "well" is now much wider and similar to the barrier in composition. For this reason, the difference in blue-shift between the samples decreases as the anneal duration increases.

Figure 5.6 shows LTPL results of SiO_xN_y capped samples annealed at 800 °C for 60 s. All samples have the same linewidth within ±1 meV, and there is no significant band-tailing in the samples. Therefore, annealing with the dielectric caps does not degrade the material quality despite the fact that the samples are intermixed much more than uncoated samples.

A device which requires several regions of different band-gap can be prepared using the intermixing results so far discussed in this section. By performing multiple depositions and selective etching steps, one could pattern a sample with dielectric stripes of various compositions. After annealing, this sample would have several gradations in band-gap across its surface. This could range from the shift for the SOG coated sections to the various shift produced by varying the composition of the PECVD film. This method could be used to laterally integrate lasers of different operating wavelength, or a laser-modulator-waveguide, for example.

We have observed the dependence of band-gap-shift on PECVD film composition before under different film deposition conditions, as shown in Figs. 5.7 and 5.8. The films of Fig. 5.7 were prepared using low flow rates of N_2O and no NH_3. The peak blue-shift occurs at a lower refractive index value, and there less net shift in the films prepared this way. The results of Fig. 5.8 were for films deposited using NH_3 and correspond to individual depositions, and indicate a large scatter. It was later deduced that the RF power supply, which generates the plasma, was faulty. Consistent results were achieved upon replacement of the supply and, hence, the faulty supply is believed to be responsible for the scatter. Although these results have no direct application, they do suggest that there is dielectric composition range where the intermixing effect is larger. The H content of PECVD films is discussed in Sec. 5.4, but it is worth noting here that inconsistent concentrations of Si–H

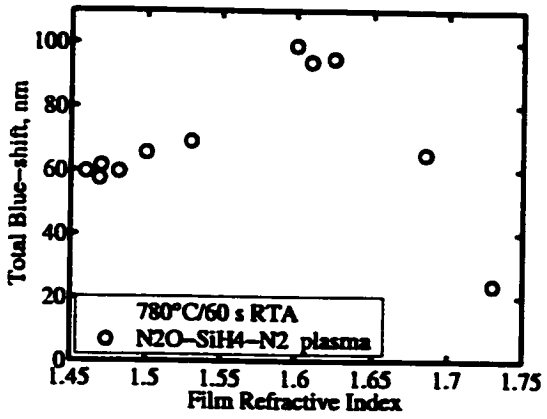

Figure 5.7: Band-gap shifting results for various SiO_xN_y capped samples 800 °C for 60 s. The PECVD films were deposited from SiH_4-N_2 and N_2O.

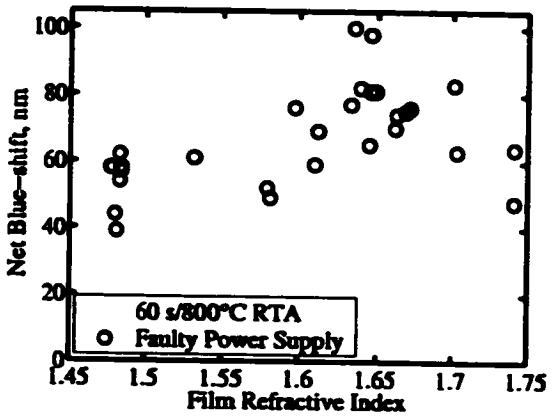

Figure 5.8: Band-gap shifting results for various SiO_xN_y capped samples 800 °C for 60 s. The PECVD RF power supply was diagnosed during this time to be faulty.

bonds were found in these films (Fig. 5.8) while negligible Si–H was detected in the set of films discussed earlier in this section (Fig. 5.4a). It is not known if the presence of the Si–H is symptomatic or problematic, but a link between H in the film and the enhanced QWI process.

5.3 Migration of Ga and In into the Dielectric Film

We have studied the migration of semiconductor material into the dielectric film to determine both the amount of material entering the dielectric film, and the manner in which it does so. SIMS measurements quantify the amount of migrating material and its penetration into the dielectric, while TEM and AFM are used to examine what is happening at the dielectric-semiconductor interface.

5.3.1 SIMS Measurements of Ga and In

SIMS samples were composed of both SOG and SiO_xN_y films on InGaAs, and studied as a function of film composition, deposition method, and annealing conditions. The SIMS data analysis technique is covered in Sec. 3.2. The enhanced QWI induced by these films was presented in Sec. 5.2.

The first experiment was designed to determine which semiconductor species migrated

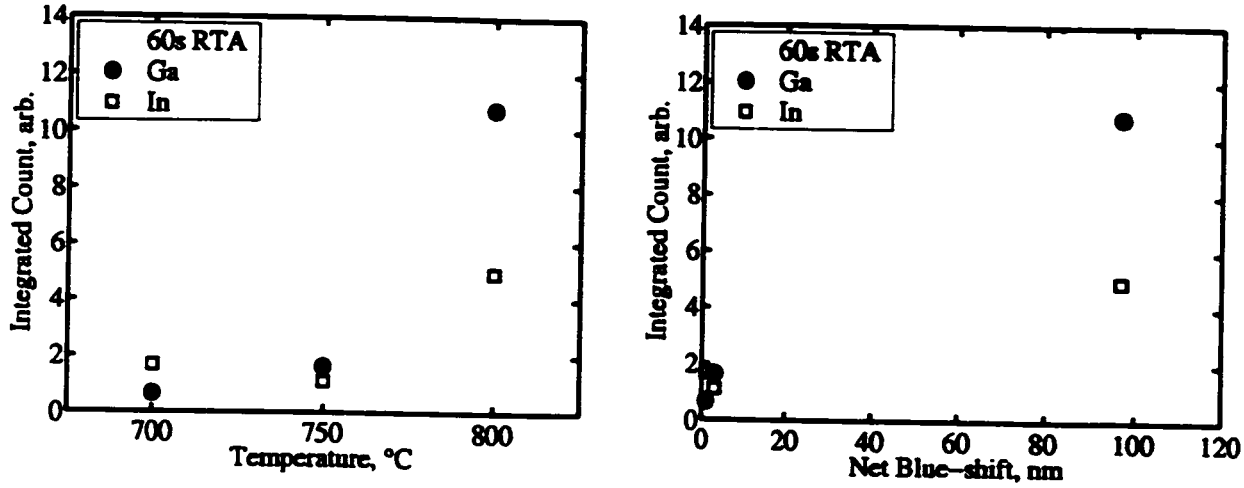

Figure 5.9: Integrated amount of In and Ga which migrate into an n=1.61 dielectric film as a function of anneal temperature for 60 s anneals (a) versus temperature, (b) versus blue-shift.

into the dielectric film. Two samples, one with the dielectric in contact with InGaAs and the other with the dielectric in contact with InP, were examined. The dielectric was an n = 1.61 SiO_xN_y film deposited using a 12 sccm N_2O flow. The level of As in the dielectric film in each of these two samples was essentially the same (not shown), indicating that the measured level was a background and that As does not migrate into the dielectric film, within the detection limits of the SIMS apparatus; the same was true for P. In and Ga were seen to migrate into the film, so consequently the following discussions are for only In and Ga.

The migration of Ga and In into the dielectric film does not begin until the anneal temperature is high enough to produce the enhanced QWI effect. Samples capped with a film of refractive index n=1.61 (prepared 12 sccm N_2O) were annealed for 60 s at 700, 750, and 800 °C. The amount of Ga and In that migrate into the film, as determined by integrating the modified SIMS data with respect to distance into the film, is shown in Fig. 5.9 as a function of both temperature and blue-shift. The units are left as "arbitrary" since there is no calibration factor available for In. The Ga and In yields in the dielectric do not increase significantly until the temperature exceeds 750 °C, where the enhanced QWI effect becomes manifest. The Ga yield at 700 and 750 °C corresponds to $2.8 \times 10^{13}/cm^2$ (2.3 % monolayers, where one monolayer is equal to four atomic planes of either Group III or V atoms), and may be either a background level that was not adequately removed or may be a result of

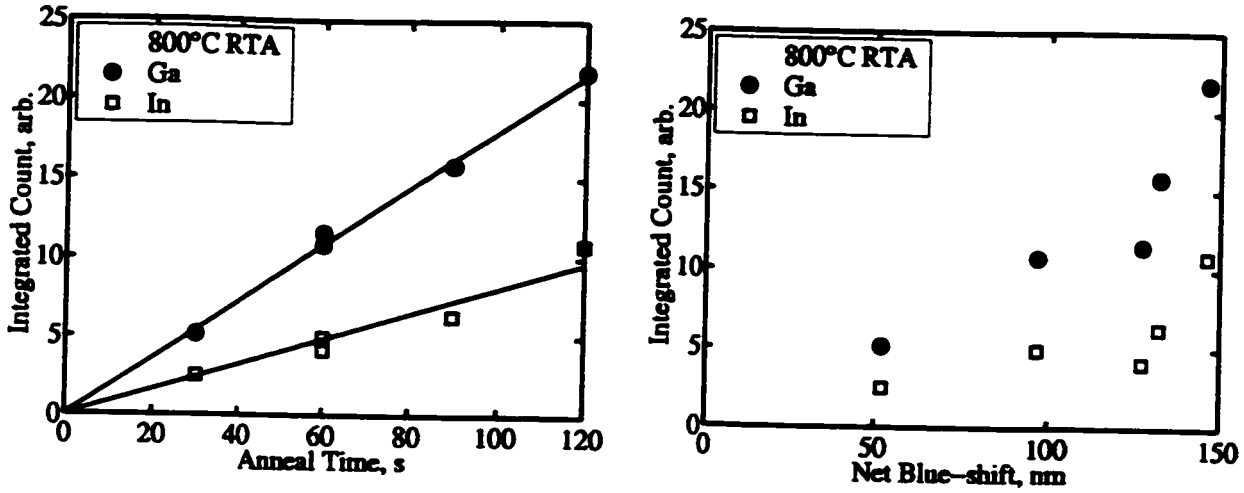

Figure 5.10: Integrated amount of In and Ga which migrate into an n=1.61 dielectric film as a function of anneal time (a) versus time, (b) versus blue-shift.

the plasma sputtering the sample during the first moments of film deposition. This behavior with respect to temperature links the migration of semiconductor material into the dielectric film with the dielectric-enhanced QWI process.

Figure 5.10 presents SIMS data showing how the total migration of Ga into an n=1.61 dielectric film (prepared using 12 sccm N_2O) behaves with respect to increasing anneal time at 800 °C. The integrated amounts of Ga and In correlate with both the anneal time and amount of band-gap shift that the sample experienced. The amount of Ga incorporated into the film after the 120 s anneal was $\approx$ 40 % of a monolayer. This result, together with the temperature dependence of the migration, indicates that the dissolution of Group III species into the dielectric film directly correlates with the physical process which enhances the QWI.

As noted in Sec. 5.2 the amount of blue-shift varies with SiO_xN_y composition. Films of refractive index n $\approx 1.63 \pm 0.02$ produce the largest amount of blue-shift by either deposition method studied. Samples prepared using both dielectric deposition methods were annealed at 800 °C for 60 s, the results are shown in Figs. 5.11 and 5.12. There is a maximum in the integrated SIMS yield corresponding to films of refractive index between 1.50 and 1.55, which does not correspond to the films which induce the largest blue-shift. Additionally, as the film composition is changed from an oxide to an oxy-nitride, the penetration depth, L_D, of the semiconductor material into the film sharply decreases, as shown in Fig. 5.13. This

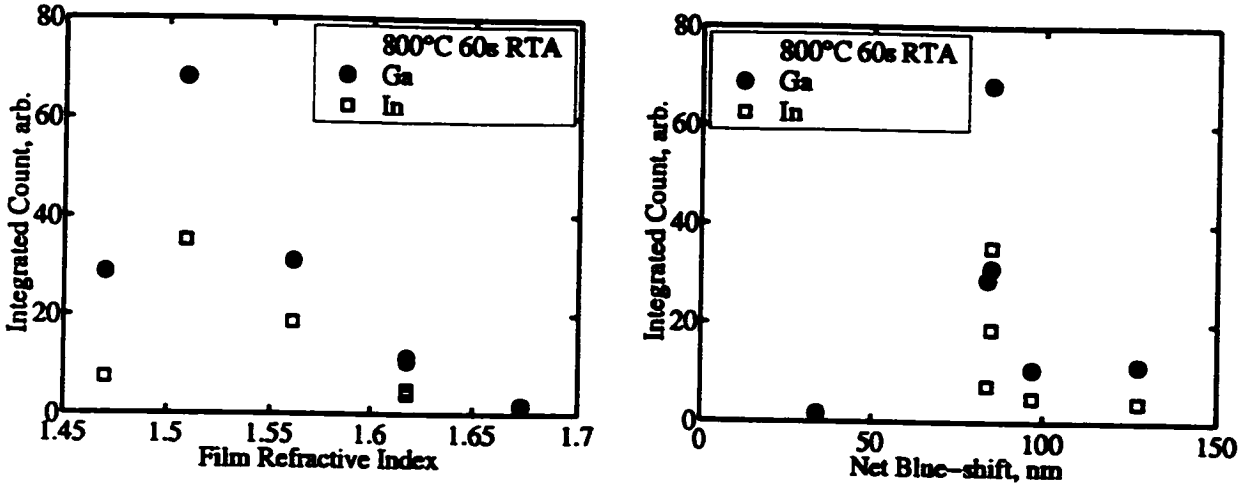

Figure 5.11: Integrated amount of In and Ga which migrate into a SiO_xN_y film as a function of film refractive index, (a) versus film index, (b) versus blue-shift. The SiO_xN_y films are prepared by the low N_2O flow method.

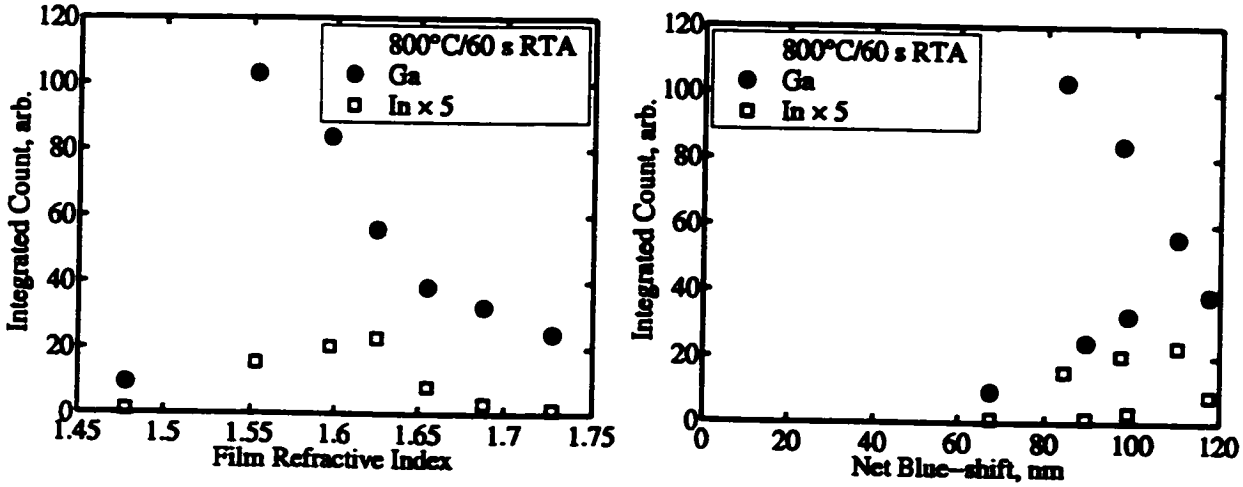

Figure 5.12: Integrated amount of In and Ga which migrate into a SiO_xN_y film as a function of film refractive index, (a) versus film index, (b) versus blue-shift. The SiO_xN_y films are prepared using NH_3.

value was determined by fitting a decaying exponential, $A\exp(-t/L_D)$, to the profile. This decrease in L_D with SiO_xN_y composition makes physical sense because it is known that the Group III elements diffuse more easily in oxides than in nitrides. Ga appears less mobile than In, in the dielectric films.

One further sample, with a SOG film, was studied by SIMS. The integrated yield and penetration depth were greater than those measured in PECVD oxide films. Since the

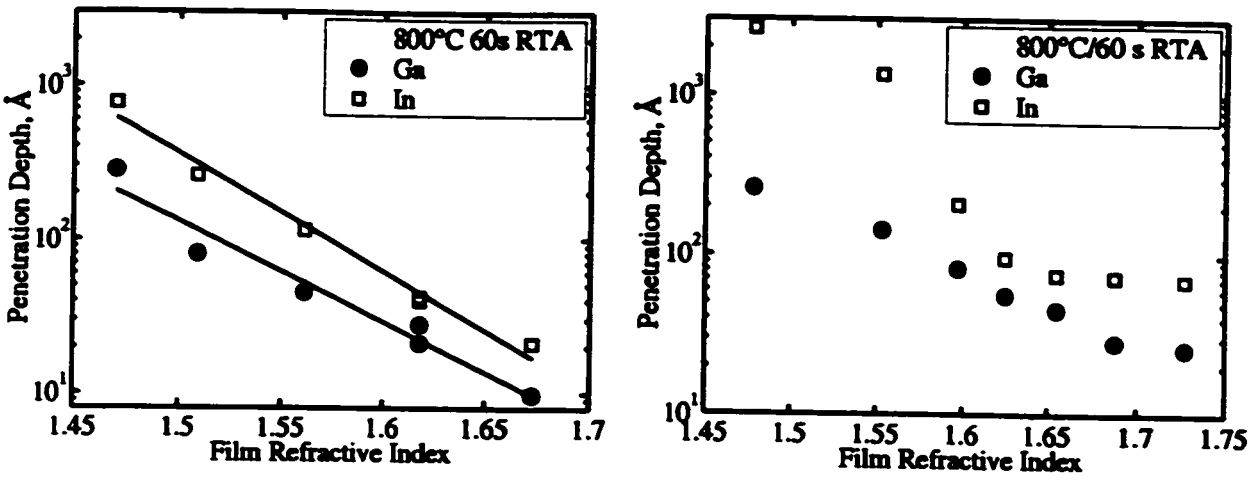

Figure 5.13: Measured penetration depths of Ga and In into the dielectric films as a function of film composition (a) low N_2O flow plasma, (b) NH_3 plasma.

films are deposited by spin-coating and a cure at 210 °C, it seems unreasonable that the In and Ga would have migrated before the anneal treatment. Therefore, even though a large amount of material is incorporated into the SOG dielectric cap during the high-temperature anneal, there is no enhanced blue-shift. Although this is a surprising result, it is consistent with the previous experimental observation that the total amount of material that migrates does not necessarily correlate with the amount of blue-shift.

There are two possible explanations for the migration behavior of Group III species into the SiO_xN_y films. Either the SIMS yield is dependent on film composition, or that the blue-shift is related to factors other than the amount of semiconductor which migrates into the dielectric film, such as film stress. Dielectric-induced stress has been shown to play a role in the defect migration and QWI behavior of samples capped with patterned SiO_2 and SiN_x films [58]. We believe that the SIMS yield does not differ significantly between samples, since care has been taken to saturate the ionization yield by using oxygen as the sputtering agent. Additionally, the Si signal, from sample to sample, has a value within a range of $(2.4 \pm 1.1) \times 10^5$ counts/s which does not correlate with sample O content. Even if the calibration value changed by an amount comparable to the range in Si values (a factor of ≈ 2), it would be not significant enough to produce the peak where the values range over a factor of 10. Therefore, even though the results from PECVD films indicate

that the migration of material into the dielectric film is necessary for the enhanced QWI process, the resulting blue-shift depends on factors other than the amount of material which has migrated. This is most clearly illustrated in the SOG films, which do not produce an enhanced blue-shift as shown in Fig. 5.1, but which clearly accumulate Ga and In during the anneal process.

This data differs from reports that relate the total amount of blue-shift to the solubility of Ga in the dielectric cap [59]. A study of Ga migration from GaAs samples into SiO_xN_y films [19] concluded that as the film composition tended towards SiN_x then the amount of Ga migration decreased, along with a corresponding decrease in the EL5 trap concentration, thought to be related to Ga vacancies. They took this as evidence that a Ga vacancy complex (like an As antisite paired with a Ga vacancy) was responsible for the observed behavior. The study did not examine the optical properties of the samples. The migration of Ga and As from a GaAs substrate into a SiO_2 film has been studied using X-ray photoelectron spectroscopy [60]. This study identified that As does not migrate into the film, and is left as elemental As at the interface. Elemental Ga was found throughout the film, and there was a buildup of Ga_2O_3 at the interface as well.

5.3.2 Microscopy

Tapping-mode atomic force microscopy (AFM) was used to examine the surface morphology of the samples before and after annealing. Uncapped samples examined before and after a 60 s 800 °C anneal showed no significant difference in the surface morphology of the InGaAs surface layer. Dielectric-coated samples examined before and after a 60 s 800 °C anneal showed no difference in the surface morphology of the film: the surface was smooth and even. A third set of AFM samples were prepared from SiO_2-coated specimens; one was not annealed and the other two were annealed for 60 s at 700 and 800 °C. The samples were then etched for 3 minutes in BHF to remove the oxide film and expose the InGaAs layer. The results are shown in Fig. 5.14. The figure clearly shows a reasonably smooth surface in the as-grown sample, followed by a roughening of the sample surface after the 700 °C anneal,

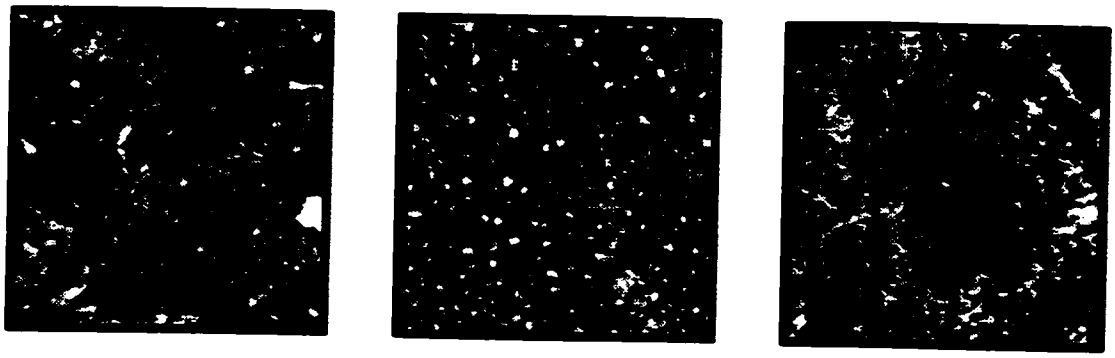

Figure 5.14: Plan view of $1 \times 1\,\mu$m AFM images of a InGaAs surface after a 3-minute BHF etch following various anneal temperatures. (a) not annealed, (b) 700 °C 60 s, (c) 800 °C 60 s. Note the increase surface roughness followed by appearance of pits. The height scale from black to white corresponds to 2.5 nm.

and finally the formation of pits in the sample after the 800 °C anneal. The pits are roughly 12 ± 5 nm in diameter and 1.0 ± 0.3 nm deep. Another set of samples with SiO_2 films was heat treated at 820 °C for 30–90 s, and wet etched to remove the SiO_2 films. The results (not shown) show an increase in the density and size of pits in the annealed samples. These results suggest that the movement of In and Ga from the surface into the dielectric film is not homogeneous over the surface of the sample. A rough estimate of the pit size and density suggests the loss of a large amount of material from the surface, however, this does not mean that the material has migrated into the dielectric during the anneal process. The BHF etchant may be etching more material away if the surface has become oxidized. The islands and pits on the surface of the sample may be related to LCM (although one might expect the islands to be elongated), since lattice-matched InGaAs exhibits this behavior [38]. Similar island features have been noted before in as-grown MBE layers which are deep within the spinodal isotherm [61], and these features are of similar appearance and size. If this is so, then a naive way to interpret the islands is that they are regions with a mean larger lattice constant, and therefore a lower band-gap. We have not yet been able to determine if these features are related to the inhomogeneous nature of the dissolution process.

We have used TEM to examine the samples in cross-section, viewing in the [011] direction. Representative bright-field images for a sample before and after a 60 s 800 °C anneal are shown in Fig. 5.15. Visible in these images is a 2000 Å InGaAs layer on InP,

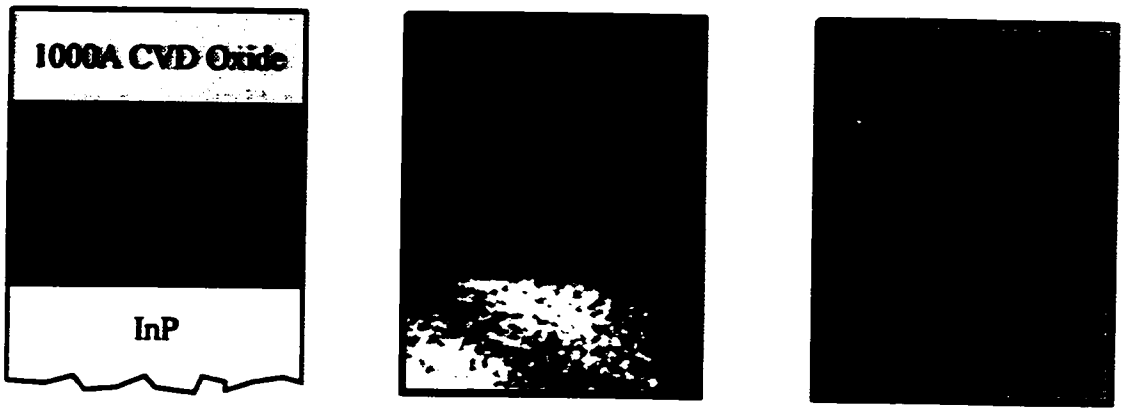

Figure 5.15: Schematic cross-section and TEM images of an oxide film on InGaAs before and after 800 °C 60 s anneal.

coated with a 1000 Å oxide film. The most apparent difference between the two samples is the appearance of dark contrast features in the annealed sample, at the top of the InGaAs layer adjacent to the film-InGaAs interface. We believe these features to be related either to an interface strain or to the pits which are unearthed after etching in BHF (Fig. 5.14). The fact that the contrast fringes are localized at the surface suggests that strain at the interface may play a role in the dielectric-enhanced QWI process. A more subtle point regarding the TEM cross section is that the oxide film shows no local ordering, either before or after annealing. This confirmed by the fact that selected-area diffraction patterns of the film (not shown) exhibit only diffuse rings.

5.4 FTIR and H Loss

Dielectric films were examined using FTIR spectroscopy by the method outlined in Sec. 3.4. In the first study a set of SiO_2 films was annealed for 60 s at temperatures between 600–800 °C. This experiment was to determine if there was a correlation between the film properties after anneal, and the temperature dependence of the dielectric-enhanced QWI. The films change significantly after anneal, as shown in Fig. 5.16; however, the FTIR spectra of the annealed films are all nearly identical, regardless of anneal temperature. Therefore, there was no correlation between the annealed film properties and the temperature dependence of the dielectric-enhanced QWI. There were no significant changes in the intensity

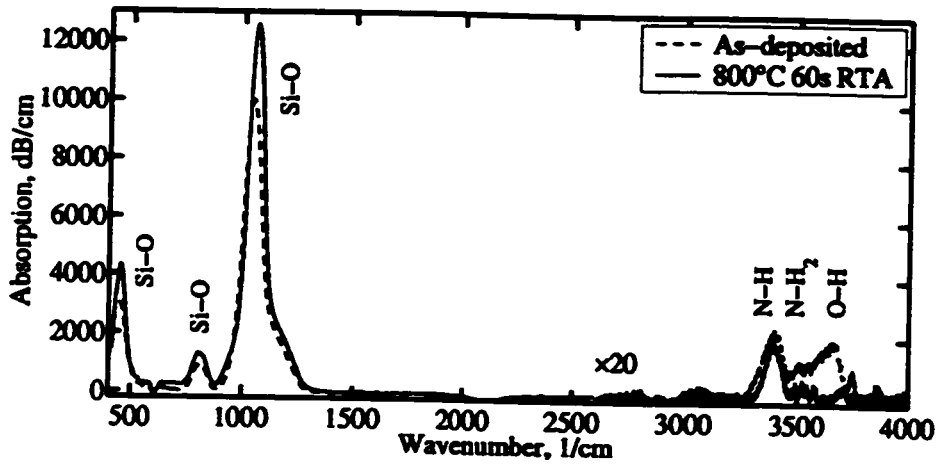

Figure 5.16: FTIR spectra of an SiO_2 film before and after annealing at 800 °C for 60 s.

or FWHM of the main Si–O feature, although the wavenumber increased from 1055 to 1060 cm^{-1} over this range, indicating that this bond is tending towards that of higher quality thermally grown SiO_2. The changes in the N–H bond feature were similarly subtle. After anneal the position decreased from 3404 to 3397 cm^{-1} indicating that the N atoms concerned with the N–H bonds are attached to a larger number of either Si or H atoms since the electronegativity of O would increase the bond energy (see discussion on page 32). Bonding to H is ruled out since the N–H_2 feature at 1560 cm^{-1} and 3500 cm^{-1} corresponds to at most $1 \times 10^{20}/cm^3$, and is therefore too weak. This leaves the conclusion that the cross-linking of the film is being increased and, that overall, the incorporated N atoms are bonded to a greater number of Si atoms. The total amount of H lost is $1.65 \pm 0.15 \times 10^{21}/cm^3$. Essentially all of the O–H is released during the 600 °C anneal. Both H features in the annealed films are weak, and noise prevents accurate measurement of their FWHM.

A second experiment was done using a range of SiO_xN_y films, deposited from NH_3 plasmas, and annealed at 800 °C for 60 s. The discussion of these features is more complicated since the films contain a significant amount of N. We first consider the main feature of the FTIR spectrum, Fig. 5.17, which is a superposition of various Si–O and Si–N vibration modes. The spectra for the annealed film of refractive index n = 1.597, which corresponds to $SiO_{1.4}N_{0.8}$, shows most clearly that there are two dominant contributions to the overall feature. These are associated with the in-phase stretching mode of the Si–O and Si–N bonds.

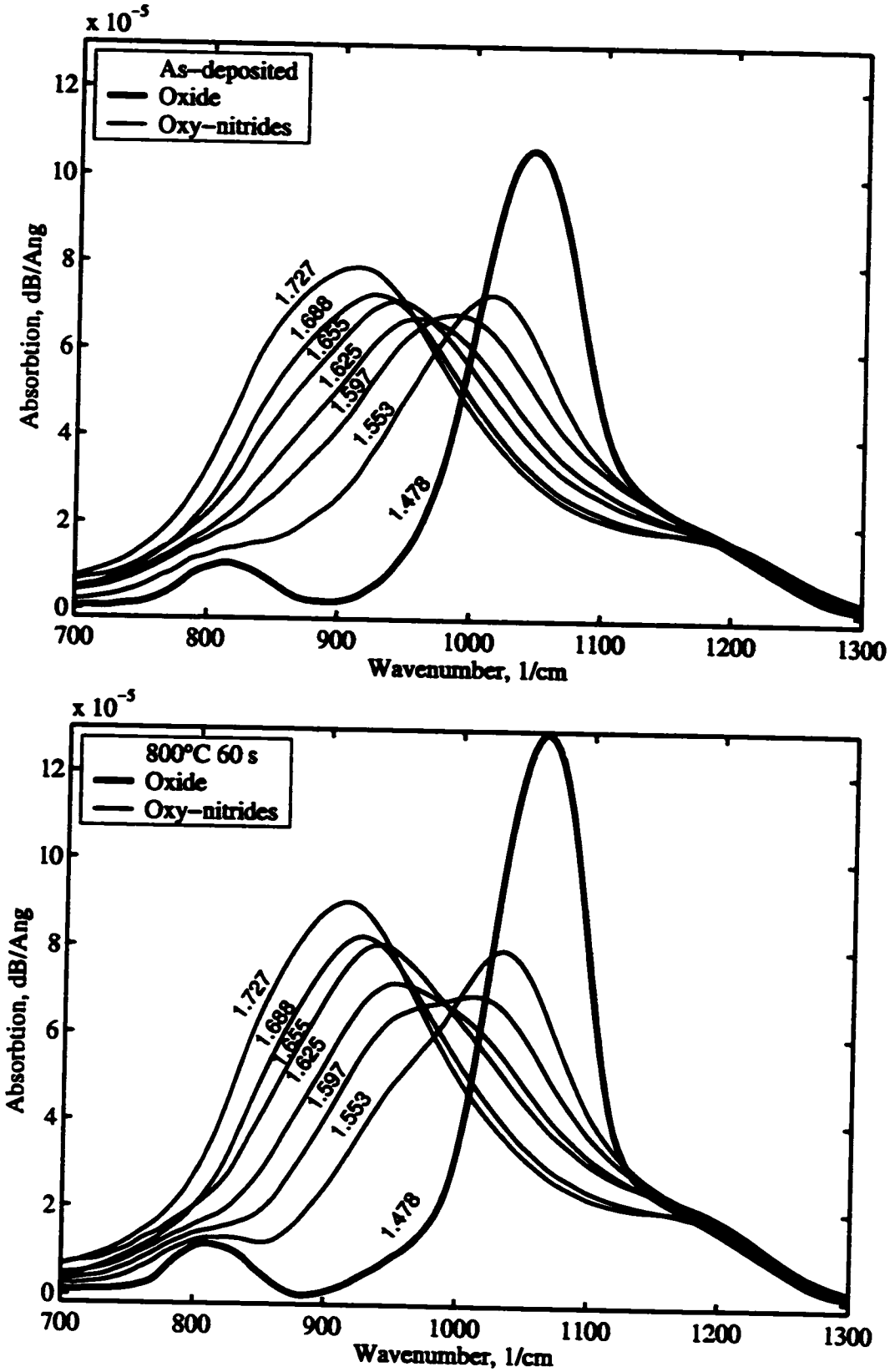

Figure 5.17: FTIR absorption spectra of the Si–O/N feature in SiO_xN_y films (a) as-deposited films, (b) after 800 °C 60 s anneal.

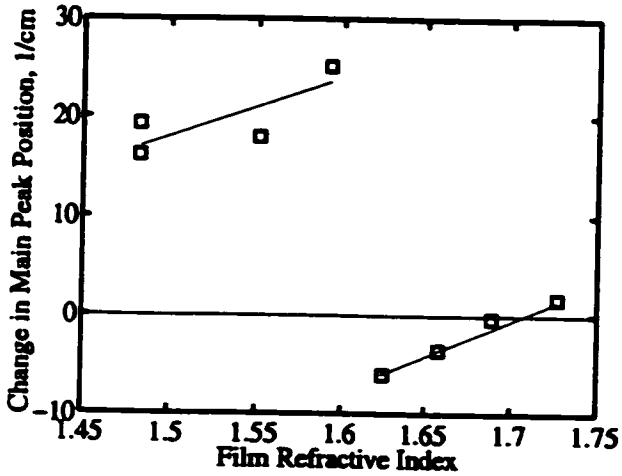

Figure 5.18: Change in position of main feature after 800 °C 60 s anneal.

However, these bond energies vary depending on the film composition, since the average ratio of O to N atoms bonded to a Si atom changes. In other words, as the N content of the film increases, an increasing number of N atoms, which have a lower electronegativity than O atoms, will be back-bonded to Si–O. The back-bonding of these lower electronegativity atoms will move the position of the Si–O bond to lower wavenumbers, which is seen in Fig. 5.17. The deconvolution of these features is therefore not attempted since the positions are not well known, and there are also contributions from vibrational modes other than the Si–O and Si–N in-phase stretch. The shoulder at 1200 cm^{-1} is related to both an asymmetrical stretching mode of Si–O and a vibrational mode of N–H. The shoulder peak around 800 cm^{-1} is related to additional vibrational modes of Si–O and Si–N. Upon annealing the intensity of the main feature increases, and the Si–O and Si–N features appear to become more distinguishable. The position of the main feature tends to move towards that of either a Si–O bond (increasing wavenumber) for O-rich films, or a Si–N bond (decreasing wavenumber) for N-rich films, as shown in Fig. 5.18. The composite feature sharpens in linewidth, excepting the case of the $n = 1.597$ film where the two principal features are of similar intensity and the overall feature simply widens. Nothing about the behavior of this composite peak directly correlates with the blue-shifting or SIMS results, however, it is clear that the bonding environment of the film is significantly changing, which will likely influence the film stress.

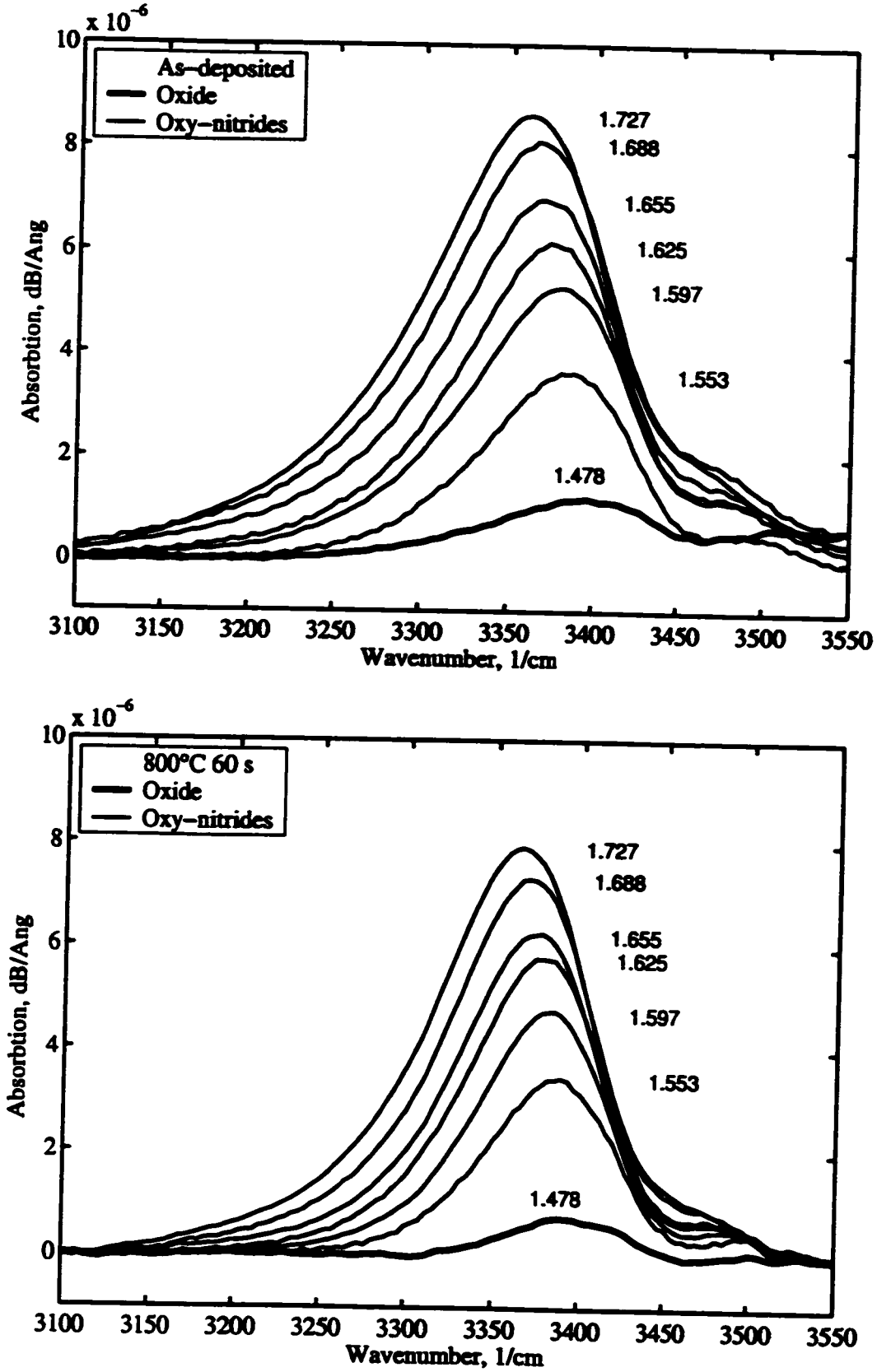

Figure 5.19: FTIR absorption spectra of SiO_xN_y films N–H feature (a) as-deposited films, (b) after 800 °C/60 s anneal.

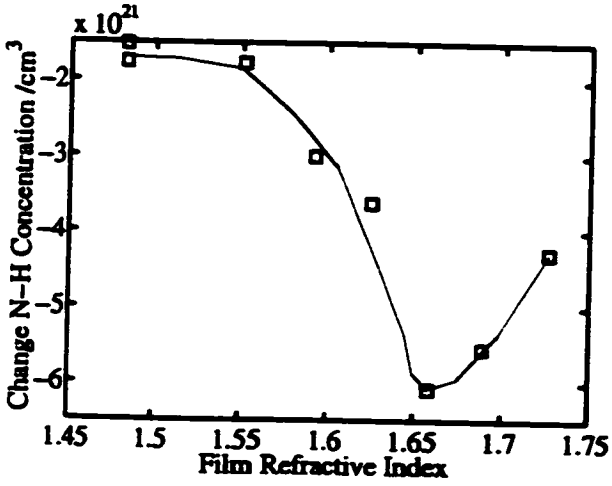

Figure 5.20: Change in concentration of N–H bonds after 800 °C 60 s anneal.

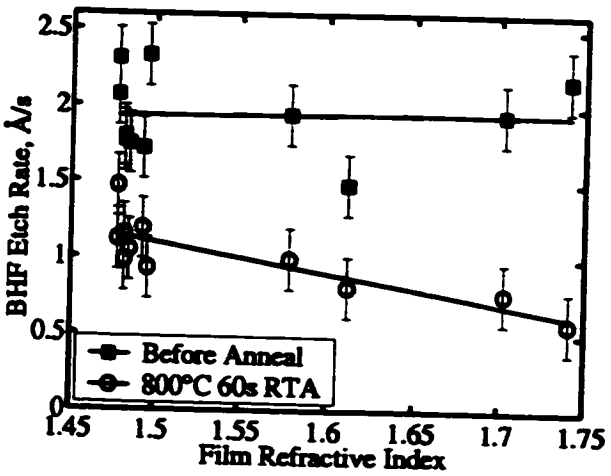

Figure 5.21: BHF etch rate of SiO_xN_y films deposited from a NH_3 plasma both as deposited and after a 800 °C 60 s anneal treatment.

All SiO_xN_y PECVD films contain a significant concentration of N–H bonds, only SiO_2 films contain O–H bonds, and none of the films deposited by this method contain measurable concentrations of Si–H bonds. The feature above 3500 cm^{-1} in the SiO_2 film is due to O–H bonds. The position of the N–H feature tends to lower wavenumbers as the N content of the film increases, Fig. 5.19, consistent with the decreasing amount of O in the film. The shoulder between 3480–3500 cm^{-1} may correspond to N–H_2, although there is no corresponding feature at 1545 cm^{-1} for the scissor mode. The N–H content steadily increases with N content in the film, as can be seen from examination of Fig. 5.19. The loss of H from N–H bonds after annealing, Fig. 5.20, correlates with the enhanced QWI effect observed versus SiO_xN_y film composition. After anneal the films also experience a refractive index change of -0.008 ± 0.002 and a thickness change of -0.004 ± 0.006 %, independent of SiO_xN_y composition. Since the H loss varies significantly from sample to sample, it does not seem likely that the reduction in refractive index is from the films losing H and forming voids; however, this does not rule out the index change as a chemical effect. We finally note, as additional proof that the chemical structure of the films has significantly changed, that the wet chemical etch rate in BHF is significantly reduced after annealing, as shown in Fig. 5.21. This is evidence that the films have indeed lost H and that there are fewer dangling bonds

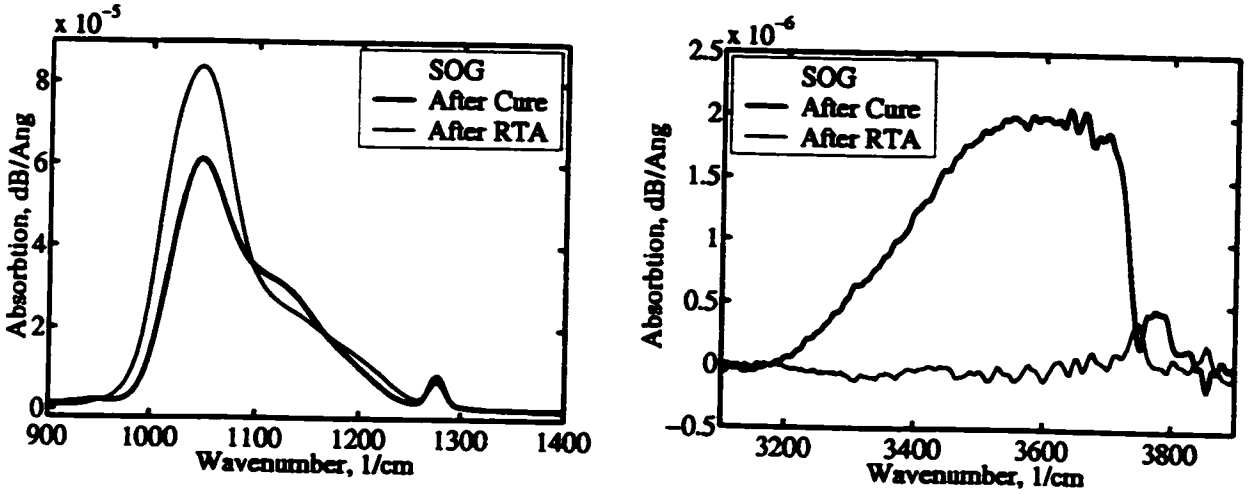

Figure 5.22: FTIR absorption spectra of SOG films before and after anneal at 800 °C for 60 s: (a) Si–O feature, (b) H-related band. The feature at 1278 cm^{-1} corresponds to Si–CH_3 groups.

in the film. The etch rates of the films with high N content are still larger than high-quality SiN_x films, which is likely due to the remaining H content in the film.

We noted previously on page 66 of Sec. 5.2 that a faulty power supply was responsible for erratic QWI results, and that the films deposited during this time had measurable and erratic concentrations of Si–H bonds. It seems reasonable, considering the behavior of the N–H bonds and this correlation with Si–H bonds, that the bonding arrangement of the film affects the dielectric-enhanced QWI process.

FTIR spectra of a SOG film after curing at 210 °C for 24 hours, and after subsequent annealing at 800 °C for 60 s, are shown in Fig. 5.22. The film index and thickness measured by ellipsometry change from (n, t) = (1.422, 1084 Å) to (1.400, 1004 Å) after anneal. After annealing, the intensity of the main Si–O feature is greatly increased with a corresponding decrease in FWHM and a reduction in the size of the shoulder at 1150 cm^{-1}. While the position of the Si–O feature does not move, it is clearly seen that the tail extends to lower wavenumbers. The broad H-related band at 3600 cm^{-1} also disappears, and the C–H_3 feature at 1280 cm^{-1} decreases in area by 71 ± 3 %. The film did not have a measurable quantity of Si–H bonds. The SOG films clearly lose a significant amount of H, $\approx 1 \times 10^{22}/cm^3$, but, they do not produce an enhanced QWI effect. The loss of H alone is therefore an insufficient condition to produce dielectric-enhanced QWI.

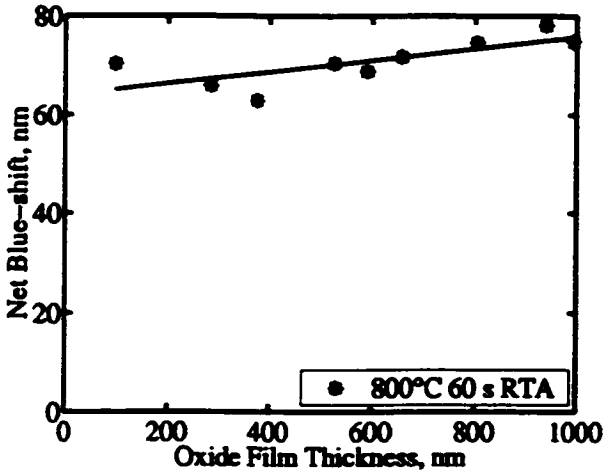

Figure 5.23: Net Blue-shift of partial laser structure annealed at 800 °C for 60 s with varying oxide thickness. The films were wet chemical etched in BHF to achieve different thicknesses from the as-deposited 1000 Å film.

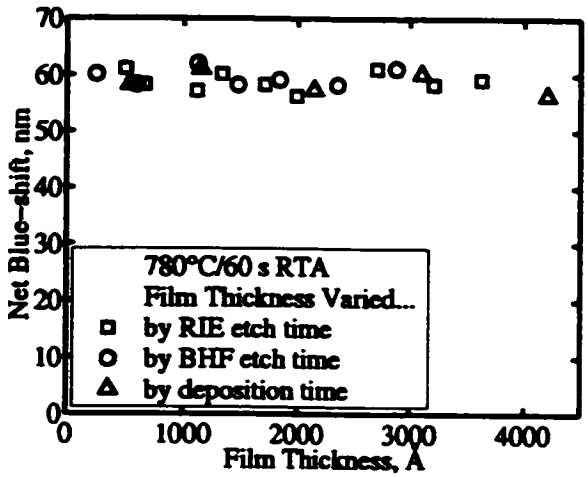

Figure 5.24: Band-gap shifting results for various thicknesses of an n=1.61 film prepared using 12 sccm N_2O. Different thicknesses were achieved by different deposition times, and different wet and dry etch times. Samples were annealed at 780 °C for 60 s.

5.5 Effect of PECVD Film Thickness

The PECVD film dielectric thickness does not appear to play a large role in the enhanced QWI process in the samples we have studied. This was suggested by the results of Sec. 5.2, and is shown explicitly in Figs. 5.23 and 5.24 for SiO_2 and n = 1.61 SiO_xN_y, respectively. Both of these films were deposited using a N_2O-SiH_4 mixture. The SiO_2 film was prepared to different thicknesses on MBE# 2958 using a BHF etchant, and samples were annealed for 60 s at 800 °C. The results show a weak film thickness dependence of $\approx$ 1 nm less blue-shift for every 100 Å of film etched. The other thickness study was done using an n = 1.61 SiO_xN_y film deposited on MBE# 2263 (a full laser structure like 2880) annealed at 780 °C for 60 s. These samples showed no dependence on film thickness ranging from 300–4000 Å, prepared by either wet chemical etching, CF_4/O_2 plasma reactive ion etching, or by varying the film deposition time.

As is shown in Fig. 5.13, these results are consistent with the penetration depth, L_D, of Ga and In into the dielectric films. In SiO_2 films $L_D \approx 1000$ Å, and decreases strongly as the N content of the film increases. If the thickness effect is due to the saturation of the

dielectric film with semiconductor material, then it is reasonable to expect a lower blue-shift in samples with thin ($\ll$penetration depth) films. However, the net blue-shift changes by less than 25% when the SiO_2 film thickness is reduced from 1000 Å ($\approx$penetration depth) by a factor of 5, as shown in Fig. 5.23. We, therefore, conclude that saturation effects, if present, are not a significant factor in determining the amount of dielectric-enhanced QWI.

It has been observed in other work that the magnitude of the blue-shift increases with encapsulant thickness [59, 15] in GaAs based structures, but not in InGaAs/InP structures [59] or all-InGaAsP active regions [30]. This was attributed to the finite solubility of Ga in the film and, hence, a limited number of vacancies were introduced into the material thereby limiting the magnitude of the blue-shift. In a study of phosphorus-doped SiO_2 films [59] it was believed that P atoms migrated from the SiO_2 cap into the semiconductor in the form of interstitials thus producing an enhanced blue-shift. This is not possible in our undoped films; however, it does suggest that Group V interstitials injected into the QW structure will promote disordering.

5.6 Film Stress Measurements

Measurements of SiO_xN_y film stress at room temperature before and after annealing do not show any correlation with the amount of blue-shift. Films were deposited on 2-inch Si wafers and tested in the manner described in Sec. 3.5. The results, Fig. 5.25, show that the as-deposited films are under compressive stress at room temperature. This seems reasonable since the thermal expansion coefficient of the film is less than that of the underlying substrate, and that the deposition is performed at 300 °C. After a 750 °C 60 s anneal the SiO_xN_y films, especially those of higher refractive index, tend towards tensile stress. This is related to the loss of H from the films and the decreased number of dangling bonds which increase the cross-linking in the film.

It is expected that the thermal expansion coefficient of SiN_x is lower but comparable to that of InP, while that of SiO_2 is lower by a factor of ten as shown in Table 5.2. Therefore, at the high anneal temperatures the SiO_2 films will change to tensile stress while the Si_3N_4 films

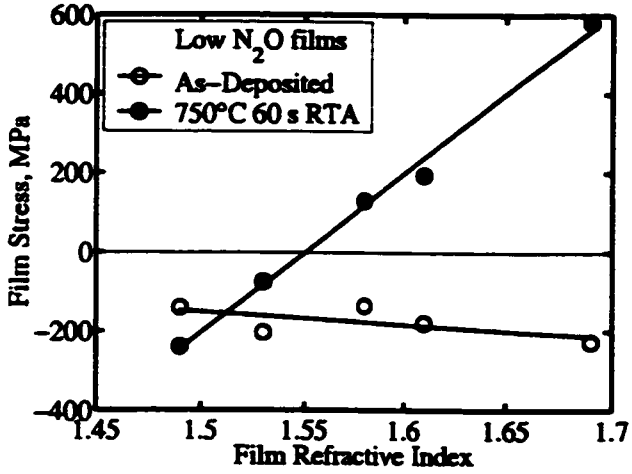

Figure 5.25: Measured film stress for n=1.61 films on a Si substrate. Negative values indicate compressive stress.

Material	α, °C^{-1}	Reference
SiO_2	0.3–0.6 $\times 10^{-6}$	[62]
SiO_2	0.52 $\times 10^{-6}$	[58]
Si_3N_4	2.8 $\times 10^{-6}$	[58]
InP	4.75 $\times 10^{-6}$	[50]
InP	4.56 $\times 10^{-6}$	[63]
GaAs	5.6 $\times 10^{-6}$	[50]
GaAs	6.86 $\times 10^{-6}$	[58]
Si	2.5–4.2 $\times 10^{-6}$	[62]

Table 5.2: Thermal expansion factors, α, for various different dielectric films and substrate materials.

will undergo a much smaller change. Therefore, since the SiO_2 films are under compressive stress at room temperature, there may be a minimum in the tensile film stress at the anneal temperature which would correspond to a minimum in compressive surface stress that the laser structure would experience. The interaction of the film stress with the sample surface may play a role in how the defects are generated and/or injected into the laser structure at the film-semiconductor interface.

It is not likely that the dielectric films influence the QWI behavior by producing an overall bow to the sample. One piece of evidence is the lack of a significant effect as the dielectric film thickness is changed. Additionally, a group of samples were prepared with n = 1.61 PECVD films (12 sccm N_2O) on either the top surface, the back surface, or both surfaces. The thermal mismatch between the film and the substrate would cause the samples to bow in different directions depending on whether the film was on the top or back surface of the sample. Films deposited on both sides would cause the least amount of bowing. The blue-shift results, however, did not differ between these samples. We therefore believe that curvature of the sample, related to the average stress induced in the sample due to the dielectric film during anneal, does not play a role in the dielectric-enhanced QWI. This, however, does not rule out the possibility of local stresses at the semiconductor-dielectric

interface playing a role.

5.7 Summary of Results

The investigation of a number of different films has provided useful candidates for device fabrication. SOG protects the surface and optical quality of the sample without enhancing the QWI process, and is useful as an encapsulating protective layer. PECVD SiO_xN_y films provide an enhanced blue-shift that varies with film composition. The maximum shift occurs for a film of n = 1.655 deposited using NH_3, and n = 1.61 using low flows of N_2O. The films seem to share a common trait that produces the blue-shift peak despite the different precursor gases. Film thickness only weakly affects the QWI process, and is only noticeable in SiO_2 films.

By performing multiple dielectric depositions and selective etching steps, one could ultimately obtain gradations in band-gap across the surface of the sample. This could be used to create complicated structures such as laterally integrated lasers of different operating wavelengths, or an integrated laser-modulator-waveguide.

The SIMS experiments have identified that the migration of Ga and In from the semiconductor into the dielectric film is required for the dielectric-enhanced QWI process. However, the amount of material which migrates does not correlate with the amount of net blue-shift when the film composition is changed. This is most clear in the case of SOG films that do not enhance the QWI at all. FTIR measurements record changes in film bonding structure and H content. The majority of annealing-related changes occur at a temperature lower than 600 °C. In the case of varying SiO_xN_y composition the loss of H from N–H bonds correlates with the amount of net blue-shift. Film stress measurements confirm that the internal stress of the dielectric films is very different after annealing.

5.8 Proposed Mechanism for Dielectric-Enhanced QWI

We do not believe that the enhanced intermixing effect is caused by sputtering-induced surface damage during the plasma deposition process. This is because when the

SiO_xN_y films are etched from the laser structure, we reproduce the same blue-shift for samples which have never experienced a dielectric deposition, unlike studies of sputtered oxide films [18] that record a large blue-shift even after the film is etched away.

For a variety of reasons, we believe that the mechanism by which the PECVD SiO_xN_y films produce enhanced QWI in our InGaAsP/InP samples is through the injection of Group V interstitials which promote the intermixing process. If this is the case, then this method can not be accurately described as "impurity-free". The evidence that brings us to this conclusion starts with the SIMS data that links the migration of both Ga and In into the dielectric film with the enhanced intermixing process versus both time and temperature. However, there is no correlation between the amount of Ga and In which migrate into the film and the amount of blue-shift when the film composition is varied. This is especially true for the case of SOG films which do not produce any enhanced intermixing, yet contain significant amounts of Ga and In after annealing. In the literature it has been postulated that the loss of H from SOG films causes pores which easily accept Ga, which in turn produce Group III vacancies that promote interdiffusion in GaAs/AlGaAs [44]. Certainly, we see a considerable loss of H from all of the films we have studied; however, since our SOG films show a large loss of H upon annealing, yet do not promote QWI, we do not believe that this "pore mechanism" explains the behavior of our samples.

Considering further the H loss from the samples upon annealing, we note that the loss of H, originally bonded as N–H, correlates with the amount of enhanced blue-shift. The FTIR measurements of the samples also indicate significant changes in film bonding structure at temperatures as low as 600 °C, which lead to changes in film stress. This is likely the reason why the higher N content SiO_xN_y films, which lose a large amount of H, change to tensile stress after annealing. The film stress likely plays a role in how the defects are generated and/or injected at the interface between the film and semiconductor. When the film is under tensile stress, the surface of the laser structure is likely under compressive stress. One one hand, the injection of vacancies would help relax this compressive stress; however, if the vacancies follow the strain gradient then they would tend to remain near the

surface where the compressive stress is highest. On the other hand, interstitials would be retarded from forming or entering the laser structure, but following the strain gradient they would move through the active region into the substrate. Under these circumstances the interstitials would not accumulate in the active region, which is consistent with the fact that the luminescence intensity of the sample is not sacrificed by the intermixing process.

Since Ga and In migrate into the dielectric film, this leaves the surface As-rich. We therefore postulate that interstitial As is injected into the structure, and that this is the defect responsible for the enhanced QWI effect. The injection of these interstitials may be mediated by the stress in the dielectric capping layer. This could explain how the blue-shift varies with PECVD SiO_xN_y composition, and why SOG fails to enhance the blue-shift even when it accepts significant amounts of Ga and In from the sample during anneal. The suggestion of Group V interstitials promoting disordering has been postulated before [59] where it was believed that the diffusion of P atoms (used to dope an SiO_2 dielectric capping layer) into a MQW structure created interstitials which promoted disordering. An earlier study of samples annealed under different phosphorus over-pressures [34] exhibited an increasing blue-shift for a phosphorus over-pressure greater than 0.1 atm when annealed at 650 °C for 120 minutes. This was attributed to the injection of P interstitials, since oxide-capped samples exhibited a much lower shift, nearly independent of phosphorus pressure. A diffusion study in GaAs/AlGaAs [64] showed that under an As-rich atmosphere the Al-Ga interdiffusion coefficient was nearly two orders of magnitude greater than under a Ga-rich ambient. This was attributed to the formation of Group III vacancies, but can also be interpreted as evidence for the formation of Group V interstitials.

The hypothesis of injected interstitials is consistent with experiments performed on different types of laser structures. The Group III compositions are nominally identical in both the barrier and QW in our standard structure. It is therefore unclear how the generation of Group III vacancies would enhance intermixing on the Group V sub-lattice. The study of InGaAs versus InGaAsP QWs suggests that the dielectric-enhanced mechanism preferentially disorders the Group V sublattice. This was deduced from the fact that the thermal shift

in the InGaAs QWs was lower while the SiO_2-capped shift was much larger, and that the competition between Group III and V intermixing acts to reduce the total amount of blue-shift.

Related experiments by other groups in our department lend additional support to the proposed Group V interstitial mechanism. As noted previously on page 56, He$^+$-InP material has provided clues into the nature of the thermal shift; similar experiments with SiO_2 films provide a clue to the nature of the dielectric-enhanced QWI process [22]. A SiO_2 film was deposited on a sample which had a layer of He$^+$-InP embedded in the material between the active region and the top InGaAs layer. A comparison of the results between uncoated and SiO_2-capped samples showed that the capped samples exhibited a *smaller* blue-shift when the SiO_2 film was present. It is believed that the defects within the He$^+$-InP material interact with the defects produced via the SiO_2 cap. The lower blue-shift is explained by postulating that the two types of defects annihilate each other, consequently leaving fewer defects overall to promote intermixing in the SiO_2-capped sample. The He$^+$-InP defects are believed to be P-vacancies and vacancy clusters [65]. Group V vacancies would certainly provide a sink for the P and As interstitials, which we postulate are responsible for the dielectric-enhanced process.

The other novel intermixing method being studied in our department [23] uses low-temperature-grown InP (LT-InP). This material is deposited by GSMBE at a growth temperature of 300 °C. It is expected that the material will contain a large number intrinsic defects, especially interstitials. Laser structures nominally the same as MBE# 2958, with an additional layer of LT-InP deposited on top of the InGaAs cap layer, exhibit large amounts of enhanced blue-shift at significantly lower temperatures than samples with PECVD SiO_xN_y films. Although a mechanism for the LT-InP-enhanced QWI has not been conclusively identified, it seems reasonable that grown-in interstitial defects are responsible for the effect. If this is the case, then it illustrates that Group V interstitials enhance QWI.

The question remains as to how Group V interstitials encourage the QWI process. Several possible diffusion mechanisms are [66]:

$V + O \rightleftharpoons O + V$	Vacancy
$(SV) \rightleftharpoons V + S$	Fast Pair Diffusion
$i + V \rightleftharpoons S$	Frank-Turnbull
$I + O \rightleftharpoons S + I$	Kick-Out

where V is a vacancy, O a host lattice atom, S a substitutional atom, i an impurity interstitial, and I a host interstitial. It has been determined that the primary mechanism on the As sublattice in GaAs is the Kick-out mechanism, involving interstitial atoms. Arsenic self-diffusion is dominated by As self-interstitials in GaAs [67]. This substitutional-interstitial diffusion mechanism results in a Fick's-law-shaped profile [66]. It therefore seems reasonable that the Group V interstitials in InGaAsP will produce an intermixing effect though the Kick-out mechanism. In this case an Group V interstitial atom would switch with a Group V host atom producing a new Group V interstitial which would continue the process. Since As self-diffusion is limited by this process in GaAs, this means that the Kick-out process causes the interstitials to interact with host atoms frequently. If the same is true in InP-based materials then this suggests a reasonable likelihood that the As interstitials injected at the surface will create a population of both As and P interstitials as the defects diffuse through the layers of the laser structure. The random replacement of both As and P on the Group V sub-lattice in the vicinity of the QW will cause the enhanced intermixing effect.

Chapter 6

Issues Regarding Device Processing

Introduction

This chapter deals with issues directly related to producing integrated devices from QWI material. The chapter is split into two sections; the first section deals with material properties other than the magnitude of the band-gap shift, and the second deals with practical device fabrication and patterning issues.

6.1 Properties Important for Photonic Integration

This section focuses on material properties that are important for device operation. Waveguides fabricated from intermixed material are characterized to determine the absorption and group index of the material as a function of blue-shift. Scanning PL measurements are presented which examine the area-selectivity of the QWI process in samples that have been annealed with pattered dielectric films. Finally, Hall effect measurements are used to examine the electrical properties of the material after annealing.

6.1.1 Waveguide Absorption and Index

The purpose of Fabry-Perot transmission measurements was to examine the absorption and refractive index of ridge-waveguides fabricated from material which had undergone various amounts of QWI, and to determine the band-gap shifting criteria to produce passive waveguides. The Fabry-Perot characterization technique is presented in Sec. 3.6.

MBE#	Film Index	Anneal Temp., °C	Anneal Time, s	Blue-shift nm	Film Type
2592	uncoated	–	–	0	
2592	uncoated	800	30	40	
2573	1.475	800	30	100	PECVD
2592	1.475	800	30	70	PECVD
2592	1.51	800	30	79	PECVD
2592	1.475	800	60	112	PECVD
2592	1.475	800	90	128	PECVD
2592	1.475	850	30	166	PECVD
2592	1.465	800	30	49	ECR SiO_2
2573	1.9	800	30	67	ECR SiN_x

Table 6.1: Summary of samples prepared for Fabry-Perot waveguide characterization.

The samples were prepared from MBE# 2592 and 2573, a full laser structure similar to MBE# 2827 with an as-grown RTPL peak at 1567 nm. The PECVD dielectric films were deposited using 2 % SiH_4 in N_2 and N_2O. The ECR films are deposited using a microwave electron-cyclotron resonance (ECR) deposition system. The ECR SiO_2 film was deposited at McMaster [68] (ECR# 846), and the ECR SiN_x film was deposited at the NRC. The ECR films were included as part of a collaboration to investigate if the film deposition method affected the material quality. Table 6.1 summarizes the sample preparation and anneal details.

The waveguides were fabricated after the samples were annealed. To begin with, any dielectric film present during the anneal was stripped from the sample using BHF. Standard photolitographic techniques were used to pattern a waveguide etch mask oriented in the <011> direction. A 1:8:80 H_2SO_4:H_2O_2:de-ionized water mixture was used to etch the top InGaAs layer, and a 3:1 H_3PO_4:HCl mixture was used to preferentially etch the (100) InP surface, thereby producing ridges with vertical side-walls. Waveguide widths ranged from 1.5 μm to 4 μm. The substrates were lapped and polished to a thickness of $\approx$ 150 μm to facilitate cleaving the waveguides into 1000 μm lengths. The lengths of individual devices were precisely measured using an optical microscope. SEM samples were prepared to examine the quality of the ridge side-walls and ridge dimensions. In all cases the side-walls exhibited a reasonable smoothness and a slight undercutting, as shown in Fig. 6.1. A further discussion

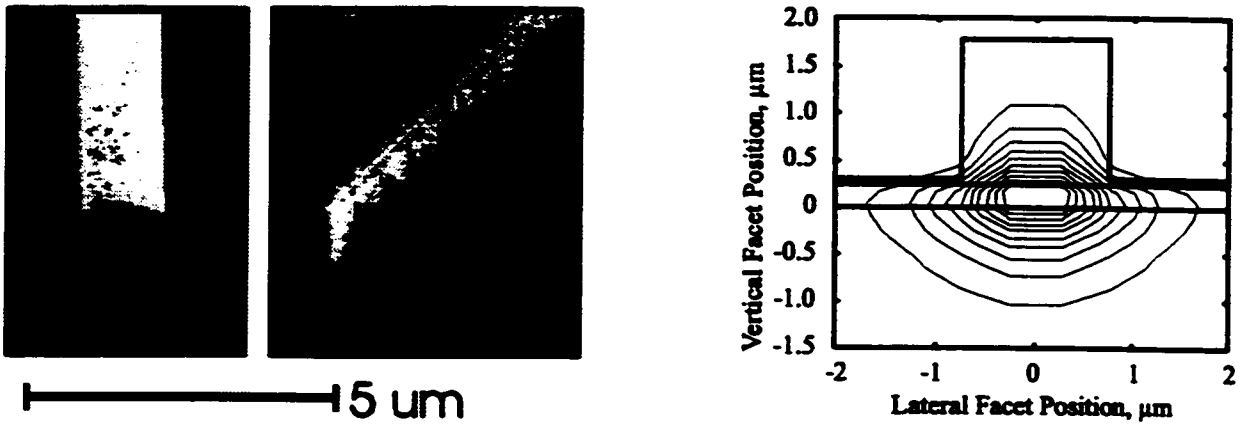

Figure 6.1: (a–b) Two SEM images of ridge waveguides processed from a sample annealed at 800 °C for 30 s. The 1.5 μm ridge waveguide on the left exhibits slight undercutting; the 4 μm guide on the right illustrates the observed side-wall roughness. (c) Accompanying is a contour plot (10 % intervals) of the electric field distribution for the fundamental optical mode of a 1.5 μm guide, as determined by BPM. The waveguide was modeled using an average core index and thickness of 3.392 and 0.25 μm. The core region extends from the vertical facet position of 0–0.25 μm. The InP had an index of 3.165, and the ridge "floats" on a layer on InP 0.05 μm thick, above the core.

of wet-chemical etching is found in Sec. 6.2.1.

Single-mode operation of the waveguides was established by examining the light distribution which exits the waveguide as the probe beam is scanned across the input facet. It was found that waveguides of width greater than 1.5 μm were laterally multi-mode and therefore unusable for testing, as discussed on page 36. The 1.5 μm guides did not show perfect single-mode behavior, which may be evidence of either the second order mode which is close to cutoff, or of higher order modes which have not sufficiently attenuated before reaching the exit facet.

The as-grown material had a RTPL peak wavelength of 1567 nm; consequently, measurements were not possible since the waveguide was too lossy over the operating range of the tunable laser. The results from other samples showed that the absorption edge tracked with the RTPL peak, illustrated for three samples in Fig. 6.2. The waveguide attenuation at 1560 nm was plotted as a function of blue-shift in Fig. 6.3, and found to decrease to a residual level of $\approx 14 \pm 3$ dB/cm once the sample was blue-shifted by greater than 70 nm from the starting wavelength. This residual loss is high, and could be caused by a number of things. One possibility is that the band-gap shifting process introduces defects into the

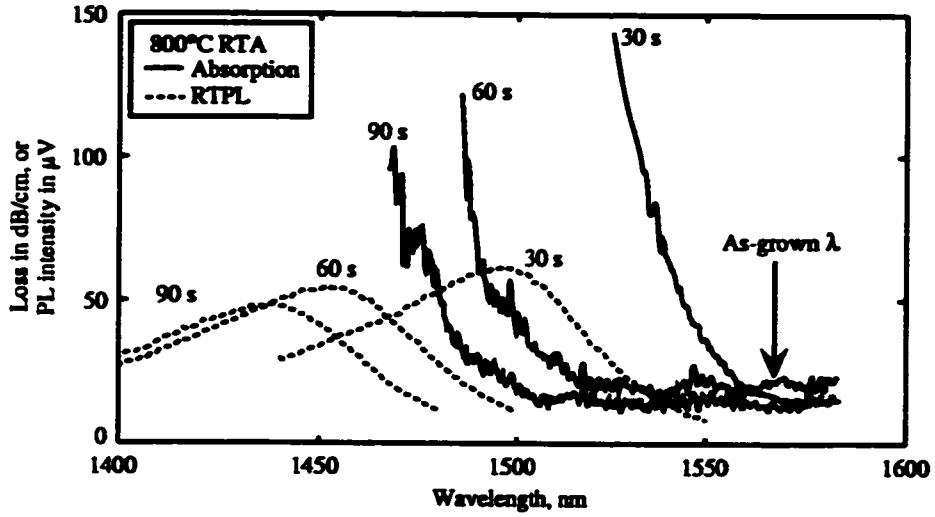

Figure 6.2: Composite figure showing RTPL spectra and corresponding absorption spectra, illustrating that the absorption edge tracks with the PL peak.

structure which act as scattering or absorption centers, thus increasing the waveguide losses. A second possibility is that of inter-valence band absorption (IVBA) in the p-doped waveguide layers. Another possibility is waveguide quality. Beam-propagation-method (BPM) calculations [69] show that the waveguide mode is expected to extend outside of the ridge, Fig. 6.1c. Roughness of the ridge side-walls will cause scattering losses. Additionally, the presence of a second lateral mode will causing beating and obscure the visibility of the Fabry-Perot fringes. Since the residual loss decreases as the amount of blue-shift increases, it seems reasonable that the high losses are a consequence of ridge defects and/or IVBA as opposed to defects introduced by the QWI process. The different film deposition methods do not seem to affect the absorption, except with respect to the magnitude of the band-gap shift. Therefore, to achieve low-loss integrated waveguides the separation between the RTPL peaks of the two sections should be greater than 70 nm.

The group index of the waveguides at 1560 nm was calculated from the Fabry-Perot spectra, and is presented versus the amount of blue-shift in Fig. 6.4. Smaller width ridges have a lower index, Fig. 6.5; although this was used to correct for the individual ridge-widths of the samples in Fig. 6.4, it had little effect. The anomalous points may be related to the insufficient attenuation of higher order lateral modes. It is estimated that the group

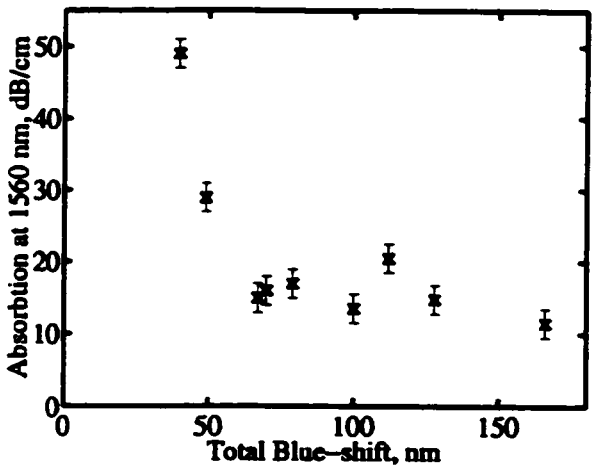

Figure 6.3: Calculated waveguide absorption at 1560 nm as a function of blue-shift.

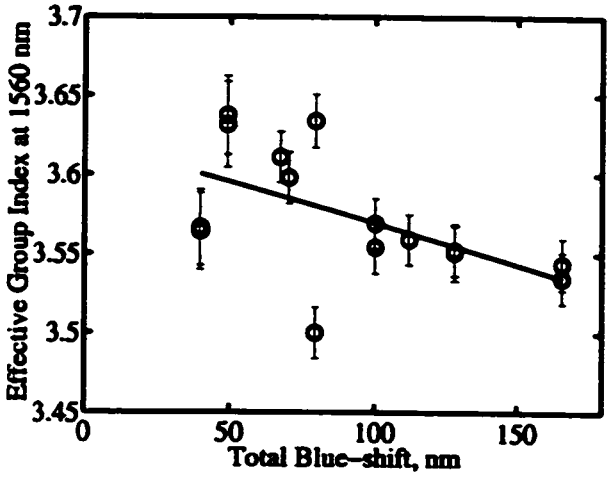

Figure 6.4: Calculated waveguide group index at 1560 nm as a function of blue-shift.

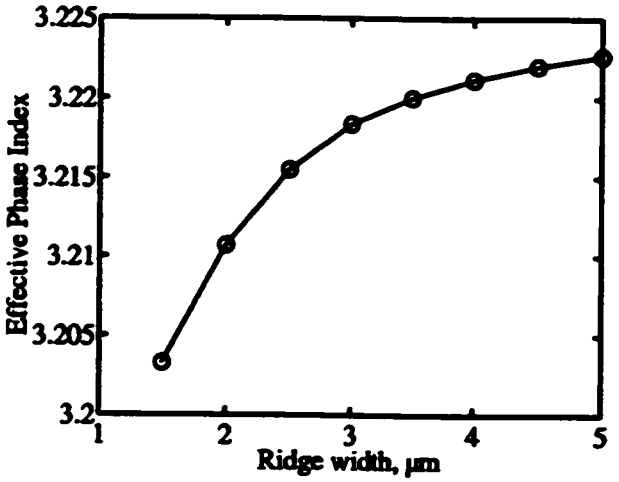

Figure 6.5: Calculated mode phase index as a function of ridge waveguide width for a full laser structure. The waveguide was modeled using BPM, an average core index and thickness of 3.392 and 0.25 μm. The InP had an index of 3.165, and the rib floated 0.05 μm above the core. The electric field distribution for the 1.5 μm ridge is illustrated in Fig. 6.1c.

index changes by $\Delta n = -0.04 \pm 0.01$ in a 70 nm blue-shift. This corresponds to a relative index change of 0.85–1.4 %. The behavior of increasing index with blue-shift has been noted elsewhere in the literature [21], and is due to the shift in band-edge, and not the change in QW composition. This is illustrated in the calculations for an InGaAs well by E. Li [24]. It was calculated that the mode index decreased by $\Delta n = -0.05$ after a blue-shift of 100 nm, at a wavelength 100 nm longer than the band-edge transition. This result is comparable with our measurements.

These results demonstrate that good quality waveguides can be produced, as a loss of 10 dB/cm is considered acceptable [21, 5], although it would certainly be desirable to further reduce this value. The change in mode index is not a significant issue for Fabry-Perot devices; however, this change is a critical factor in determining the spectral characteristics of grating-based waveguide devices such as DFB lasers and distributed Bragg reflectors (DBR). For grating-based devices operating in the 1550 nm regime this corresponds to a wavelength shift of -17 ± 5 nm, which would require consideration during device design.

6.1.2 Area-Selectivity

The technique of scanning photoluminescence (SPL) is essentially the same as described in Sec. 3.1, except that special care is taken to tightly focus the pump beam on the sample, to a spot as small as 1 μm in diameter, using a microscope objective lens. The luminescence is collected by the same lens. This setup allows the examination of an area of the sample localized to a couple microns. By rastering the sample beneath the lens and collecting a PL spectrum at each point, a map of the sample is obtained; the area-selectivity of the intermixing process can be directly observed from this map.

To examine the area-selectivity a full laser structure growth was coated with a PECVD SiO_xN_y film of index n = 1.61, deposited using the low N_2O flow method. Using standard photolithography techniques and BHF as an etchant the SiO_xN_y film was patterned into stripes. To protect the InGaAs surface exposed between the stripes, the entire sample was then coated with SOG and cured. Samples measuring 2.5 × 2.5 mm^2 were cleaved from the patterned region, annealed, and tested.

Figure 6.6 on page 96 shows the results derived from a plan view SPL map of a patterned sample annealed at 780 °C for 60 s. The SPL system with which this measurement was performed had a spatial resolution of roughly 15 μm. Full spectra were taken at each point and analyzed to produce the peak wavelength, peak intensity, and FWHM maps of the sample. The areas where the oxide stripes were present during the anneal are clearly distinguished, and correspond to the second and fourth vertical stripes as counted from the

left. The top-right-corner of the sample was scribed with an "x" for orientation purposes, and is the reason for the missing data. Blank areas in the FWHM map correspond to places where the pump beam straddled both PECVD and SOG-capped regions; the resulting spectra exhibited two peaks. Artifacts from this are also seen as lower peak values in the intensity map. Although this scan does not address the question of how sharp the transition is between the two regions on the sample, it clearly illustrates that edge effects are insignificant and that the intermixing process is uniform over the surface of the sample.

To determine the spatial selectivity the sample was examined *edge-on* instead of in "plan" view. To obtain a clean surface for measurement, a sample was cleaved in two, perpendicular to the SiO_xN_y stripes, after annealing. The measurement apparatus [28] did not acquire a discrete spectrum at each position, but instead employed a wavelength-dependent beam-splitter cube to estimate the mean wavelength of the collected luminescence. A scan was performed over the cleaved sample face, straddling an interface between SiO_xN_y-coated and SOG-coated material. This is shown in Fig. 6.7 on the following page. The area-selectivity is better than 5 μm in this sample, indicating that devices with sharply delineated regions are possible. This is important since it allows composite devices to be created with precision. For example, a short transition region allows the integration of facet windows that do not take up much room on the device, and a short unpumped transition region to a non-absorbing waveguide will not incur significant losses. It also allows the possibility of using the selective intermixing to produce regions of lateral isolation, with precision.

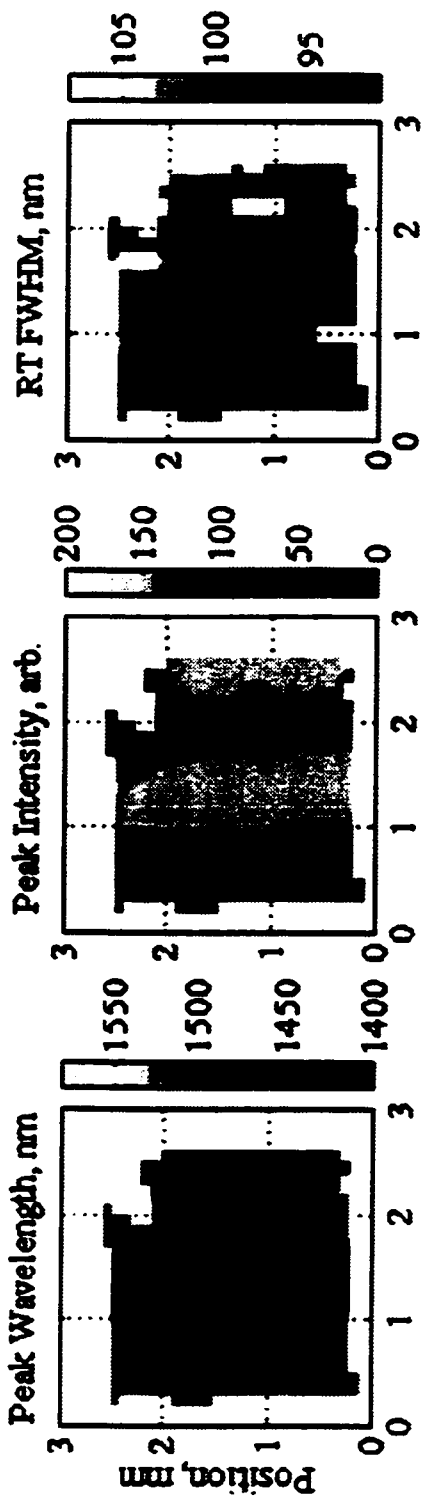

Figure 6.6: Scanning PL measurement of a 2.5 x 2.5 mm sample patterned with a PECVD film, coated with SOG, and then annealed at 780 °C for 60 s. Maps depict the peak wavelength, peak intensity, and the FWHM as determined from RTPL spectra taken at discrete points. Note the lack of edge effects.

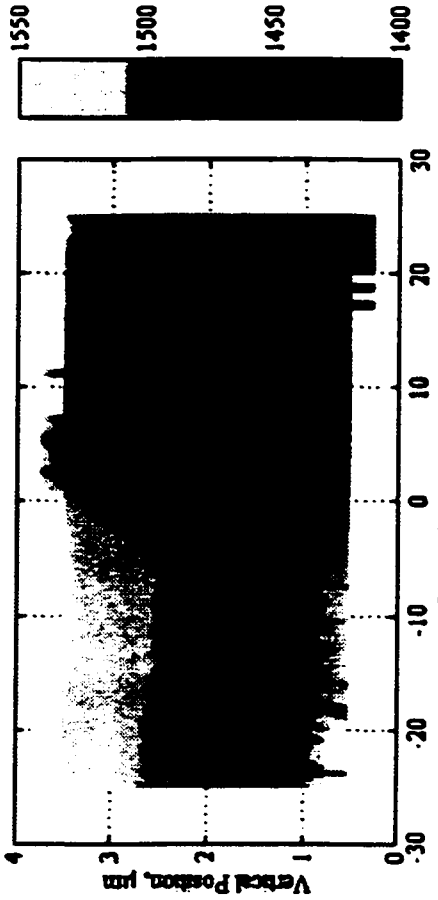

Figure 6.7: Scanning mean-wavelength PL measurement of a sample patterned with a PECVD film and then annealed at 780 °C for 60 s. The image corresponds to a scan in 50 μm long by 5 μm deep; the right side was coated with oxide.

Sample	Concentration ($/cm^3$)	Mobility (cm^2/Vs)	Confidence Factor
As-grown	8.8×10^{14}	4770	0.9995
As-grown	8.7×10^{14}	4770	0.9995
Bare RTA	9.1×10^{14}	4040	0.8062
Oxide RTA	8.5×10^{14}	3980	0.9937
Oxide RTA	8.3×10^{14}	3990	0.9937

Table 6.2: Hall effect results.

6.1.3 Hall Effect Measurements

It is important to have material that remains resistive after annealing [21], such that individual sections of the device remain electrically isolated from each other. Thus, to determine if the intermixing process injects electrically-active defects, Hall effect measurements were performed. Samples consisted of a 3 μm layer of intrinsic InP, grown on a semi-insulating InP substrate. Samples were cleaved into $4 \times 4\,mm^2$ square pieces. Samples with and without a SiO_2-cap were annealed at 800 °C for 60 s. The surface of the uncoated sample exhibited damage in the form of rectangular pits after annealing. The Hall effect measurement results are summarized in Table 6.2. The concentration and mobility values take into account surface depletion effects to arrive at a self-consistent solution. The uncoated annealed sample exhibited a low confidence factor, likely owing to the surface damage. It can be seen that the electrical properties of the SiO_2-capped sample were not affected significantly, just a small reduction in mobility that may be due to surface roughening, possibly like that shown in the AFM image of Fig. 5.14c. It therefore seems reasonable to conclude that the defects introduced into the material are either insufficient or unable to modify the electrical properties of the material, assuming they are electrically active. This is consistent with results from SIMS measurements in the literature [59, 30] which confirm that Si (an n-type dopant in InP) does not migrate into InP-based samples.

One issue that this experiment does not address is that of dopant redistribution in a laser structure during the annealing process. We do not believe that this is an issue for our samples doped with Si and Be. SIMS studies have shown [33] that the Si doping profile remains abrupt. Device processing using He^+-InP-assisted QWI with anneal treatments of

800 °C for 30 s have been successful [22]. Other groups have fabricated integrated devices in the InP/InGaAs system using anneal treatments at 800 °C for times ranging from 30 to 240 s [5], and at 850 °C for 7 s with no degradation in device electrical characteristics [6].

6.2 Processing of Devices From Intermixed Material

As discussed on page 19 of Sec. 2.1.2, there are two potential routes for fabricating devices while incorporating the area-selective QWI process. The options are to either perform the intermixing on completed laser structures where further epitaxial growth is not needed, or to perform the intermixing on a partial structure and subsequently grow additional epitaxial layers to complete the laser structure. Both of these approaches are discussed in the following sections along with their respective merits and shortcomings.

6.2.1 Application of QWI to Completed Structures

By "completed", we mean laser structures that do not require further epitaxial growth. This includes full laser structures grown in one step intended for Fabry-Perot devices, and grating-based devices which require multiple epitaxial growths and a grating patterning step. Regardless, the structures are terminated by a thick cladding of InP ($\approx 1.5\,\mu$m), and a top p-InGaAs contact layer.

The processing begins by depositing the PECVD dielectric film that will be used for the QWI step. This dielectric layer is used both as a mask to produce alignment marks; and as the QWI mask. The devices which are ultimately fabricated will require alignment to the areas of the sample which have been preferentially intermixed. Hence, the first mask step corresponds to etching alignment marks into the InGaAs layer to which both the QWI mask and subsequent mask steps are aligned. Next, the dielectric is patterned to form the QWI mask. For example, the patterning required for an integrated laser-waveguide could be 1000 μm-wide stripes of oxide separated by 1000 μm, which run perpendicular to the direction that the ridge waveguides will run. This geometry would allow either of the sections to be cleaved to a length of up to 1000 μm. This type of QWI stripe mask was used to prepare

the sample seen in Fig. 6.6. At this point the entire surface should be protected by applying a SOG film. After annealing the dielectric material is stripped from the sample with a BHF etch. The alignment marks, where the 2000 Å thick layer of InGaAs was etched away, will be clearly visible. At this point the sample is ready for ridge waveguide patterning. Typically a second PECVD film is deposited and used as the ridge-waveguide etch mask. A 1:8:80 H_2SO_4:H_2O_2:de-ionized water mixture is used to etch the top InGaAs contact layer, and a 3:1 H_3PO_4:HCl mixture is used to etch the InP layer waveguide layer.

We have noted two difficulties with this processing sequence. The first difficulty stems from applying the QWI process to samples which contain gratings and re-growth interfaces [70]. We have noted that the behavior of the intermixing process is not reliable when regrowth interfaces are present. In some samples the blue-shifting effect is suppressed suggesting that the regrowth interface is gettering the defects required for the intermixing. In other cases we have seen the samples exhibit abnormally large amounts of thermal blue-shift, suggesting that the interface is acting as a source of intermixing-enhancing defects.

The second difficulty with this process sequence is that the wet chemical etching behavior of the InGaAs and InP material is modified by the heat treatment process. In general, the etch rate of both InP and InGaAs decreases after heat treatment, for both SiO_xN_y-coated and uncoated samples. After anneal treatments in excess of $\approx 800\,^{\circ}C$, uncoated samples exhibit lower etch rates than PECVD-coated samples. This makes sample processing awkward, since the etch times vary with heat treatment, and in the worst case, some areas of the sample will finish etching significantly in advance of other areas. This is of particular concern when etching the thick 1.5 μm InP ridge-waveguide layer. The 3:1 H_3PO_4:HCl etchant is anisotropic (ridges with vertical side-walls are produced since the etch rate in the lateral direction is much slower than into the depth of the material). The etch rate of InP in this mixture is nominally 6500 ± 500 Å/minute which may be reduced by over a factor of 2 after annealing. Figure 6.8 shows an example of what happens to a sample when the etch rate of the two areas differs significantly. The SiO_2-capped areas etch faster and are therefore completed first. However, while etching in the other areas continues to proceed, the completed

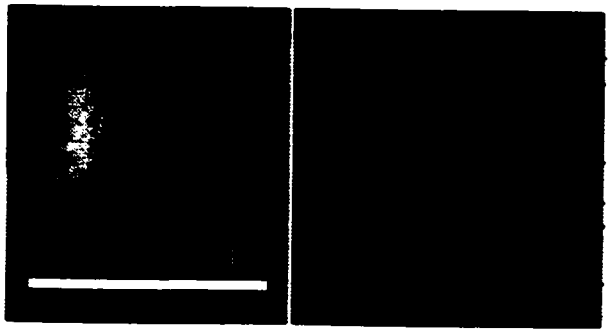

Figure 6.8: Composite SEM image showing a ridge waveguide end on, to illustrate wet chemical etching difficulties. The left side of the image was taken from an area of the sample that was coated with SOG during the 830 °C 30 s anneal, while the right side was capped with a PECVD SiO_2 film.

areas begin to show signs of undercutting. Had this particular sample been etched long enough for the uncoated areas to reach completion, the ridge waveguide in the other section would have become severely undercut. We do not understand the reason for this etching behavior. Since there were multiple difficulties associated with the QWI of completed laser growths, we pursued the alternative method outlined in the following section.

6.2.2 Application of QWI to Incomplete Structures

As discussed in the previous section, there are two reasons to consider the application of the QWI process before the MBE growth of the structures is complete. The final epitaxial growth essentially consists of the top layers of InP and InGaAs from which the ridge waveguide and contacts are produced. Intermixing the structure before these layers are grown is intended to circumvent the difficulties associated with the presence of regrowth interfaces and wet chemical etching. Therefore, ideally, the QWI process is carried out after the epitaxial growth of the active region and before any subsequent processing.

The processing sequence begins with a partial laser structure, terminated with a layer of InGaAs. A PECVD film is applied and patterned in the same way discussed for the completed laser structure on page 98. Once the dielectric QWI mask has been removed using BHF the sample is ready for either grating patterning or regrowth, depending on the desired end device. Since the growth corresponds to a partial laser structure it is easy to test the sample and determine the amount of blue-shift. This is advantageous since early

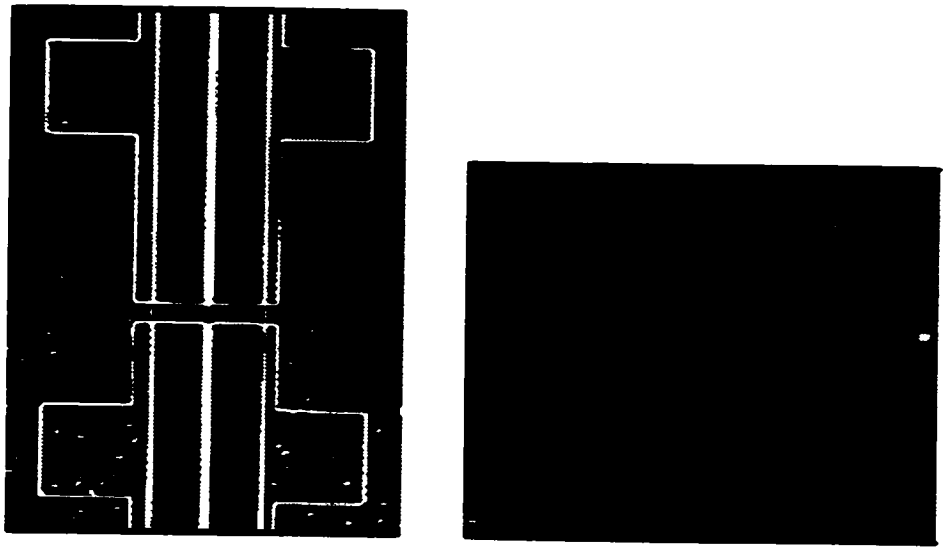

Figure 6.9: Optical microscope Nomarski images of a sample exhibiting oval defects after regrowth. (a) This 370 × 500 μm image shows a split-ridge waveguide running from top to bottom, inside a 100 μm trench; contact pads protrude to the sides. The bottom section was SiO_2-capped during the anneal treatment and exhibits oval defects, which appear as white dots in the image. (b) The image on the right, 35 × 27 μm, is a closeup of the oval defects.

evaluation of the sample allows the subsequent processing to be tailored to an exact amount of obtained blue-shift.

To prepare the sample for regrowth, the top layers are wet chemical etched to expose the 1.15 Q top waveguide layer. The sample is then cleaned with repetitive UV ozone treatments, each followed by a BHF etch and DI water rinse. The re-growth begins by heating the sample to 470 °C in the MBE system under a Group V over-pressure. The epitaxial growth, layers C–C' in Fig. 2.1, starts with a layer of InP. Areas of the sample that were coated with SiO_2 during the anneal exhibited a high density of oval defects in the re-growth. Figure 6.9 shows the resulting surface morphology in plan view for a processed device and a close up of the oval defects. The defects are also present in areas adjacent to the boundary which were not SiO_2-capped during the anneal. Ridge waveguide devices tested from this regrowth did not lase, which is attributed to the oval defects. Cross-sectional TEM samples were prepared from samples, both with and without SiO_2 caps, annealed at 800 °C for 60 s. Figure 6.10 is a bright field image showing the small high-contrast features present at the InP re-growth interface, only in the sample annealed with an SiO_2 cap. High-resolution energy-dispersive

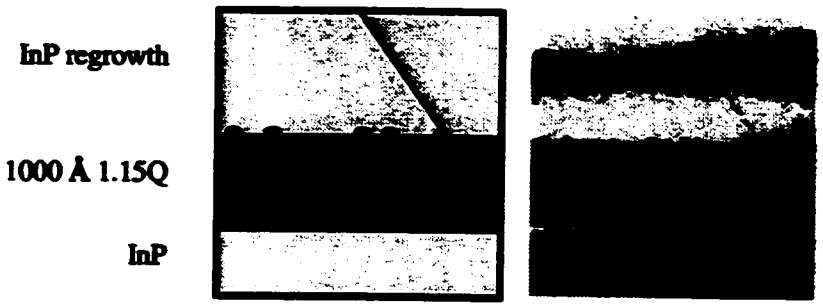

Figure 6.10: Cross-sectional TEM image of InP regrowth.

X-ray measurements indicate that the features are Ga rich. A line defect is also apparent in the figure which appears to originate from one of the interfacial features. These interfacial features are believed to be potential nucleation sites for the oval defects.

A second re-growth study consisted of a terraced sample with thicknesses of semiconductor material (InGaAs and InP) between the SiO_2 and 1.15 Q layer ranging from 0–7250 Å. The SiO_2 film was patterned into stripes perpendicular to the terrace steps. The sample was annealed at 800 °C for 60 s, followed by the removal of the SiO_2 film and terrace layers. The regrowth consisted of $\approx 0.75\,\mu$m InP. The regrowth on areas where the SiO_2 was removed before annealing was acceptable. Areas where the SiO_2 was in direct contact with the subsequent re-growth surface exhibited amorphous InP. All other areas showed poor re-growth, with no significant improvement in the areas where 7250 Å of material separated the dielectric from the regrowth interface. Therefore, simply adding sacrificial material to the structure does not solve the regrowth difficulties.

The cause of the regrowth defects has not yet been determined. We do not yet know if the interfacial defects are formed during the growth of the InP layer, or if they self-organize on the surface during the initial sample heat-up under Group V over-pressure. Since there are reports in the literature of successful regrowth performed on cap annealed samples at 850 °C for 7–9 s [6, 30] we are optimistic in finding a solution.

6.3 Summary of Device Issues

Measurements made on waveguides fabricated from intermixed material indicate that to achieve low-loss integrated waveguides the separation between the RTPL peaks of the two sections must be greater than 70 nm. It is estimated that the mode index increases by between $\Delta n = -0.04 \pm 0.01$ for a blue-shift of this magnitude in this structure. This behavior of increasing index with anneal is due to the shift in band-edge. The change in mode index will strongly affect the spectral characteristics of grating-based waveguide devices corresponding to a wavelength shift of 17 ± 5 nm which would necessitate consideration during device design. Scanning PL measurements indicate that edge effects can be neglected and that the intermixing process is uniform over the surface of the sample. The area selectivity that can be achieved from a sample patterned with a PECVD film and coated with SOG is better than $5\,\mu$m, indicating that devices with sharply delineated regions are possible. Hall effect measurements indicate that the defects introduced via the dielectric film into the material are either insufficient or unable to modify the electrical properties of the material.

There are several associated issues which impede the fabrication of integrated devices using dielectric-enhanced QWI. The intermixing of samples which contain regrowth interfaces (such as in a DFB laser) has proven unreliable, which is believed to be related to the regrowth interface acting as either a source or sink of defects. The patterning of devices via wet chemical etching from QWI material has proven difficult, due to problems with differential etching. In order to circumvent these issues, attempts have been made to produce devices from samples which have been selectively intermixed and then epitaxially regrown. Oval defects, present only in areas that have been annealed with SiO_2 caps, have been linked to the presence of Ga-rich features present at the regrowth interface.

Chapter 7

Conclusions

7.1 Summary of Work

The band-gap shifting behavior of all-quaternary active regions has been described in detail with regards to both device structure and dielectric capping layer. Experiments have been performed to elucidate the mechanism responsible for the dielectric-enhanced QWI effect, and to characterize the results for subsequent device design and processing.

Multiple mechanisms appear to be responsible for the thermal QWI process. There appears to be a fast transient process that causes an 27 ± 2 nm shift within seconds of heat treatment above 600 °C. This is postulated to be associated with grown-in defects, and the activation temperature of this effect depends strongly on sample geometry. The second process, related to the thermal stability of the InGaAsP material, causes the structure to intermix on a longer time scale, and produces large shifts once the anneal temperature exceeds 750 °C. In general the heat treatment process improves the luminescence efficiency of the material.

Laser structures grown on Zn-doped p-substrates are not suitable for optical integration due to the lack of a dielectric-enhanced-shift and a degraded material quality after heat treatment. Partial structures exhibit a lower thermal shift and larger SiO_2-capped shifts than full laser structures, but either type of structure is appropriate. Ternary as opposed to quaternary QWs exhibit a lower thermal shift and yet a larger dielectric-enhanced shift. The different behavior of nominally identical structures suggests that the substrate or growth

conditions affect the QWI results and, therefore, the QWI behavior of every growth should be individually characterized.

SOG films do not enhance the QWI process, and are therefore useful as a protective encapsulating layers. Dielectric caps deposited by PECVD enhance the QWI at temperatures in excess of 720 °C. PECVD SiO_xN_y films provide an enhanced blue-shift that varies with film composition. Film thickness only weakly affects the QWI process in SiO_2 films. SiO_xN_y-coated samples maintain a sharper LTPL FWHM than the bare or SOG-coated samples, suggesting that a higher material quality is maintained despite heavy intermixing.

We believe that the dielectric-enhanced QWI in our InGaAsP/InP samples is through the injection of Group V interstitials which encourage the intermixing process. The migration of Ga and In into the dielectric film, as measured by SIMS, leaves the surface As-rich. We postulate that As is injected into the structure as an interstitial, and is the defect responsible for the enhanced QWI effect. The formation or injection of these interstitials may be mediated by the interfacial stress at the dielectric-semiconductor interface. Stress effects seem likely due to the changes in film properties as measured by FTIR, and the room temperature film stress measurements. During heat treatment the surface of the crystal is expected to be under compressive stress which would retard interstitials from forming and/or entering the crystal, although the resulting strain gradient within the crystal would encourage the interstitials to diffuse through (rather than accumulate within) the active region. If different dielectric films produce significantly different stresses at the film-semiconductor interface then this could explain how the blue-shift varies with PECVD SiO_xN_y composition, and why SOG fails to enhance the blue-shift even when it accepts significant amounts of Ga and In from the sample during anneal. We believe that the Group V interstitials promote disordering through the "Kick-out" mechanism. Arsenic interstitials injected at the surface will create a population of both As and P interstitials as the defects diffuse through the laser structure. The random replacement of both As and P on the Group V sub-lattice in the vicinity of the QW will cause the enhanced intermixing effect.

Fabry-Perot waveguide characterization indicates that to achieve low-loss integrated

waveguides the separation between the RTPL peaks of the two sections must be greater than 70 nm. It is estimated that the mode group index decreases by $\Delta n = -0.04 \pm 0.01$ for a blue-shift of this magnitude in this structure. The change in mode index will strongly affect the spectral characteristics of grating-based waveguide devices, thereby requiring consideration during device design. Scanning PL measurements indicate the intermixing process exhibits a lateral selectivity better than 5 μm, indicating that devices with sharply delineated regions are possible. Hall effect measurements indicate that the introduced defects do not significantly modify the electrical properties of the material.

There are several issues which impede the fabrication of integrated devices using dielectric-enhanced QWI. The intermixing of samples which contain regrowth interfaces has proven unreliable, which is believed to be related to the regrowth interface acting as either a source or sink of defects. The patterning of devices via wet chemical etching from QWI material has proven difficult, due to problems with differential etching. It may be possible to solve this issue by using plasma etching techniques. Epitaxial regrowth over areas preferentially intermixed with SiO_2 films exhibits oval defects linked to the presence of Ga-rich features present on the regrowth interface.

The thermal anneals at 750 °C have the advantage that for a given net dielectric blue-shift the resulting thermal shift is lower, the longer anneal time is easier to control, and the material surface will decompose less. Etching behaviors are more reliable at lower temperature anneals; regrowth studies have not been performed as a function of anneal treatment. Therefore, the most sensible way to proceed for device processing, based on the results presented, is to use lower temperature anneals ($\approx$ 750 °C) of longer duration on full laser structures. Regrowth issues need further study before grating-based intermixed devices can be produced using this method.

7.2 Summary of Original Contributions

Although studies of all-quaternary active regions have been presented in the literature before, there has been no systematic study of a range of structures practical for the fabrication

of optical devices such as lasers with all-quaternary active regions. This study has presented detailed results for four different structures, applicable to practical devices due to the layer structure and doping profiles. The QWI behavior of these structures has been compared and contrasted, both with and without SiO_2 dielectric caps.

The dielectric-enhanced QWI of a partial laser structure was studied in detail using native oxide, SOG, and PECVD SiO_xN_y caps of differing composition. To our knowledge, this is the first time that such a broad study of dielectric films for QWI in the InP materials system has been presented.

The migration of Ga and In into dielectric caps by SIMS has been studied versus anneal time, temperature, and SiO_xN_y composition – a broader study than presented before in the literature. The analysis of this SIMS data by referencing the traces to the Si yield is also a novel technique. FTIR measurements have been presented for dielectric layers used for QWI purposes, but this is the first published study of dielectric films before and after annealing as a function of anneal temperature and SiO_xN_y composition, to our knowledge. We have correlated the loss of H from the SiO_xN_y films with the amount of enhanced QWI, as a function of PECVD SiO_xN_y composition. The change in surface morphology with QWI as observed by AFM is novel.

Our studies have clarified the nature of the "thermal" intermixing effect. Grown-in defects have been postulated to create a fixed amount of intermixing with a low temperature sensitivity on a short time scale; these defects are present both in the active region and in the layers grown above. A second mechanism is responsible for intermixing that is more temperature sensitive and occurs on the order of minutes. We have postulated a new mechanism for the dielectric-enhanced QWI in the InGaAsP/InP materials system, based on Group V interstitials, as opposed to Group III vacancies. The formation and/or injection of these interstitials is believed to be due to the dissolution of Group III atoms (Ga, In) into the dielectric cap, and mediated by the near-surface stress that the dielectric cap imposes on the semiconductor material.

We have reported the Fabry-Perot waveguide characterization of intermixed all-

quaternary active region ridge waveguides as a function of intermixing. We have reported the novel observation of GSMBE regrowth sensitivity to dielectric-capped annealed surfaces, and identified that the defects are related to Ga-rich clusters on the regrowth surface. We have also reported the sensitivity of certain wet chemical etchants to the anneal treatment that the sample undergoes. These issues are important in the fabrication of useful devices.

7.3 Suggested Future Work

In some respects this thesis asks more new questions than it answers. There are a number of extensions that may be added to this body of research, both in terms of solving the technological issues that prevent high-quality devices from being fabricated and in terms of understanding the QWI process further.

The achievement of defect-free regrowth is critical for the production of grating-based intermixed devices. Further study of the defects present at the regrowth interface may identify the nature of the problem and suggest a technique to circumvent it. Ways to potentially control these defects include investigating the composition of the surface to be regrown upon, the cleaning method of the surface (both after anneal and in the MBE), and the specific anneal treatment.

Further investigation of the etching characteristics of intermixed material is important for the production of devices. The wet chemical etch rate issues may be linked to the regrowth defects. Reactive ion etching is expected to be especially useful in obtaining even and consistent etch rates since there is considerable flexibility to develop an etching environment which is both anisotropic and insensitive to material differences.

Since grown-in defects play a significant role in the thermal QWI behavior of all-quaternary active regions this should be studied in greater detail. An examination of different InGaAs cap layer thicknesses could be undertaken to determine how the presence of this layer affects the thermal shift. A larger study of partially etched structures (with different doping, layer compositions and thicknesses) will clarify the nature of the thermal shift. TEM and temperature dependent PL can be used to directly observe how LCM varies with structure

growth conditions and annealing treatment.

Another issue useful for device production would be the study of the QWI behavior of dielectric films patterned at different fine pitches (1–5 μm, for example) to induce different relative amounts of band-gap shift without resorting to the use of different composition dielectric films by multiple depositions.

Film stress should be examined with respect to film composition on InP substrates, over a range of temperatures in order to estimate the film stress at the annealing temperature. This may identify why the SIMS migration measurements versus dielectric composition do not correlate with the intermixing results.

References

[1] "The New Encyclopædia Britannica, 15th ed." 1998, Or see for example http://www.britannica.com.

[2] R. W. Clark, *The Scientific Breakthrough: The impact of modern invention.* G. P. Putnam's Sons, 1974.

[3] Intel Corp., "25th Anniversary Hall of Fame." http://www.intel.com/intel/museum, [May 29th, 2000].

[4] B. Streetman, *Solid State Electronic Devices.* Prentice Hall, 4th ed., 1995.

[5] T. Miyazawa, H. Iwamura, and M. Naganuma, "Integrated external-cavity InGaAs/InP lasers using cap-annealing disordering," *IEEE Photon. Technol. Lett.*, vol. 3, pp. 421–423, May 1991.

[6] A. Ramdane, P. Krauz, E. V. K. Rao, A. Hamoudi, A. Ougazzaden, D. Robein, A. Gloukhian, and M. Carré, "Monolithic integration of InGaAsP-InP strained-layer distributed feedback laser and external modulator by selective quantum-well interdiffusion," *IEEE Photon. Technol. Lett.*, vol. 7, pp. 1016–1018, Sept. 1995.

[7] P. Ojala, C. Pettersson, B. Stoltz, A. C. Mörner, M. Janson, and O. Sahlén, "DFB laser monolithically integrated with an absorption modulator with low residual reflectance and small chirp," *Electron. Lett.*, vol. 29, pp. 859–860, May 1993.

[8] C. H. Joyner, S. Chandrasekhar, J. W. Sulhoff, and A. G. Dentai, "Extremely large band gap shifts for MQW structures by selective epitaxy on SiO_2 masked substrates," *IEEE Photon. Technol. Lett.*, vol. 4, pp. 1006–1009, Sept. 1992.

[9] D. Hofstetter, H. P. Zappe, J. E. Epler, and P. Riel, "Monolithically integrated DBR laser, detector, and transparent waveguide fabricated in a single growth step," *IEEE Photon. Technol. Lett.*, vol. 7, pp. 1022–1024, Sept. 1995.

[10] P. G. Piva, S. Fafard, M. Dion, M. Buchanan, S. Charbonneau, R. D. Goldberg, and I. V. Mitchell, "Reduction of InGaAs/GaAs laser facet temperatures by band-gap shifted extended cavities," *Appl. Phys. Lett.*, vol. 70, pp. 1662–1664, Mar. 1997.

[11] S. F. Yu and E. H. Li, "Semiconductor lasers using diffused quantum-well structures," *IEEE J. Sel. Topics in Quantum Electron.*, vol. 4, pp. 723–735, Nov. 1998.

[12] A. Q. Jiang, C. Z. Sun, Z. B. Hao, Y. Luo, and J. H. Wang, "Novel laser structures based on MQW interdiffusion using rapid thermal annealing technique," *IEEE J. Sel. Topics in Quantum Electron.*, vol. 4, pp. 736–740, Nov. 1998.

[13] J. Micallef, J. L. Borg, and E. H. Li, "Interdiffused InGaAs/InP quantum wells for polarization-independent electroabsorbtion," *Opt. Quantum Electron.*, vol. 29, pp. 423–428, 1997.

[14] E. H. Li, E. S. Koteles, and J. H. Marsh, "Introduction to the issue on interdiffused quantum-well materials and devices," *IEEE J. Sel. Topics in Quantum Electron.*, vol. 4, pp. 581–582, Nov. 1998.

[15] S. Bürkner, M. Maier, E. C. Larkins, W. Rothemund, E. O'Reilly, and J. D. Ralston, "Process parameter dependence of impurity-free interdiffusion in GaAs/$Al_xGa_{1-x}As$ and $In_yGa_{1-y}As$/GaAs multiple quantum wells," *J. Electron. Mat.*, vol. 24, no. 7, pp. 805–812, 1995.

[16] W. D. Laidig, N. Holonyak Jr., M. D. Camras, K. Hees, J. J. Coleman, P. D. Dapkus, and J. Bardeen, "Disorder of an AlAs-GaAs superlattice by impurity diffusion," *Appl. Phys. Lett.*, vol. 38, pp. 776–778, May 1981.

[17] S. Charbonneau, E. S. Koteles, P. J. Poole, J. J. He, G. C. Aers, J. Haysom, M. Buchanan, Y. Feng, A. Delage, F. Yang, M. Davies, R. D. Goldberg, P. G. Piva, and I. V. Mitchell, "Photonic integrated circuits fabricated using ion implantation," *IEEE J. Sel. Topics in Quantum Electron.*, vol. 4, pp. 772–793, Nov. 1998.

[18] J. H. Marsh, O. P. Kowalski, S. D. McDougall, B. C. Qiu, A. McKee, C. J. Hamilton, R. M. De La Rue, and A. C. Bryce, "Quantum well intermixing in material systems for 1.5 μm," *J. Vac. Sci. Tech. A*, vol. 16, pp. 810–816, Mar. 1998.

[19] M. Kuzuhara, T. Nozaki, and T. Kamejima, "Characterization of Ga out-diffusion from GaAs into SiO_xN_y films during thermal annealing," *J. Appl. Phys.*, vol. 66, pp. 5833–5836, Dec. 1989.

[20] J. Y. Chi, X. Wen, E. S. Koteles, and B. Elman, "Spatially selective modification of GaAs/AlGaAs quantum wells by SiO_2 capping and rapid thermal annealing," *Appl. Phys. Lett.*, vol. 55, pp. 855–857, Aug. 1989.

[21] J. H. Marsh and A. C. Bryce, "Fabrication of photonic integrated circuits using quantum well intermixing," *Mat. Sci. Eng. B*, vol. B28, pp. 272–278, 1994.

[22] G. J. Letal, *Integrated Distributed Feedback Lasers and Electroabsorption Modulators Fabricated Using Helium-Plasma-Assisted InP Defect Induced Quantum Well Intermixing.* PhD thesis, McMaster University, 2000.

[23] D. A. Thomposon, J. F. Hazell, A. S. W. Lee, T. Yin, G. J. Letal, B. J. Robinson, N. Bertsch, and J. G. Simmons, "New methods of defect-enhanced quantum well intermixing and demonstrated integrated distributed feedback laser-modulator," in *Photonics Taiwan*, July 2000.

[24] E. H. Li, "Optical properties of an InGaAs-InP interdiffused quantum well," *IEEE J. Quantum Electron.*, vol. 34, pp. 982–990, June 1998.

[25] C. K. W. Wyllie and D. A. Thomposon, "Compositional intermixing enhancement in InGaAs(P)/InP quantum well heterostructures related to lateral composition modulation," *Semicond. Sci. Technol.*, vol. 13, pp. 750–755, 1998.

[26] L. M. Lam, C. W. Kwong, H. P. Ho, E. Y. B. Pun, K. S. Chan, Z. N. Fan, and P. K. Chu, "Plasma immersion Ar^+ ion implantation induced disorder in strained InGaAsP multiple quantum wells," *Electron. Lett.*, vol. 34, pp. 817–818, Apr. 1998.

[27] J.-P. Noël, D. Melville, T. Jones, F. R. Sheperd, C. J. Miner, N. Puetz, K. Fox, P. J. Poole, E. S. Feng, Y. Koteles, S. Charbonneau, R. D. Goldberg, and I. V. Mitchell, "Interdiffusion of the group III sublattice in In-Ga-As-P/In-Ga-As-P and In-Ga-As/In-Ga-As heterostructures," *Appl. Phys. Lett.*, vol. 69, pp. 3516–3518, Dec. 1996.

[28] J. Yang, B. B. Elenkrig, D. T. Cassidy, D. M. Bruce, and I. M. Templeton, "Application of polarization resolved photoluminescence to the study of quantum well intermixing in InGaAsP systems," *Semicond. Sci. Technol.*, vol. 10, pp. 483–488, 1995.

[29] B. B. Elenkrig, D. A. Thompson, J. G. Simmons, D. M. Bruce, Y. Si, J. Zhao, J. D. Evans, and I. M. Templeton, "Experimental study of implantation-induced disordering in InGaAsP strained multiple-quantum-well heterostructures," *Appl. Phys. Lett.*, vol. 65, pp. 1239–1241, Sept. 1994.

[30] A. Hamoudi, E. V. K. Rao, P. Krauz, A. Ramdane, A. Ougazzaden, D. Robein, and H. Thibierge, "Controlled disordering of compressively strained InGaAsP multiple quantum wells under SiO:P encapsulant and application to laser-modulator integration," *J. Appl. Phys.*, vol. 78, pp. 5638–5641, Nov. 1995.

[31] A. Hamoudi, A. Ougazzaden, P. Krauz, E. V. K. Rao, M. Juhel, and H. Thibierge, "Cation interdiffusion in InGaAsP/InGaAsP multiple quantum wells with constant P/As ratio," *Appl. Phys. Lett.*, vol. 66, pp. 718–720, Feb. 1995.

[32] S. S. Rao, W. P. Gillin, and K. P. Homewood, "Interdiffusion of the group-III sublattice in In-Ga-As-P/In-Ga-As-P and In-Ga-As/In-Ga-As heterostructures," *Phys. Rev. B*, vol. 50, pp. 8071–8073, Sept. 1994.

[33] A. Hamoudi, A. Ougazzaden, P. Krauz, K. Rao, M. Juhel, and H. Thibierge, "An optical study of interdiffusion in strained InP-based heterostructures," *Jpn. J. Appl. Phys. Pt. 1*, vol. 34, pp. 36–41, Jan. 1995.

[34] C. Francis, F. H. Julien, J.-Y. Emery, R. Simes, and L. Goldstein, "Selective band-gap blueshifting of InGaAsP/InGaAs(p) quantum wells by thermal intermixing with phosphorus pressure and dielectric capping," *J. Appl. Phys.*, vol. 75, pp. 3607–3610, Apr. 1994.

[35] J. W. Park, H. S. Kim, J. S. Kim, D. K. Oh, K. R. Oh, D. H. Yeo, and S. J. Kim, "Intermixing characteristics of strained-InGaAs/InGaAsP multiple quantum well structure using impurity-free vacancy diffusion," *Jpn. J. Appl. Phys. Pt. 2*, vol. 38, pp. L1303–L1305, Nov. 1999.

[36] J. F. Hazell, "The effect of varying barrier layer composition on the output characteristics of 1.3 μm InGaAsP MQW lasers," Master's thesis, McMaster University, 1995.

[37] R. R. LaPierre, "Spinodal decomposition of InGaAsP on (100) and non-(100) InP substrates," Master's thesis, McMaster University, 1994.

[38] R. R. LaPierre, T. Okada, B. J. Robinson, D. A. Thompson, and G. C. Weatherly, "Spinodal-like decomposition of InGaAsP/(100)InP grown by gas source molecular beam epitaxy," *J. Crystal Growth*, vol. 155, p. 1, 1995.

[39] L. A. Coldren and S. W. Corzine, *Diode Lasers and Photonic Integrated Circuits*. Wiley Interscience, 1995.

[40] AlliedSignal Inc., Advanced Microelectronic Materials, "Product Bulletin: Accuglass T-11 Series Spin-On Glass (SOG)," 1992.

[41] R. K. Wild, "Surface analytical techniques," *Adv. Mat. for Optics and Electronics*, vol. 5, pp. 53–70, Dec. 1995.

[42] O. Brox, K. Iltgen, S. Hellweg, and A. Benninghoven, "Determination of silicon oxide layer thickness by time-of-flight secondary ion mass spectrometry," *J. Vac. Sci. Tech. A*, vol. 17, pp. 2191–2192, Sept. 1999.

[43] D. Landheer, S. M. Sayedi, L. M. Landsberger, and M. Kahrizi, "Fourier transform infrared spectroscopy of corona-processed silicon dioxide films," *J. Vac. Sci. Tech. B*, vol. 16, pp. 605–608, Mar. 1998.

[44] L. Fu, P. N. K. Deenapanray, H. H. Tan, C. Jagadish, L. V. Dao, and M. Gal, "Quality of silica capping layer and its influence on quantum-well intermixing," *Appl. Phys. Lett.*, vol. 76, pp. 837–839, Feb. 2000.

[45] B. F. Hanyaloglu and E. S. Aydil, "Low temperature plasma deposition of silicon nitride from silane and nitrogen plasmas," *J. Vac. Sci. Tech. A*, vol. 16, pp. 2794–2803, Sept. 1998.

[46] J. Yeh and S. Lee, "Structural and optical properties of amorphous silicon oxynitride," *J. Appl. Phys.*, vol. 79, pp. 656–663, Jan. 1996.

[47] W. A. Lanford and M. J. Rand, "The hydrogen content of plasma-deposited silicon nitride," *J. Appl. Phys.*, vol. 49, pp. 2473–2477, Apr. 1978.

[48] Y. Cros, N. Jaffrezic-Renault, J. M. Chovelon, and J. J. Fombon, "Study of PECVD silicon oxynitride thin layers as ISFET and sensitive insulator surface for pH detection," *J. Electrochem. Soc.*, vol. 139, pp. 507–511, Feb. 1992.

[49] Tencor Corporation, "Tencor FLX-2900 Manual." #238856 Rev. B 4/93, 1993.

[50] O. Madelung, M. Schulz, and H. Weiss, eds., *Numerical data and functional relationships in science and technology New Series III/22a*. Springer-Verlag, 1982.

[51] J. J. He, E. S. Koteles, M. Davis, P. J. Poole, M. Dion, Y. Feng, S. Charbonneau, P. Piva, M. Buchanan, R. Goldberg, and I. Mitchell, "Transparency of band-gap shifted InGaAsP/InP quantum-well waveguides," *Can. J. Phys. (Suppl.)*, vol. 74, pp. S32–S34, 1996.

[52] O. M. Khreis, K. P. Homewood, and W. P. Gillen, "Interdiffusion in InGaAs/GaAs: The effect of growth conditions," *J. Appl. Phys.*, vol. 84, pp. 232–236, July 1998.

[53] R. W. Glew, A. T. R. Briggs, P. D. Greene, and E. M. Allen, "The influence of the substrate on the thermal stability of InGaAs/InGaAsP quantum wells," in *Fourth International Conference on Indium Phosphide and Related Materials*, pp. 234–237, 1992.

[54] D. H. Yeo, K. H. Yoon, and S. J. Kim, "Characteristics of intermixed InGaAs/InGaAsP multi-quantum-well structure," *Jpn. J. Appl. Phys. Pt. 1*, vol. 39, pp. 1032–1034, Mar. 2000.

[55] I. J. Pape, P. Li Kim Wa, J. P. R. David, P. A. Claxton, P. N. Robson, and D. Sykes, "Diffusion-induced disordering of $Ga_{0.47}In_{0.53}As$/InP multiple quantum wells with zinc," *Electron. Lett.*, vol. 24, pp. 910–911, July 1988.

[56] M. Razeghi, O. Acher, and F. Launay, "Disorder of $In_xGa_{1-x}As_{1-y}P_y$)–InP quantum well by Zn diffusion," *Semicond. Sci. Technol.*, vol. 2, pp. 793–796, 1987.

[57] R. R. Lapierre, T. Okada, B. J. Robinson, D. A. Thompson, and G. C. Weatherly, "Lateral composition modulation in InGaAsP strained layers and quantum wells grown on (100)InP by gas source molecular beam epitaxy," *J. Crystal Growth*, vol. 158, pp. 6–14, 1995.

[58] A. Pépin, C. Vieu, M. Schneider, H. Launois, and Y. Nissim, "Evidence of stress dependence in SiO_2/SiN_x encapsulation-based layer disordering of GaAs/AlGaAs quantum well heterostructures," *J. Vac. Sci. Tech. B*, vol. 15, pp. 142–153, Jan. 1997.

[59] E. K. V. Rao, P. Harmoudi, M. Juhel, and H. Thibierge, "New encapsulant source for III-V quantum well disordering," *Appl. Phys. Lett.*, vol. 66, pp. 472–474, Jan. 1995.

[60] M. Katayama, Y. Tokuda, N. Ando, Y. Inoue, A. Usami, and T. Wada, "X-ray photoelectron spectroscopic study of rapid thermal processing on SiO_2/GaAs," *Appl. Phys. Lett.*, vol. 54, pp. 2559–2561, June 1989.

[61] S. Wallace, "Private Communication: Examination of InGaAsP grown on GaAs by atomic force microscopy," 2000.

[62] *Properties of Si, EMIS Datareviews Series # 4.* INSPEC, 1988.

[63] *Properties of InP, EMIS Datareviews Series # 6.* INSPEC, 1991.

[64] B. L. Olmsted and S. N. Houde-Walter, "Al-Ga interdiffusion through group III-vacancy second nearest-neighbor hopping," *Appl. Phys. Lett.*, vol. 63, pp. 530–532, July 1993.

[65] H. Pinkney, D. A. Thompson, B. Robinson, P. Mascher, P. Simpson, U. Myler, J. Kang, and M. Frankney, "Characterization of annealed high-resistivity InP grown by He-plasma-assisted epitaxy," *J. Vac. Sci. Tech. A*, vol. 16, pp. 772–775, Mar. 1998.

[66] M. Schultz, U. Egger, R. Scholz, O. Breitenstein, and U. Gösele, "Experimental and computer simulation studies of diffusion mechanisms on the arsenic sublattice of gallium arsenide," *J. Appl. Phys.*, vol. 83, pp. 5295–5301, May 1998.

[67] R. F. Scholz and U. Gösele, "Phosphorus and antimony in GaAs as tracers for self-diffusion on the arsenic sublattice," *J. Appl. Phys.*, vol. 87, pp. 704–710, Jan. 2000.

[68] M. G. Boudreau, S. G. Wallace, G. Balcautis, S. Murugkar, H. K. Haugen, and P. Mascher, "Application of in-situ ellipsometry in the fabrication of thin film optical coatings on semiconductors," *Appl. Opt.*, vol. 39, pp. 1053–1058, Feb. 2000.

[69] D. Yevick, "A guide to electric field propagation techniques for guided-wave optics," *Opt. Quantum Electron.*, vol. 26, pp. 5185–5197, 1994.

[70] S. Nagy, G. J. Letal, and J. F. Hazell, "Private Communication: Experiments involving the band-gap shifting of completed DFB laser structures," 1997-1999.